Exploration of manganese doped Prussian Blue in energy storage to design Supercapacitor and in optical sensor to detect Glutathion

A thesis submitted towards partial fulfilment of the requirements for the degree of

Master of Technology in Nano Science and Technology

Submitted by

Srijita Chakraborty

Roll Number: M4NST24010

Registration Number: 151949 of 2019-2020

Under the guidance of

Dr. Chandan Kumar Ghosh

Jadavpur University

SCHOOL OF MATERIALS SCIENCE AND NANOTECHNOLOGY

Jadavpur University

Kolkata-70003

CERTIFICATE OF RECOMMENDATION

This is to certify that the thesis entitled "**Exploration of manganese doped Prussian Blue in energy storage to design Supercapacitor and in optical sensor to detect Glutathion**" is an authentic work carried out by **Srijita Chakraborty** under our supervision and guidance for partial fulfilment of the requirement for Post Graduate Degree of Master of Technology in Nano Science and Technology during the academic session 2022-2024.

THESIS ADVISOR

Dr. Chandan Kumar Ghosh

School of Materials Science and Nanotechnology

Jadavpur University,

Kolkata -700032

DIRECTOR

School of Materials Science and Nanotechnology

Jadavpur University

Kolkata-700032

DEAN

Faculty Council of Interdisciplinary Studies, Law and Management

Jadavpur University, Kolkata -700032

CERTIFICATE OF APPROVAL

I hereby endorse the foregoing thesis as an engineering study, conducted and presented in a manner satisfactory enough to justify its acceptance as an engineering study, in order to obtain the degree for which it has been submitted. This approval does not endorse or approve any statement made, opinion expressed or conclusion drawn therein, but merely approves the thesis for the purpose for which it has been submitted.

Committee of the final examination for evaluation of the Thesis

---

DECLARATION OF ORIGINALITY AND COMPLIANCE OF ACADEMIC ETHICS

I hereby declare that this thesis contains a literature survey and original research work by the undersigned candidate for the Master of Technology (Nano Science and Technology) program during the academic year 2020-2022. The information in this document has been gathered and presented according to academic standards and ethical conduct. I also declare that I have cited and referred to all materials and results that are not original to this work as required by these rules and conduct.

Name: Srijita Chakraborty

Roll Number: M4NST24010

Registration Number:151949 0f 2019-2020

Thesis Title: Exploration of manganese doped Prussian Blue in energy storage to design Supercapacitor and in optical sensor to detect Glutathion

Signature **Date**

Dedicated to my parents

ACKNOWLEDGEMENT

This work described in the thesis titled "***Exploration of manganese doped Prussian Blue in energy storage to design Supercapacitor and in optical sensor to detect Glutathion***" was started in the School of Materials Science & Nanotechnology department laboratory, Jadavpur University in 2024 and would not have been what it is today without the support and advice of others. It was a golden opportunity to work under the guidance of Dr. Chandan Kumar Ghosh, School of Materials Science & Nanotechnology. I sincerely would like to thank him for his support and experienced guidance throughout the project work and for allowing me to utilize the valuable resources and necessary laboratory and library facilities. I accept this opportunity to thank all the members of our department for helping me to carry out some key characterization studies. I am deeply indebted to Roshni Begum,Kabir Khan,Dr.Sudipta Goswami for their invaluable contribution to complete my project work. I take this occasion also to thank all my classmates whose cooperative attitude helped me very much. I would also like to acknowledge the cooperation of all the staff members of department during my project work.

Finally, I pay my indebt acknowledgement to my family for giving me inspiration and supporting me.

ABSTRACT

In the present work, the Prussian blue (PB) and manganese doped Prussian blue (MnPB) materials were synthesized via simple reflux procedure at 60ºC temperature.

The as-synthesized samples were characterized by X-ray diffraction (XRD), Field emission scanning electron microscopy (FESEM), Fourier transform infra-red spectroscopy (FTIR), UV Visible spectroscopy, photoluminescence spectroscopy.

The structural study was conducted for XRD in a 2θ mode from 10º to 80º. The crystal morphologies of the prepared samples were observed using FESEM. The framework crystalline structure constructed with cyanide ligands was verified using FTIR analysis. Ultraviolet−Visible spectral study was recorded to understand the electronic structure and to calculate the optical band gap of the prepared samples.

The electrochemical measurement cyclic voltammetry (CV) of all samples was performed. Mn:PB delivered the highest specific capacitance in aqueous 0.5M Na_2SO_4 electrolyte. The total charge storage included both outer and inner contributions to the specific capacitance. The higher value of inner contribution to the specific capacitance suggested that the redox reaction play a dominating role in storing the charges.

We believe that the observable results show future perspectives to develop superior, cost effective and eco-friendly asymmetric supercapacitor.

Manganese is sensitive to glutathoin which can show a visible difference in photoluminescence spectroscopy and UV Vis spectroscopy.Mn doped prussian blue can be used in glutathoin sensor.

SL no.	CONTENTS :	Page no.
1.	**CHAPTER 1: INTRODUCTION** • Definition of Nano Science & Technology • Structure of PB & PBAs and its Application • Introduction to Supercapacitors • Fundamentals of ES • Types of Supercapacitors and its Charge Storage Mechanism • Choice of Electrode and Electrolyte • . Introduction to Cyclic Voltammetry • Introduction to EIS • REFERENCES	9 10 12 14 27 31 34 37 39
2.	**CHAPTER 2:INSTRUMENTATION** • Scanning Electron Microscope (SEM) • X-Ray Diffraction (XRD) • FTIR (Fourier Transform Infrared Spectroscopy) • UV-Visible Spectroscopy • Photoluminescence Spectroscopy • Cyclic Voltametry • Reference	41 45 46 50 55 60 60
3.	**CHAPTER 3:LITERATURE REVIEW** • Prussian blue and manganese doped Prussian blue as electrode material • Prussian blue and manganese doped Prussian blue in optical sensor	62 65
4.	**CHAPTER 4:SYNTHESIS**	67
5.	**CHAPTER5:RESULt AND DISCUSSION** • XRD Analysis • Williamson-Hall Plot • FEESEM Analysis • FTIR Spectra Analysis • Photoluminescence Spectroscopy • UV- Visible Spectra Analysis • Electrochemical property of Prussian blue and manganese doped prussian blue • Exploration of prussian blue and manganese doped prussian blue in optical sensor to detect glutathoin	68 69 70 71 72 73 75 91

Chapter-1

INTRODUCTION



Definition of Nano Science & Technology

Nanomaterials describe, in principle, chemical substances or materials of which a single unit is sized (in at least one dimension) between 1 and 100 nm (the usual definition of nanomatrials.

Nanomaterials research takes a materials science-based approach to nanotechnology, leveraging advances in materials metrology and synthesis which have been developed in support of microfabrication research. Materials with structure at the nanoscale often have unique optical, electronic, thermo-physical or mechanical properties.In ISO/TS 80004, *nanomaterial* is defined as the "material with any external dimension in the nanoscale or having internal structure or surface structure in the nanoscale", with *nanoscale* defined as the "length range approximately from 1 nm to 100 nm". This includes both *nano-objects*, which are discrete pieces of material, and *nanostructured materials*, which have internal or surface structure on the nanoscale; a nanomaterial may be a member of both these categories.

Feynman hypothesised a process to manipulate individual atoms and molecules, using a set of sophisticated tools to build and operate another relatively smaller set, so on down to the required scale. He also visualized scaling issues would emerge from the changing magnitude of various physical property, like surface tension and Van der Waals attraction would become more significant than gravity. The term nano simply denotes a scale of 10^{-9} m and nanomaterials are those with at least one dimension falling in nanometer scale.

So Nanotechnology is the science and technology of materials in the nanoscale, whose physical, chemical and biological properties distinctively differ from that of their bulk scale.

Bulk matter differs in property from their corresponding nanoparticles. The properties of the material are dependent on the size. As the size of the matter decreases, a significant change in the material property is observed. So, it can be inferred that

- The properties are affected by the large increase in surface to volume ratio and high surface energy.
- Quantum confinement rises from the size reduction of material.

Mainly based on these aspects such as size reduction, phase change, changes in electric or magnetic domains, etc., nanomaterials undergo variations in their melting point, thermal expansion coefficient, hardness, diffusivity, optical absorption, dielectric properties and magnetic properties and so on.

Commonly nanomaterials are classified based on the number of dimensions (<100 nm) :(a)zero-dimensional (0-D), b)one-dimensional (1-D), c) two-dimensional (2-D) and d) threedimensional (3-D)

have shown in Fig. 1.1.

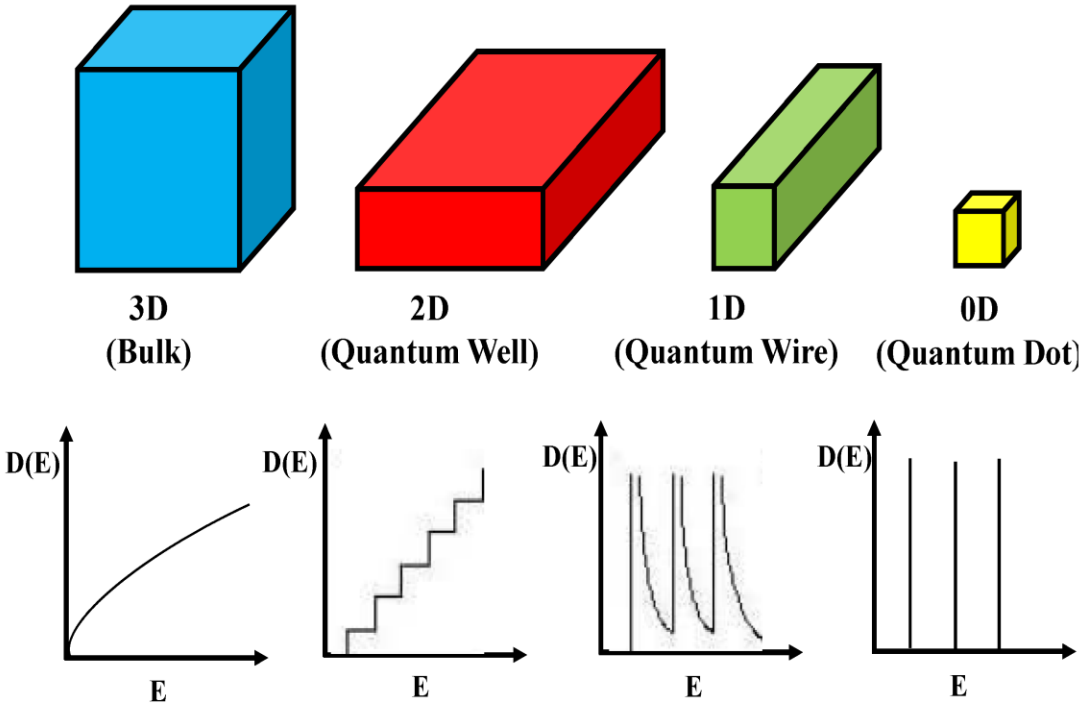


Fig. 1.1 - Density of states of 3-D, 2-D, 1-D and 0-D nanomaterial

Quantum dots, nanorods, nanowires, thin film and nanostructured bulk materials are the typical example of nanomaterials. So to understand the electronic structure and associated properties of different structures, primarily it is mandatory to understand their density of 2 states (DOS) i.e. number of electron energy states per unit volume over the energy interval E to E+ dE.

There are many potential applications of nanotechnology, including

- **Nanomaterials** : Nanoscopic particles for coatings, lubricants, as catalyst in chemical processing, in organ specific drug delivery etc. Nanocomposite materials with improved properties can be used for the construction of aircraft, sports cars, bikes, the development of energy storage devices like supercapacitors, rechargeable batteries, fuel cells and also to design bulletproofing helmet and SMART uniform etc.
- **Nanoelectronics** : It is promoting the attainment of super miniaturization and high packing density, extremely small, fast and low power electronic devices, such as transistor, MOSFETs, CNT FETs, computing and memory devices.
- **Nano-optics & Nanomagnetics** : These includes the development of nanoscale optical circuits, storage technologies and logic devices.
- **Nanofluidics** : This type of devices leading to the “lab on a chip” system for analytical, bioanalytical and drug delivery applications.

Structure of Prussian Blue :

Porous crystalline coordination polymers like Prussian blue (PB) and Prussian blue analogues (PBAs) are formed by linking of inorganic metal ions and electron donating organic ligands, have become a rapidly developing research area owing to their high specific surface area, controllable structures, high porosity, low framework density and high thermal stability. Due to the considerable features of PB and PBAs act as outstanding candidates for potential uses in many fields especially in the field of energy storage devices like fuel cells, alkali ion rechargeable batteries, supercapacitors, solar cells etc.

Fig. 1.2 depicts two different structural variations of Prussian blue, i.e. the soluble Prussian blue (SPB), KFe(III)[Fe(II)$(CN)_6$] and insoluble Prussian blue (IPB), Fe(III)$_4$[FeII$(CN)_6]_3$, nH_2O. The crystal lattice of the insoluble PB displays a face centered cubic (fcc) crystal containing different oxidation states of iron atoms (2+ and 3+) which are settled in the crystal sites and linked by pairs of cyano group. Fe^{3+} is interconnected with the octahedral nitrogen but carbon atoms are surrounding Fe^{2+} ions. The crystal lattice has 25% voids of $[Fe^{2+}(CN)_6]^{4-}$ clusters that are coming from the charge neutrality because of the particular ratio between Fe^{2+} and Fe^{3+} (3:4). As a result, these octahedral vacancies in the crystal lattice are occupied by water molecules. The water molecules are found to be positioned in two different places from the lattice; the corner where Fe^{3+} attached to six H_2O which are called “coordinated water”, and the other place is the available eight sites of the unit cell which is hosting the other water molecules which are called “zeolitic water’’.

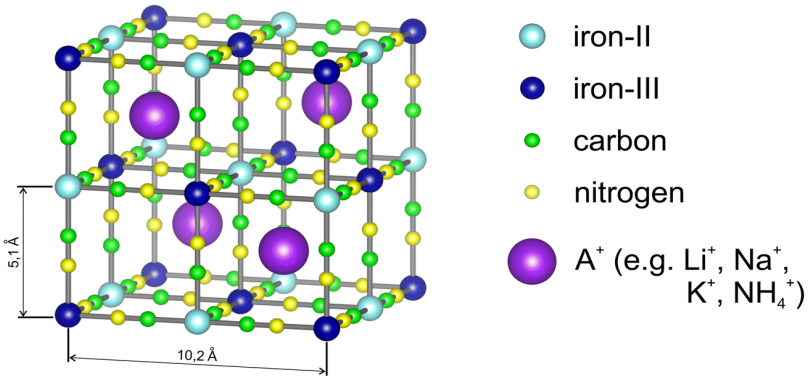


Fig-1.2 –Structure of prussian blue

Structure of Prussian blue according to the Keggin and Miles model from 1936 , with 4 alkali ions in alternate octants (soluble Prussian blue). For insoluble Prussian blue, Keggin and Miles suggested 11/3 Fe^{3+} instead of 4 A^+

Besides that PB structure can be modified substitutional or interstitially with maintaining the structure of the lattice to give the Prussian blue analogues (PBA) shown in Fig.1.4. The substitutional modification involves the replacement of iron atoms with conventional transition metals such as

manganese, zinc, copper, nickel, cobalt, other materials such as lanthanide elements with special electronic configurations Mo, Gd and non-transition metal ions (Ga, Al and Bi) etc.

Today, the exact formulation, composition, and structure of Prussian blue or ferric ferro cyanide are usually described by a model, which has been developed in the research group of Andreas Ludi at the University of Bern. Ludi et al. were the first in the twentieth century to be able to produce larger crystals of (insoluble) Prussian blue with an edge length of about 0.05 to 0.1 mm by dissolving $FeII(CN)_6^{4-}$ (i.e., ferrocyanide or hexacyanoferrate(II)) and Fe^{3+} or Fe^{2+} in concentrated hydrochloric acid (10 mol/L), in which Prussian blue is really soluble. Prussian blue was slowly precipitated from this yellow solution by very slow in diffusion of water, i.e., dilution of the hydrochloric acid. However, these are extreme conditions that are characterized by the complete absence of potassium or other alkali metal cations and high concentrations of protons and chloride anions. Their structural investigations came to the result that the ratio between Fe(III) and $Fe^{II}(CN)_6^{4-}$ of 4:3 can be explained by the fact that $Fe^{II}(CN)_6^{4-}$ vacancies are present in the cubic Prussian blue lattice, “the vacant sites being randomly distributed.” 100% of the Fe^{III} places are occupied, but only 75% of the $Fe^{II}(CN)_6^{4-}$ places. Water molecules are placed both in the zeolitic cavities , the octants, and instead of the empty nitrogen sites of the missing ferrocyanide units. The exact Ludi formula $Fe^{III}_4[Fe^{II}(CN)_6]_3 \cdot 14\text{-}16H_2O$ acquired widespread acceptance.

In 1980, the exact positions of the 14 to 16 water molecules were determined for the Ludi structure . It was determined that besides the six water molecules which are coordinated to Fe(III) at the empty nitrogen sites as shown in Fig.1.3 , there are four non-coordinated water molecules inside the vacancy, and the remaining four to six non-coordinated water molecules are found in the 8 octants.

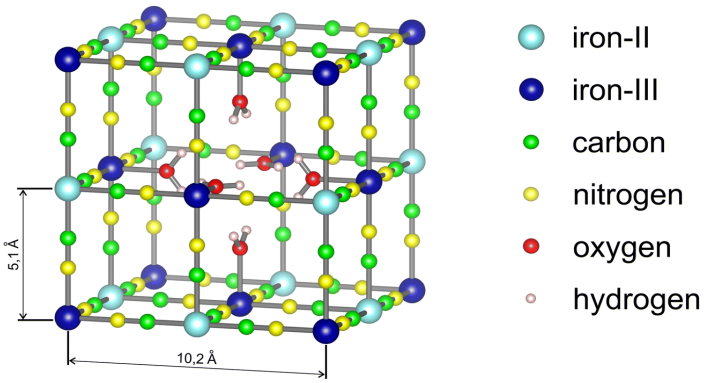


Fig.1.3- Structure of (insoluble) Prussian blue according to Ludi and coworkers

Introduction to Supercapacitors :

In today's energy-dependent world, electrochemical devices for energy storage and conversion such as batteries, fuel cells and electrochemical supercapacitors (ESs) have been recognized as the most important inventions among all energy storage and conversion technologies. The electrochemical supercapacitor, also known as a supercapacitor, ultracapacitor or electrochemical double-layer capacitor is a special type of capacitor that can store relatively high energy density compared to storage capabilities of conventional capacitors. ES devices posses several high impact characteristics such as fast charging capabilities, long charge- discharge cycles and broad operating temperature ranges. As a result, their use in hybrid and electrical vehicles, electronics, aircraft and smart grids is widespread. Although ES systems still face some challenges, such as relatively low energy density and high cost, further development will allow ES to work as power devices in tandem with batteries and fuel cells and also function as stand-alone high energy storage devices. For energy storage devices, energy density and power density are very important parameters for characterizing the performance of the devices. Energy density defines the amount of energy that can be stored in a given volume of weight of the material. Power density defines the total energy per unit time which can be stored into the device. So, the ideal storage device should have both high energy density and high-power density. To compare the energy and power capabilities a representation known as the Ragone plot or diagram has been developed has been shown in the figure1.5

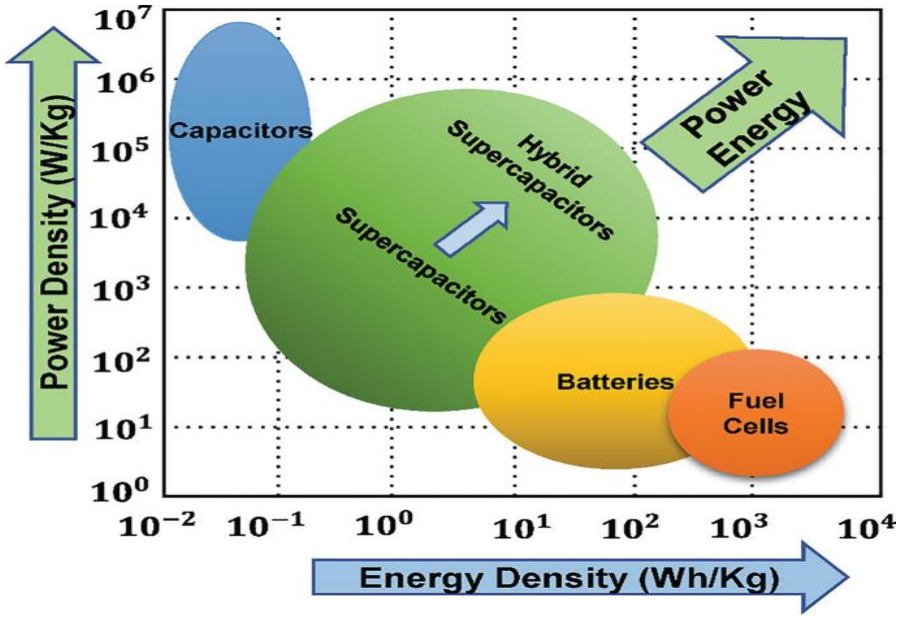


Fig1.5- Ragone plot

Batteries have high energy density, but poor power density. Fuel cells have the highest energy density and lowest power density. By contrast with them, supercapacitors could posses high power density

and notable increased high energy density. Supercapacitor is also known as electric double-layer capacitor (EDLC), super condenser, pseudo capacitor or ultracapacitor. Compared to conventional electrolytic capacitors the energy density is typically in the order of hundreds of times greater in supercapacitors. In comparison with conventional batteries or fuel cells, EDLCs also have much higher power density. The present energy crisis has created a growing demand for efficient, portable and high-power energy storage devices. Supercapacitors are fast emerging as a promising potential solution to this problem.

➢ Classification of Supercapacitors:

Based upon present scenarios, supercapacitors can be divided into three general classes: electrochemical double-layer capacitors, pseudo capacitors and hybrid capacitors. Each class is characterized by its unique mechanism for storing charge. These are respectively, non-Faradaic, Faradaic and a combination of the two. Faradaic processes,such as oxidation-reduction reactions, involve the transfer of charge between electrode and electrolyte. A non-Faradaic mechanism, by contrast, does not use a chemical mechanism. Rather charges are distributed on surfaces by physical processes that do not involve the making or breaking of chemical bonds. A graphical taxonomy of the different classes and subclasses of supercapacitors is presented in the below figure.

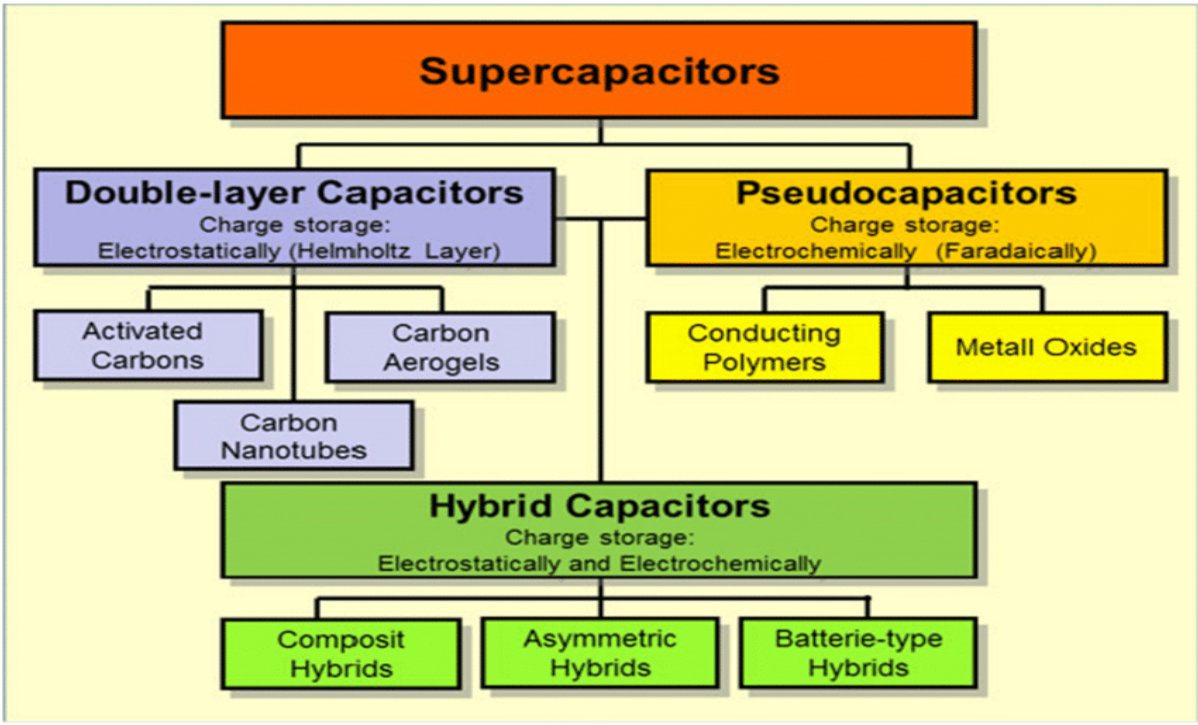


Fig.1.6- Types of Supercapacitors & its Charge Storage Mechanism

Three types of ES exist – a) EDLC (Electric double layer supercapacitor), b) Pseudocapacitor, c) Hybrid capacitor

a) **EDLC :** When an electrically conductive electrode is immersed in an ion conductive electrolyte solution, a double layer spontaneously forms due to the accumulation of charges. An EDLC (Fig.1.7) is the simplest supercapacitor, where the charge is physically stored by electrostatic charge adsorption at the electrode-electrolyte interface i.e., no faradaic charge transfer occurs

The concept of the existence of the double layer at the surface of a metal being in contact with an electrolyte was proposed by Helmholtz in 1879. It was the first theoretical model which assumed the presence of a compact layer of ions in contact with the charged metal surface. The Gouy and Chapman model suggested the involvement of a diffuse double layer in which the accumulated ions, due to the Boltzmann distribution, extend to some distance from the solid surface. In 1924, Stern suggested that the electrified electrode-electrolyte interface includes both the Helmholtz layer and the diffuse layer. In 1947, Graham pointed out the specific adsorption of ions according to their distance of closest approach at the metal surface. In consecutive developments, it became clear that the dipolar solvent must interact with the charged metal surface. Parsons showed that the dielectric constant of the

solvent in the compact layer of adsorbed molecules is much lower compared to the outer region and approaches the limiting Maxwell value. The change in the electric potential within the double layer is shown in Fig.1.7. Two planes are basically associated with the double layer. The inner Helmholtz plane (IHP), passes through the centers of specifically adsorbed ions and the outer Helmholtz plane (OHP), passes through the centers of hydrated ions which are in contact with the metal surface. The electric potentials linked to IHP and OHP can be written as and respectively. The diffuse layer is developed outside the OHP. The concentrations of cations in the diffuse layer decreases exponentially with the distance from the electrode surface. It is considered that the electrode is charged negatively. The electric potential is practically constant throughout the metallic phase except for the layers located near to the electrolyte solution, where a discontinuity in the metal structure occurs and the wave properties of the electron are found (the jellium model).

The thickness of the electric double layer is usually represented in terms of Debye Huckel length (k^{-1}) :

$$k^{-1} = \left(\frac{€r€0kBT}{2coe2zi2}\right)^{1/2}$$

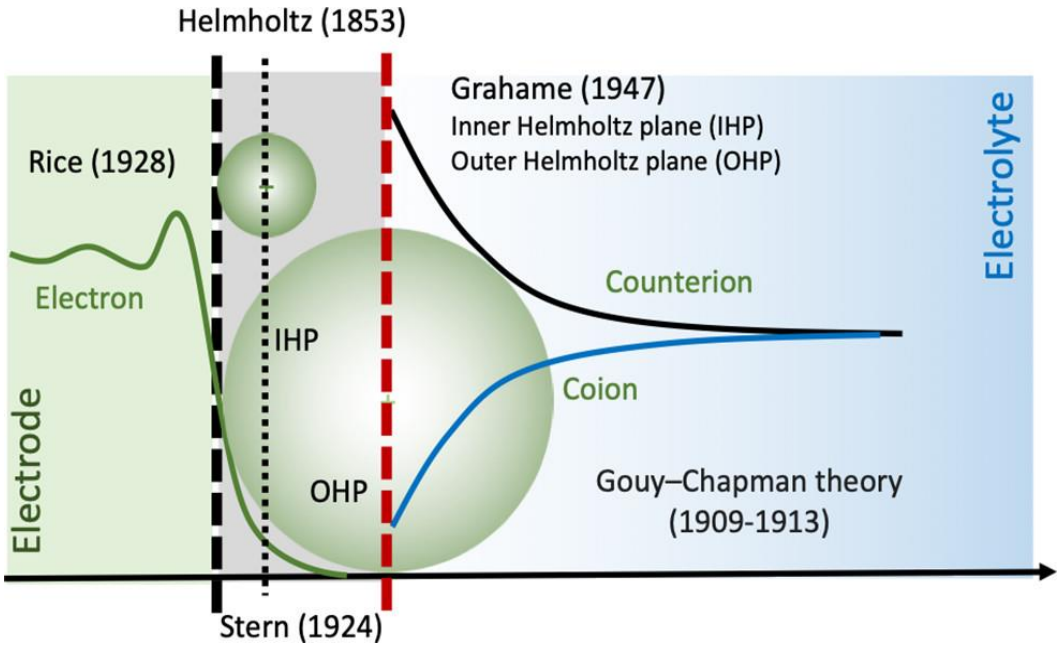


Fig.1.7- EDLC Model

Where c_0 is the bulk concentration of the z:z electrolyte, ε_r and ε_0 is the dielectric constant of electrolyte and free space respectively, T is the temperature, is the ion charge, e is the elementary charge. Higher concentration and ion charge results reduced thickness of the double layer. The thickness of the double layer is also depend on the potential difference between electrode potential and the potential of zero charge that means larger the potential difference, smaller is the Debye Huckel length.

- **Limitations :** Experimentally the specific capacitance of pure carbon based EDLC is small due to the finite conductivity, unavailability of all of the surface sites and the limited ion accessibility of the porous structure. As a result, supercapacitors based on EDLC electrode materials can store energy in the range of 3-10 Wh kg^{-1}.

Pseudocapacitor : To increase the capacitance of ESs , some electrochemically active materials are investigated for electrode use to provide much higher pseudocapacitance than double layer capacitance. For pseudocapacitance, a faradaic charge transfer in the electrode porous layer occurs through a thermodynamically and kinetically favoured electrochemical oxidation-reduction (redox) reaction. The strong dependency of the change in charge quantity (dq) on electrode potential (dv), represented as ( ) is called the pseudocapacitance created by the redox reaction. The electrochemical reversibility of employed redox material in a pseudocapacitor normally depends on the structural and chemical reversibility of the reaction mechanism.

Three types of faradaic processes occur in the case of pseudocapacitor i) Under potential deposition (UPD) ii) Redox pseudocapacitance iii) Intercalation pseudocapacitance

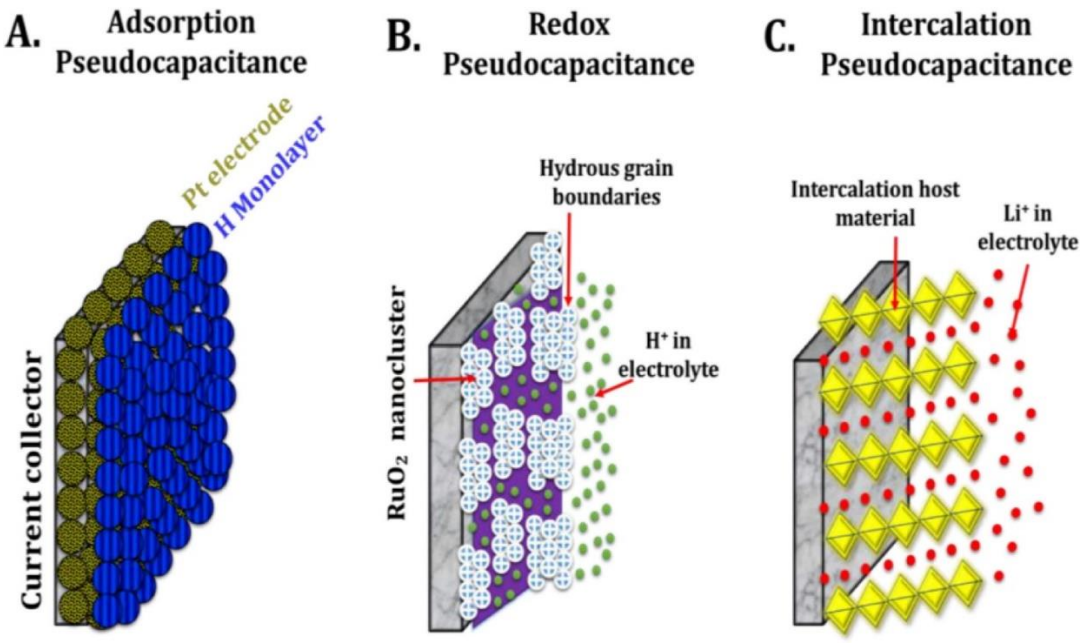


Fig1.8-Mechanism of pseudocapacitance

i) Under potential deposition : Under potential deposition is well known for the adsorption of hydrogen atoms on catalytic noble metals such as Au, Pt, Rh, Ru, and Ir.

The good reversibility of the charge-discharge kinetics is a prime factor in obtaining favourable specific capacitances and power densities for pseudocapacitive materials. However, the operational potential ranges are usually small, only 0.3-0.6 V and the capacitance values are potential dependent for the under potential deposition process. That results limited energy density compared to other pseudocapacitive systems.

ii) Redox pseudocapacitance: Important requirements that should be followed by the redox couples are a) It should exhibit multiple redox states and remain stable over a large potential window. b) It should be very electrically conductive and have accessible structure needed to support performance. c) a high diffusion rate of charge balancing ions within the matrix. Pseudocapacitance based on redox reactions, uses electron transfer between an oxidized species Ox (e.g., RuO_2, MnO_2 or p-doped conducting polymers) and a reduced species, Red (e.g., RuO_2–z(OH)z, MnO_2–z(OH)z, or n-doped conducting polymers). These reactions are usually described as electrochemical adsorption of cations on the oxidized species surface accompanying fast and reversible electron transfer across the interface between the electrode and the electrolyte

iii) Intercalation pseudocapacitance : Pseudocapacitance can also occur in the case of ion insertion or intercalation into layered crystalline materials

The intercalation is accompanied by a change of metal valence to maintain electrical neutrality. The cathode intercalation mechanism requires a faradaic charge or driving force for the lithium cation to adsorb and deposit into the cathode material lattice structure. The electrochemical performance of a

cation intercalation pseudocapacitor is described as “transitional” behaviour between Li-ion batteries and supercapacitors. The intercalation pseudocapacitance is characterized by fast ion transport kinetics, short charge time, high rate capability, and long cycling stability, whereas battery materials are limited by solid-state diffusion, resulting in lower power density.

c) Hybrid Capacitor： To achieve optimum coupling between double layer capacitance and pseudocapacitance, composite electrodes seems more effective by using high surface area carbon to increase deposition mass of the pseudocapacitive component.

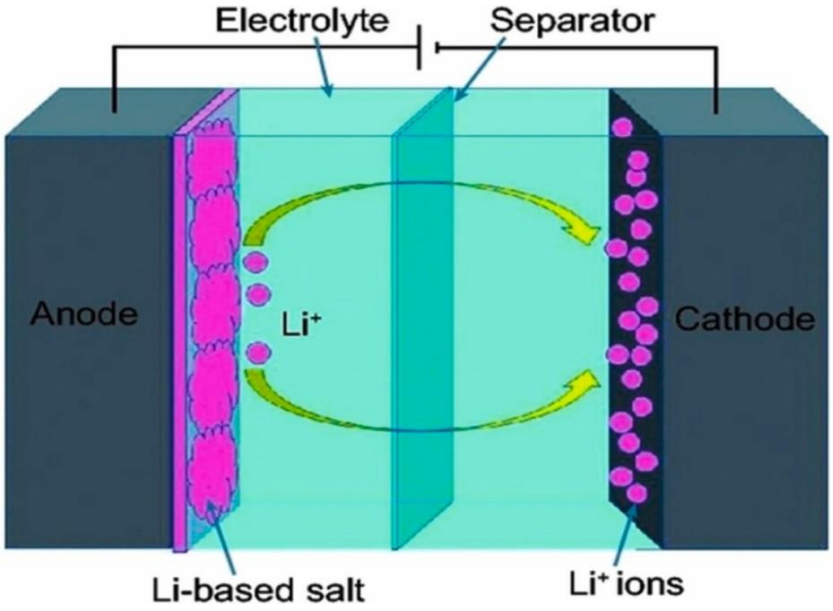


Fig. 1.9 –Design of hybrid capacitor .In designing hybrid ES devices, asymmetric configuration (e.g. one electrode consists of electrostatic carbon material while the other consists of faradaic capacitance material)

Discussions on different charge storage mechanism by the concept of Cyclic Voltammetry (CV) and Galvanostatic Charge Discharge (GCD) analysis :

Faradaic and non-Faradaic both of these processes are characterized by a current i that is directly proportional to the charge-discharge rate

$$i=av^b$$

Here a, b are adjustable parameters. Whereas the value of b equals to 1 and 0.5 specifies capacitive and diffusion controlled process respectively.

In the case of EDLC rectangular cyclic voltammogram with a voltage independent current and a linear triangular shaped charge-discharge curve as shown in Fig.1.10 a),b),c).

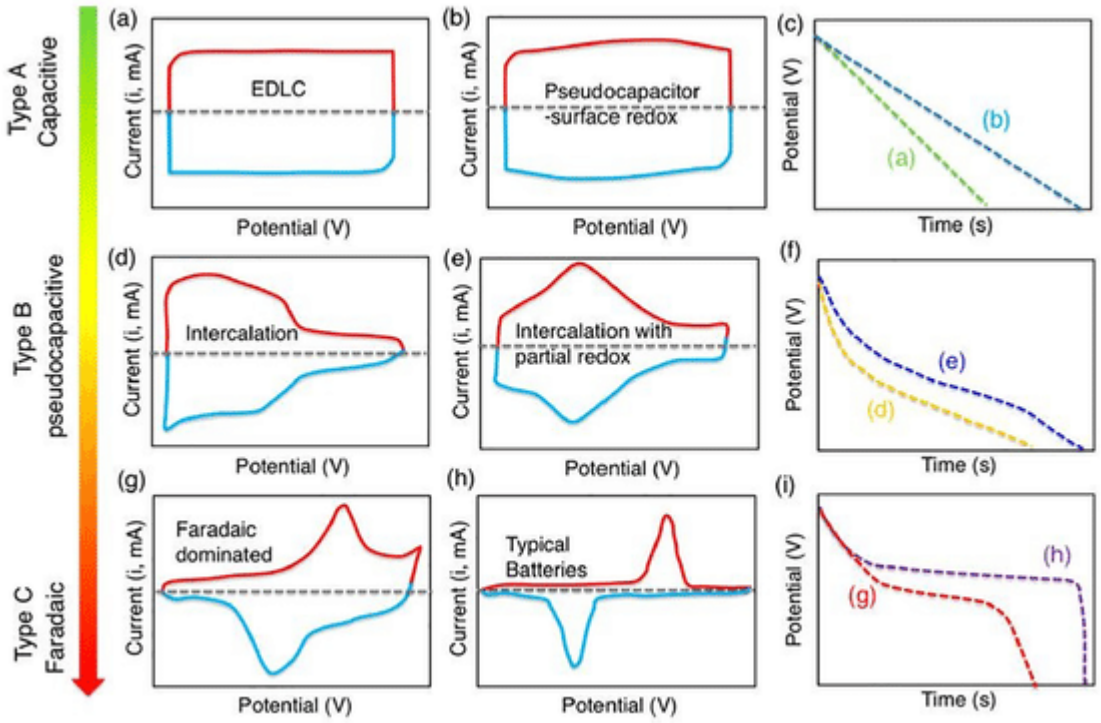


Fig.1.10- rectangular cyclic voltammogram with a voltage independent current and a linear triangular shaped charge-discharge curve

Fig.1.10 d),e),f) shows behaviour involving voltage dependent electrochemical charge transfer i.e. faradaic reaction in pseudocapacitive material which signifies a charge storage mechanism centered between EDLC and battery like ESs.

Fig.1.10 g),h) shows prominent and widely separated peaks associated with the oxidation and reduction of the metal storage (i.e. battery type).

Fig.1.10 i) shows variation of potential with respect to time for the discharge of a battery. The relation is found very nonlinear and characterized by plateaus of nearly constant potential.

1.3.3 Choice of Electrode and Electrolyte

- **Electrode** :

ES device performance is strongly depends on the choice of the electrode materials and electrolytes. Several materials, such as carbon materials (e.g., Activated carbon, Carbon nanotubes, carbon aerogels and graphene etc.), faradaic materials (transition metal oxide, metal hydroxides, metal sulphides and conducting polymers), have been widely investigated as promising electrode materials for ESs.

Additionally, metal coordination electrode materials, such as MOFs, PB/PBAs and POMs have been introduced recently.

Carbon materials :

Carbon materials are the most used electrode materials in fabrication of supercapacitor owing to their high surface area, high mechanical strength, high thermal and electrochemical stability, low cost, availability, established electrode production technologies. Usually, carbon materials store charges electrostatically in the double layer. Therefore the capacitance primarily depends on the surface area accessible to the electrolyte ions. To improve the specific capacitance of carbon materials it is essential to consider the effect of high specific surface area and appropriate pore size distribution, pore shape and structure, surface functionality and electrical conductivity. The presence of functional groups on the surface of carbonaceous materials may introduce faradaic redox reactions, leading to a 5-10% increase in the total capacitance. Usually the measured value of specific capacitance of carbon materials in real ESs are in the range of 75-175 F g^{-1} for aqueous electrolytes and 40-100 F g^{-1} for organic electrolytes.

Faradaic materials :

Pseudocapacitive materials store charge through fast, reversible surface redox reactions and hence exhibit considerably large capacitance values (300-2000 F g^{-1}). This category usually includes transition metal oxides, metal hydroxides, metal sulphides and metal nitrides, such as RuO_2, IrO_2, MnO_2, NiO, Co_2O_3, SnO_2, V_2O_5, MoO and $NiCo_2O_4$, MoS_2, $Ni(OH)_2$, $Co(OH)_2$ and conducting polymers (CPs) such as Polyaniline (PANI), Polypyrrole (PPy), Polythiophene (PTh).

In general, metal oxides can provide higher energy density than conventional carbon materials and better electrochemical stability than polymer materials. They not only store charge electrostatically like carbon materials but also exhibit electrochemical faradaic reactions between electrode materials and ions within appropriate potential windows. RuO_2 is the most studied material because of its wide potential window of 1.2 V, highly reversible redox reactions having three distinct oxidation states, high proton conductivity, remarkably high specific capacitance(720 F g^{-1}) and a long cycle life but their costliness prevents their practical application in ES. But majority of these metal oxides demonstrate very poor conductivity towards electron conduction, which results in an increase of overall resistance of the electrode hampering the power delivery.

The redox reaction in the conducting polymer occurs throughout its entire bulk. During oxidation the ions are transferred to the polymer chain and during reduction the ions are released from this polymer chain into the electrolyte. The processes are highly reversible because the charging and discharging reactions do not involve any structural alterations such as phase changes. Unfortunately, swelling and shrinking of CPs may occur during the intercalating or de-intercalating process which lead to mechanical degradation of the electrode and fading electrochemical performance during cycling, and then limits their usage as electrode materials. To reinforce the stability as well as maximize the

capacitance value nanocomposite based electrode materials such as carbon-carbon composites, carbonmetal oxide composites, carbon-conducting polymer composites can also be used.

- **Electrolyte:**

The electrolyte is a significant constituent in supercapacitors. Electrolyte is the conducting solution of electrolyte salt and solvent which plays an important role in transferring and balancing charges between two electrodes in the cell. The electrolytes are classified into various categories .The interaction between the electrolyte and electrodes in all electrochemical processes significantly influences the electrode-electrolyte interface and internal structure of active materials. The factors influencing the overall performance of supercapacitors are ionic conductivity and mobility, diffusion coefficient, radius of hydrated spheres, solvation, dielectric constant, electrochemical stability, thermal stability and dispersion interaction etc. So the requirements for ideal electrolyte are as follows – a wide electrochemical stable potential window (ESPW), high ionic conductivity, high chemical and electrochemical stability, high chemical and electrochemical inertness to ES components, a wide operating temperature range, well matched with the electrolyte materials, a low volatility and flammability, environmental friendliness, low cost etc.

Aqueous electrolytes :

Aqueous electrolytes have been used extensively in research and development due to their low cost and user friendliness in ES fabrication. Normally, aqueous electrolytes exhibit high conductivity higher than that of organic and IL electrolytes. It is advantageous for lowering the ESR, leading to a better power delivery of ESs. Aqueous electrolytes are classified into three categories: (a) alkaline, (b) neutral, and (c) acidic solutions. Often used aqueous electrolytes are KOH, NaOH, LiOH, Na_2SO_4, H_2SO_4, $(NH4)_2SO_4$, K_2SO_4, Li_2SO_4, $MgSO_4$, $CaSO_4$, $BaSO_4$, KCl, NaCl, LiCl, HCl, CsCl, $CaCl_2$, KNO_3, $LiNO_3$, Na_2HPO_4, $NaHCO_3$, $Na_2B_4O_7$ etc. The main disadvantage of aqueous electrolytes is their relatively narrow ESPW (1.0 V to 1.3 V).

Organic electrolytes :

Organic electrolyte based ESs are currently dominating owing to their high operation potential window (2.5 V to 2.8 V) which can provide a significant improvement in both the energy and power densities. Typical organic electrolytes consist of the conductive salts (e.g., tetraethylammonium tetrafluoroborate (TEABF4)) dissolved in the acetonitrile (ACN), acetone, g-butyrolactone (GBL), and propylene carbonate (PC) solvent.

ESs with organic electrolytes usually offer smaller specific capacitance, lower conductivity, and safety concerns related to the flammability, volatility and toxicity. Basically it requires complicated purification and assembling processes in a strictly controlled environment to remove any residual impurities (e.g., water) that can lead to large performance degradation and serious self-discharge issues. The disadvantage of organic electrolytes is their higher resistivity due to their large size molecules which require a large pore size in the electrodes.

Ionic liquids :

The salts composed of ions (organic cations and organic/inorganic anions) with melting points below 100ºC are called ionic liquids (ILs). Due to their unique structures, physical and chemical properties, ILs have received significant importance as alternative electrolytes. The supercapacitor performance can be improved by the tuneability properties of ILs due to

their large variety (virtually unlimited) of combinations of cations and anions. Ionic liquids have various advantages such as non-flammability, higher thermal and electrochemical stability, high voltage window (3.5 V to 4 V) and insignificant volatility as compared to organic electrolytes.

ILs can be classified into protic, aprotic and zwitter ionic types based on their composition. ILs used for ESs are based on ammonium, sulfonium, imidazolium, pyrrolidinium and phosphonium cations and hexafluorophosphate (PF6), tetrafluoroborate (BF4), bis(trifluoromethanesulfonyl)imide (TFSI), bis(fluorosulfonyl)imide (FSI), and di cyanamide (DCA) anions. The solvent free ILs may have an advantage in solving the safety problems associated with those organic solvents, making IL-based ESs favourable for high temperature applications. Unfortunately, there are several main drawbacks with most ILs, such as high viscosity, low ionic conductivity and high cost, which can limit their application in ESs.

Solid and quasi-solid state electrolytes :

There are three types of polymer based solid electrolytes - solid polymer electrolytes (SPEs), gel polymer electrolytes (GPEs), and polyelectrolytes. GPE based ESs currently dominate due to their higher ionic conductivity than dry SPEs. The weak mechanical strength of some GPEs may lead to internal short circuits, causing safety issues. Dry SPEs normally have lower ionic conductivity and higher mechanical strength than GPEs. The limited contact surface area between solid state electrolytes and electrode materials especially for the nanoporous materials is the main issue which increases the ESR value, reduces the rate performance and results low specific capacitance of ESs.

Introduction to Cyclic Voltammetry

In electrochemistry, cyclic voltammetry (CV) is a type of potentiodynamic measurement. In a cyclic voltammetry experiment, the working electrode potential is ramped linearly versus time. Unlike in linear sweep voltammetry, after the set potential is reached in a CV experiment, the working electrode's potential is ramped in the opposite direction to return to the initial potential. These cycles of ramps in potential may be repeated as many times as needed. The current at the working electrode is plotted versus the applied voltage (that is, the working electrode's potential) to give the cyclic voltammogram trace. Cyclic voltammetry is generally used to study the electrochemical properties of an analyte in solution or of a molecule that is adsorbed onto the electrode.

The CV measurement is normally conducted in a three electrode configuration or electrochemical cell containing a working electrode (W), counter electrode (C) and reference electrode (R) as shown in Fig.1.11. In the case of symmetric cell CV measurements can also be performed using a two electrode test cell by connecting both the reference and counter electrode probes of the potentiostat to one electrode of the test cell, while connecting the working electrode to the other electrode of the test cell. The electrolyte in the three electrode cell is generally an aqueous or non-aqueous liquid solution. The basic principles of three electrode electrochemical cell for cyclic voltammetric experiments are :

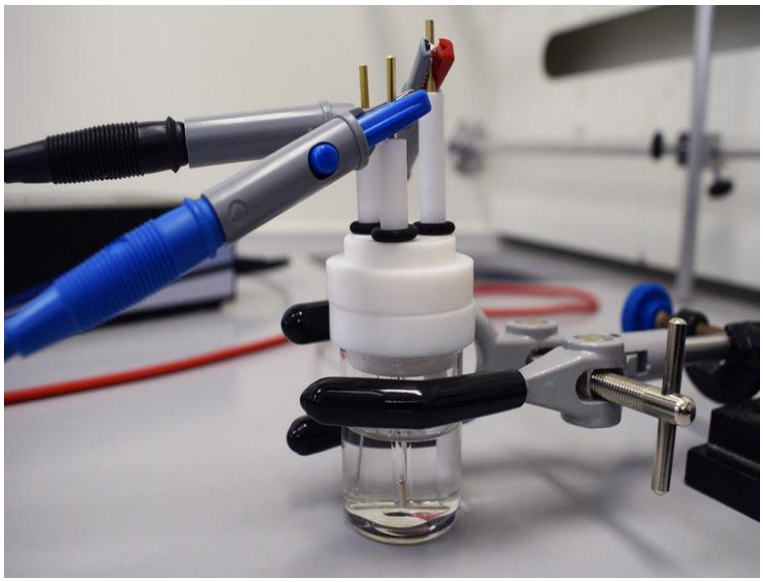


Fig1.11-CV measurement set-up

- **Reference electrode (R) :**

The excitation signal is simultaneously applied across the working and reference electrode. The reference electrode circuit has large resistance so that no current is present in the electrode, therefore providing a stable and reproducible voltage to which the working electrode potential may be referenced. The current that is measured in response to applied potential. Commonly used reference electrodes are aqueous Ag/AgCl, standard hydrogen electrode (SHE) and calomel half cells.

- **Counter electrode (C) :**

The auxiliary electrode provides the current required to sustain the electrochemical reaction at the working electrode. It is also used to prevent large current from passing through the reference electrode. It is basically non-reactive high surface area electrode, commonly platinum gauze.

- **Working electrode (W) :**

The working electrode is the electrode through which the potential is "cycled." It is where the electrochemical reaction takes place and therefore, where the current response is also recorded. The working electrode dimensions are kept small to enhance concentration polarization.

➢ Supporting electrolyte :

A purified supporting electrolyte must be highly soluble in the solvent chosen. It also has to be chemically and electrochemically inert in the conditions of the experiment.

▪ Analysis of CV Curve :

Potentiometry is a way of measuring the electrical potential of an electrochemical cell under static conditions (i.e. no current flow).

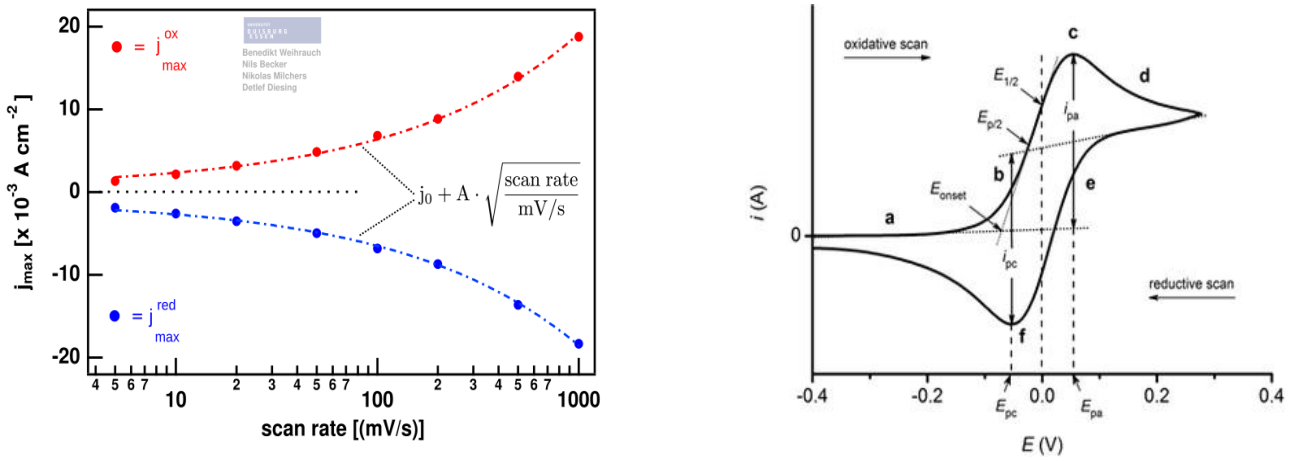


Fig.1.12-(a)Peak current Vs scan rate(b)Current Vs potential graph from CV

For a general reduction or oxidation (redox) reaction, the standard potential is related to the concentration of the reactants (A) and the products (B). This occurs at the electrode/solution interface and can be recognised according to the Nernst equation:

$$aA + ne^- \Leftrightarrow bB \qquad (1.1)$$

Here, E is the electrode potential, $E^{0'}$ is the formal potential, R is the gas constant (8.3145 $J \cdot K^{-1} \cdot mol^{-1}$), T is temperature, n is the number of moles of electrons involved and F is the Faraday constant (96,485 $C \cdot mol^{-1}$).

The term $[B]^b/[A]^a$ is the ratio of products to reactants, raised to their respective stoichiometric powers. You can use this in place of an activity term when the concentration is sufficiently low (< 0.1 $mol \cdot dm^{-3}$).

Under standard conditions of temperature and pressure, the Nernst equation can be written as:

$$E = E^{0'} - \frac{2.303RT}{nF} log \frac{[B]^b}{[A]^a}$$

In the forward scan of working electrode (Fig.1.14.a) the potential first scans positively, from left to right (to positive potential) and later from right to left (to negative potentials) and the current response is measured. The positive scan caused an oxidation of an analyte where the voltage reaches maximum is known as the anodic peak potential (E_{pa}) and results in anodic current (i_{pa}). The reverse negative potential scan caused a typical reduction reaction at the cathodic peak potential (E_{pc}) and results in cathodic current (i_{pc}).

$$Ip = 0.446 nAC_0 \left(\frac{nF\nu D}{RT}\right)^{1/2} \quad (1.2)$$

For electrochemically reversible electron transfer process the Randles-Sevcik equation (Eq. 1.10) describes how the peak current (A) increases linearly with the square root of the scan rate (V s^{-1}), where is the number of transferred electrons in the redox event, is the electrode surface area, is the diffusion coefficient of the oxidized analyte and is the bulk concentration of the analyte.

To evaluate material capacitance, we have to measure this working electrode in the chosen electrolyte using electrochemical CV to record cyclic voltammogram of the particular material from which the capacitance (C_m) can be calculated. Where m is the mass of electroactive material and is potential scan rate.

$$C_m = \frac{i}{2mv} \quad (1.3)$$

And the current (i) which represents the total charge transferred during forward or backward direction CV scanning is obtained by calculating the enclosed area of the CV curves using equation (1.),

$$I = \frac{\int_{v1}^{v2} i dv}{v2 - v1} \quad (1.4)$$

where v_1 and v_2 are the lowest and highest ends of the potential range.

As mentioned above, the voltage scan rate can affect measured capacitance. At lower scan rate complete redox transition also occurred at inner active sites producing high specific capacitance whereas, the capacitance value decreases at higher scan rate due to limited diffusion effect of electrolyte ion within the electrode layer.

- **Analysis of GCD Curve :**

Galvanostatic charge discharge (GCD) curve is one of the most reliable technique to determine capacitance energy density, power density, equivalent series resistance and cycle life of a supercapacitor.

It can be seen that the charge discharge profile (Fig. 1.13) deviate from typical linear variation of voltage with time. It is mainly due to the IR drop that increases with the increase of current rate.

The specific capacitance can be calculated from the GCD profile using equation (1.13),

$$C_m=\frac{i}{m\frac{dv}{dt}} \qquad (1.5)$$

where (i) is the applied current and $\frac{dv}{dt}$ is the average slope of the discharge curve.

$$E=c_m(\Delta v)^2/7.2 \qquad (1.6)$$

$$P=\frac{3600E}{\Delta t} \qquad (1.7)$$

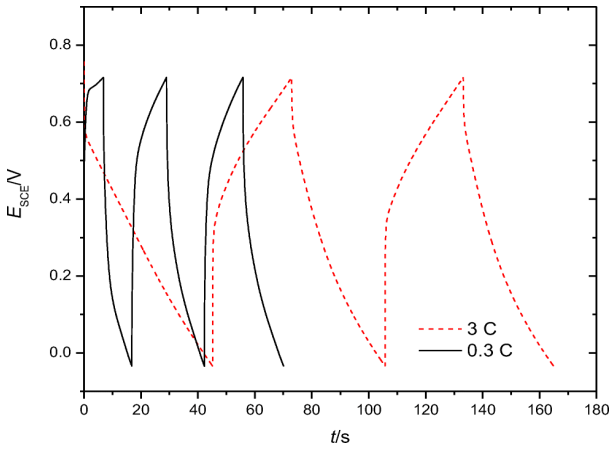


Fig1.13-GCD

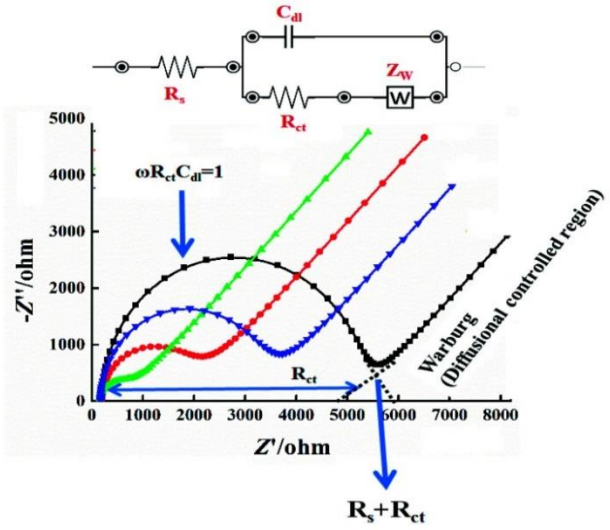
The energy density (Wh kg-1) and power density (W kg-1) of the supercapacitor can be calculated from the GCD profiles at different current densities using the following two equations (1.6) and (1.7).

Here C_m is the specific capacitances of the device as obtained from the GCD at different current densities, Δv is the working potential window and Δt represents different discharge times at different current densities.

Different charging and discharging rates can provide some information about the mass transfer kinetics of an electrode layer. The decrease in specific capacitance with the increasing in current density is due to limited number of interface charges.

Introduction to Electrochemical Impedance Spectroscopy

As a powerful method, electrochemical impedance spectroscopy (EIS) is used to analyse electrical characteristics of the electrochemical system. Any electrochemical supercapacitor (ES) can be represented in terms of an equivalent electrical circuit that comprises a combination of the double layer capacity (Cd), the impedance of the faradaic or non-faradaic process and the high frequency resistance (RΩ), constant phase element and Warburg impedance (W) corresponding to the diffusion of the charged particles. A quasi-reversible charge transfer is considered with the equivalent Randles circuit in EIS measurement as shown in Figure 1.16.a.



EIS measurement is collecting the ES impedance data at the open circuit potential by applying a small perturbation of amplitude (±5 mv to ±10 mv) over a wide frequency (f) range from 1mHz to 1MHz. Normally, amplitude and phase shift of the response signal is measured. Capacitance can be calculated using a linear portion of a log|z| vs log|f| curve, which is called the Bode Plot. EIS can also be expressed as a Nyquist diagram

Fig1.14-EIS data and equivalent circuit

re 1.16.b), where the imaginary part of the impedance, Z(f'') is plotted against the real part of impedance, Z(f').

For an ideally polarized electrode, the impedance consists of the double-layer capacity Cd and the solution resistance RΩ in series. In the impedance plane plot, a straight vertical line results intersecting the Z(f') axis at RΩ at an angle smaller than 90º to the real axis. When a charge transfer proceeds at the electrode, the equivalent circuit consists of Cd and the charge transfer resistance Rct in parallel. So the corresponding Nyquist impedance plot represents a semicircular arc.

The complete Nyquist plot shows the Randles impedance with the semicircle at higher frequencies and the straight line at an angle of 45º to the real axis at lower frequencies. Therefore, from the diameter of the semicircle on Nyquist plot, charge transfer resistance can be obtained. The charge transfer resistance R_{ct} is defined as equation

$$R_{ct} = RT/nFj_o \qquad (1.8)$$

where j_o is the exchange current density, is Faraday's constant, is the universal gas constant, is the number of electrons, and is the temperature

Reference:

Handbook of Nanotechnology : Bharat Bhushan, Springer, 2004

2. Nanostructure and nanomaterials synthesis, properties & applications : Guozhong Cao, Imperial College Press, 2004

3. Fundamentals Of Nanoelectronics : George W. Hanson , Pearson Education, 2009

4. Introduction to Nano : Basic to Nanoscience and Nanotechnology/ Amretashis Sengupta, Chandan Kumar Sarkar, Springer, 2015

5. Mohammadreza Shokouhimehr, Eric S. Soehnlen, Anatoly Khitrin , Soumitra Basu, Songping D. Huang : Inorganic Chemistry Communications 13 (2010) 58–61

6. Anxing Zhou, Liwei Jiang, Jinming Yue, Yuxin Tong, Qiangqiang Zhang, Zejing Lin, Binghang Liu, Chuan Wu, Liumin Suo, Yong-Sheng Hu, Hong Li, and Liquan Chen : ACS App . M t . I t f s 2019 11 41356−41362

7. Feipeng Zhao, Yeyun Wang, Xiaona Xu, Yiling Liu, Rui Song, Guang Lu, and Yanguang Li : ACS App . M t . I t f s 2014 6 11007−11012

8. Bingxing Xie, Liguang Wang, Jie Shu, Xiaoming Zhou, Zhenjiang Yu, Hua Huo, Yulin Ma, Xinqun Cheng, Geping Yin and Pengjian Zuo : ACS Appl. Mater. Interfaces 2019, 11, 46705−46713

9. Yuru Ge, Xuan Xie, Jessica Roscher, Rudolf Holze & Qunting Qu : Journal of Solid State Electrochemistry (2020) 24: 3215–3230

10. Electrochemical supercapacitors : Scientific Fundamentals and Technological Applications/ B.E.Conway, Kluwer Academic/Plenum Publishers

11. Guoping Wang, Lei Zhang and Jiujun Zhang : Chem. Soc. Rev., 2012, 41, 797–828 13. Electroanalytical Methods : Fritz Scholz, Springer, 2010

12. Yuanlong Shao, Maher F. El-Kady, Jingyu Sun, Yaogang Li, Qinghong Zhang, Meifang Zhu, Hongzhi Wang, : Ch . R v. 2018 118 9233−9280

13. Cheng Zhong, Yida Deng, Wenbin Hu, Jinli Qiao, Lei Zhangd and Jiujun Zhang : Chem. Soc. Rev., 2015, 44, 7484

14. Yang Zhao, Zhongxin Song, Xia Li, Qian Sun, Niancai Cheng, Stephen Lawes, Xueliang Sun : Energy Storage Materials 2 (2016) 35-62

15. Shasha Zheng, Huaiguo Xue, Huan Pang : Coordination Chemistry Reviews 373 (2018) 2–21

16.Cheng Zhong, Yida Deng, Wenbin Hu, Jinli Qiao, Lei Zhangd and Jiujun Zhang : Chem. Soc. Rev., 2015, 44, 7484

17. Bhupender Pal, Shengyuan Yang, Subramaniam Ramesh, Venkataraman Thangadurai and Rajan Jose : Nanoscale Adv., 2019, 1, 3807

18. Deepak P. Dubal, Nilesh R. Chodankar, Do-Heyoung Kim and Pedro Gomez-Romero : Chem. Soc. Rev., 2018, 47, 2065

19. Noemie Elgrishi, Kelley J. Rountree, Brian D. McCarthy, Eric S. Rountree, Thomas T. Eisenhart and Jil L. D ps y : J. Ch . Edu . 2018 95 197−206

20. Electrochemical Supercapacitors for Energy Storage and Delivery : Aiping Yu, Victor Chabot and Jiujun Zhang : CRC Press

21. Electrochemical Supercapacitors for Energy Storage and Delivery : Aiping Yu, Victor Chabot and Jiujun Zhang : CRC Press

Chapter-2

INSTRUMENTATION



• Characterization Techniques:

There are several different methods to characterize the sample to determine its phase, morphology, band gap, lattice vibration, crystallite size, interplanar distance, crystal plane etc. Here, in this work also these methods and machineries are being used to determine various properties of the prepared samples. There are mainly 3 types of characterization analysis that one sample can have, i.e.,

➢ Morphological characterization

➢ Phase or crystallographic characterization

➢ Spectroscopic characterization.

These three types of characterization techniques include a wide range of different apparatus and machineries. In this chapter major instruments and their basic working principle which were used in this project will be discussed briefly.

➢ Morphological Characterization:

Morphological characterization defines as the technique or method to get information about the morphology of the sample in micro and nano level. In nanotechnology, ordinary optical microscope can not be used due to their limited focus range which is not able to get the information in nano level. Hence, the need of electron microscopes has been emerged and resulting two types of very important electron microscope, i.e., Scanning Electron Microscope (SEM)

▪ Scanning Electron Microscope (SEM):

One of the most adaptable tools for inspecting and deciphering the morphology of microstructures is the scanning electron microscope (SEM). The surface of the object is routinely scanned by a focused electron beam in a scanning electron microscope (SEM), yielding a significant number of signals. An image is produced from these electron impulses and displayed on a cathode ray tube (CRT). There are two techniques to produce the electron beam:

a) Thermionic emission; b) Field emission.

Thermal energy is used to regulate the source's electron emission to produce thermionic emission. In modern electron microscopes, field emission electron guns (FEG) are a great replacement for thermionic electron guns. Very minute topographic characteristics on the surface of whole or fragmented objects can be observed with a FESEM. Researchers in the fields of biology, chemistry, and physics utilise this technique to examine structures as small a 1 nanometer, or billionths of a millimetre. Organelles and DNA material in cells, synthetic polymers, and microchip coatings can all be studied with the FESEM.

• **Sample preparation for FESEM:** The specimens that can be analysed must be compatible with high vacuum (10-5 mbar), as the SEM is operated under high vacuum. This suggests that liquids and objects made of volatile substances, like water, cannot be directly studied. To prevent contaminating the SEM specimen chamber, fine powder samples must also be firmly connected to a specimen holder substrate. A thin conductive layer must be sprayed or evaporated onto non-conductive materials before they are attached to a conductive specimen container. Common coating materials include carbon, Au, Pt, Pd, and their alloy

• Components of FESEM:

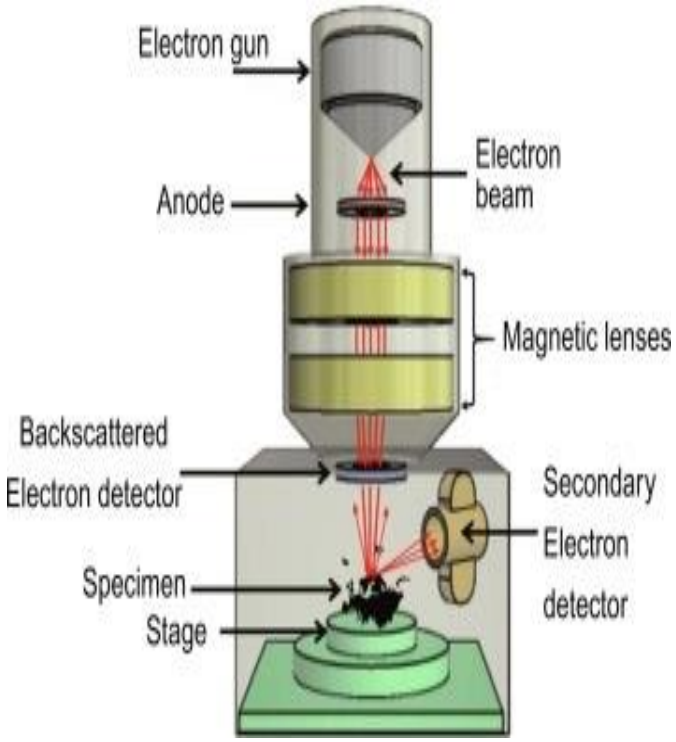


Fig.2.1-Structure of FESEM

▪ **Electron Guns**: Modern FESEM systems require a constant electron beam from the electron cannon that has a high energy, current, a small spot size, configurable and minimal energy dispersion. A variety of electron guns are used in a FESEM system, and the quality of the electron beam produced by each differs greatly. The first tungsten "hairpin" or lanthanum hexaboride (LaB6) cathodes used in the FESEM systems have since been replaced by field emission sources, which provide more current and less energy dispersion. The longevity of the emitter is a crucial consideration when

▪ **Electron Lenses:** Electron beams can be concentrated by electrostatic or magnetic fields. The FESEM system, however, solely employs a magnetic field since an electron beam governed by one has less aberration. Electromagnets can be used to alter the electrons' routes.

• **Condenser Lenses:** The electron beam will diverge after passing through an anode plate from the emission source. The electron beam is brought together and collimated by the condenser lens into a nearly parallel stream. Two rotationally symmetric iron pole pieces make form a magnetic lens, and a copper winding generates the magnetic field. The centre of each pole piece has a hole through which the electron beam can travel. Through a lens-gap between the two pole components, the magnetic

field shapes (focuses) the electron beam. Condenser lens current can be changed to change the focus point's location.

• **Scan Coils:** The scan coils cause the electron beam to be zigzagged as it passes over the object. The development of the image on the display and the scan movement are coordinated. The scan velocity controls both the screen's refresh rate and the amount of noise in the image. In scan coils, upper and lower coils are frequently utilized to avoid the formation of a circular shadow at low magnification.

• **Objective Lens:** The electron beam will diverge below the condenser aperture. The electron beam is de- magnified further and focused into a probe point on the specimen surface using objective lenses. The diameter of the electron beam on the specimen surface (spot size), which affects image resolution, decreases as aperture size and fundamentals of Scanning Electron Microscopy included.

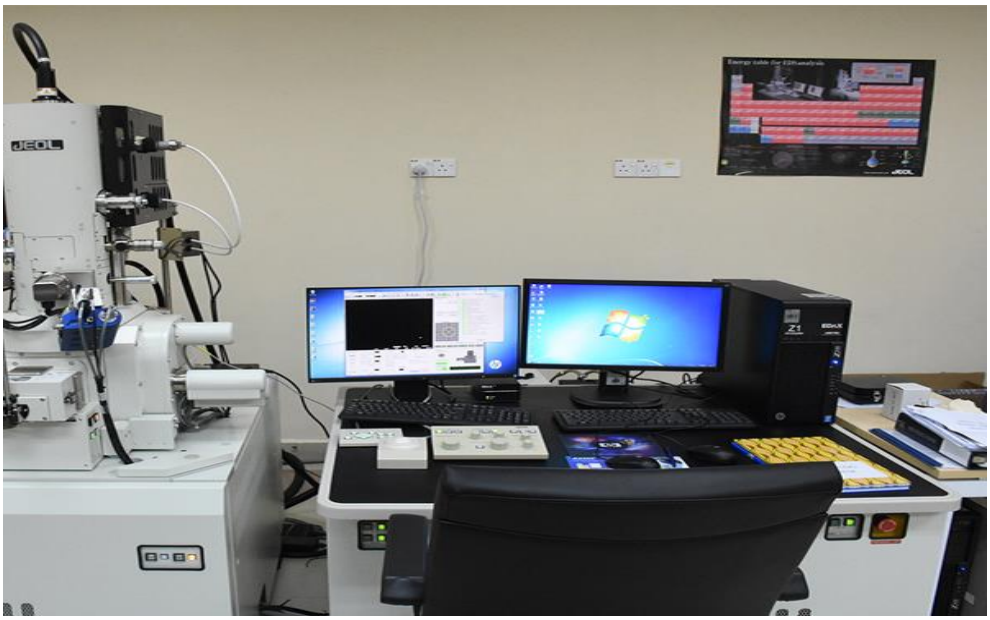


Fig2.2-FESEM set up

•**Stigmator Coil**: The stigmator coils are used to rectify inconsistencies in the beam's xand y deflection, resulting in a perfectly round beam. When the beam is ellipsoidal rather than circular, the picture seems fuzzy and stretched.

• **Object Chamber:** The object is coated with a conductive coating before being set on a particular holder. The object is anchored on a moveable stage and introduced into the high vacuum section of the microscope through an exchange chamber. The secondary electron emission detector (scintillator) is placed behind the object holder in the chamber.

▪ **Image Information:** Complex interactions take place when an electron beam impinges on a specimen surface in a FESEM and stimulates various signals for FESEM inspection. It is possible to collect and display secondary electrons, back scattered electrons (BSEs),

transmitted electrons, and specimen current on a monitor. To determine the specimen's composition, the excited x-ray or Auger electrons are analysed. This part will cover the interactions of the electron beam with the specimen surface as well as the idea behind making pictures out of different signals

➢ **Phase or crystallographic characterization:** The main instrument involved in phase or crystallographic characterization is X-ray Diffraction. It operates with X-Ray to determine the phase of the sample. Apart from that, it is also possible to get information about the crystallographic planes, interplanar distance, crystal size and the lattice structure of the prepared sample

▪ X-Ray Diffraction (XRD):

X-rays are a form of electromagnetic radiation that has high energies and short wavelengths on the order of the atomic spacing for solids. When a beam of x-rays impinges on a solid material, a portion of this beam will be scattered in all directions by the electron associated with each atom or ion that lies within the beam's pathway. Let us now examine the necessary conditions for diffraction of X-rays by a periodic arrangement of atoms. Diffraction occurs when wave encounters a series of regularly spaced obstacles that are capable of scattering the wave and have spacing that are comparable in magnitude to the wavelength. Furthermore, diffraction is a consequence of specific phase relationships established between two or more waves that have been scattered by the obstacles.

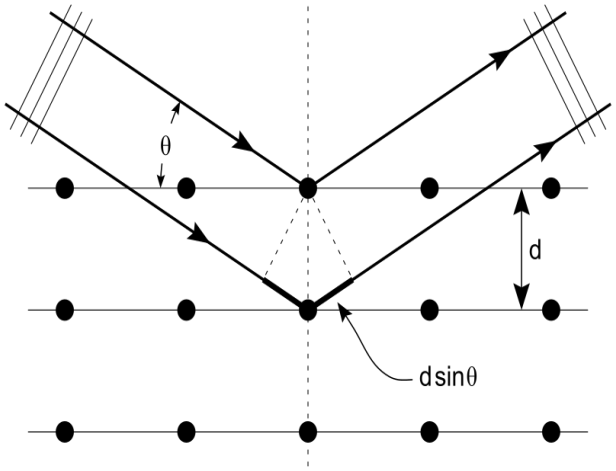


Fig2.3-Diffraction of X-rat at Bragg's plane

a

The phase relationship between the scattered waves, which will depend upon the difference in path length is important. One possibly results when its pathway length is an integral number of wavelengths.

Bragg's Law:

Considering the two parallel planes of atoms, which have the same h, k and l Miller indices and are separated by the interplanar spacing d. Now assuming a parallel, monochromatic and coherent (in-phase) beam of x-rays of wavelength λ is incident on these two planes at an angle of Θ. Two rays in this beam are scattered by atoms A and B. Constructive interference of the scattered waves occur also an angle of Θ to the planes, if the path length difference between these waves is equal to a whole number, n, of wavelengths. So, the condition for diffraction is

$$n\lambda = 2d \sin\Theta \qquad (2.1)$$

- **Working Principle :**

The basic function of a diffractometer is to detect diffracted X-ray beam from sample and to record the diffraction intensity as a function of the diffraction angle ( ) Figure 3.1 demonstrates the geometrical arrangement of X-ray diffractometer which consist of three basic elements an X-ray tube, sample holder and an X-ray detector.

The X-rays are generated by an X-ray tube passes through special slits which collimate the Xray beam. The commonly used Soller slits are made from a set of closely spaced thin metal plates parallel to the figure plane to prevent beam divergence in the direction perpendicular to the figure plane. A divergent X-ray beam passing through the slits strikes the sample. Xrays are diffracted by the sample and form a convergent beam at receiving slits before they enter a detector. The diffracted X-ray beam needs to pass through a crystal monochromator before being received by a detector. Monochromator is used to eliminate wavelengths other than Kα radiation and also decrease the background radiation originating within the sample. As the sample stage and detector are rotated, the intensity of the reflected X-rays is recorded.

- **Determination of lattice parameter :**

As we know that unit cell of a crystal lattice represented by the a,b,c (length) and (interfacial angles) are known as lattice parameters. Knowing the spacings of crystallographic planes by diffraction method, we can determine the crystal structure of materials.

The inter-planar spacing of cubic crystal relates to the lattice parameter (a) by the following equation,

$$d_{hkl} = \frac{a}{\sqrt{h2+k2+l2}} \qquad (2.2)$$

Where ‘ d ’ is the inter-planar distance, ‘a’ is the lattice parameter, ‘h’, ‘k’, ‘l’ is known as Miller indices.

- **Determination of the crystallite size and strain:**

One weakness of the Scherrer method is that it relates the peak width only to the size of the crystallites. While the width of the peaks depends not only on the size of the crystallites but also on the strain of the lattice. This strain is formed in the structure due to different kinds of defects like point defects, grain boundaries, stacking faults, etc.. Williamson-Hall (W-H) method was used to cover all these parameters and gives a better estimate of the crystallite size . In the W-H method, the broadening is deconvoluted into crystallite size and the lattice strain as shown in

$$\beta_{sample} = \beta_{crystalline\ size} + \beta_{lattice\ strain} \quad (2.3)$$

Three distinct models--
uniform deformation model (UDM), uniform stress deformation model (USDM), and uniform defect energy density model (UDEDM)--are created via altering the W-H approach in accordance with different assumptions. The most commonly used form of the W-H route is the uniform deformation model. In UDM the $\beta_{crystalline}$, $\beta_{lattice\ strain}$

$$\beta \text{crystalline size} = \frac{k\lambda}{d cos\theta} \quad (2.4)$$

$$\beta_{lattice\ strain} = 4\epsilon tan\theta \quad (2.5)$$

where ε is lattice strain. Combining two equation

$$\beta cos\theta = \frac{k\lambda}{d} + 4\epsilon sin\theta \quad (2.6)$$

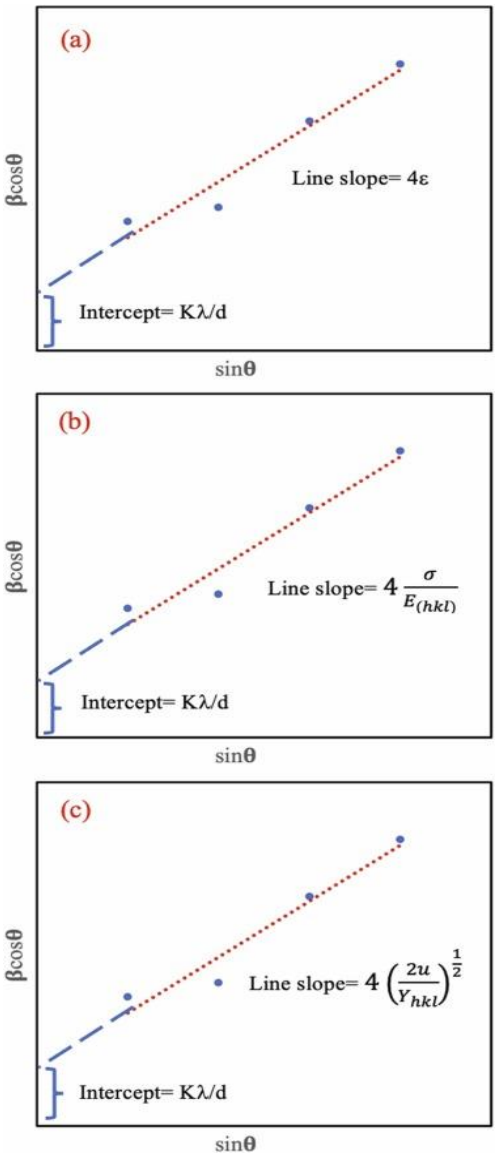


Fig.2.3-WH plot

Here 4Є is the slope of Williamson Hall plot and Kλ/d is the intercept βcosθ axis.

FTIR (Fourier Transform Infrared Spectroscopy) :

Fourier transform infrared spectroscopy is a technique to analyse the structure of molecules by examining the interaction between IR radiation and vibrations in molecules. When a molecule is irradiated by electromagnetic waves within the infrared frequency range, one particular frequency may absorbs the vibrational frequency of the molecule. These absorption frequencies represent the excitation of vibrations of chemical bonds, and thus specifies the type of the bond and the functional groups that are present in a molecule.

In Fourier transform infrared (FTIR) spectroscopy experiment, the intensity of a beam of IR radiation is measured after it interacts with the sample as a function of light frequency which is subjected to Fourier transform to convert infrared spectrum (intensity vs frequency) to intensity-time output. The identity of a pure compound or to detect the presence of specific impurities, atomic arrangement and concentrations of the chemical bonds that are present in the sample can be determined.

Working Principle :

The schematic diagram of an FTIR spectrophotometer is shown in Fig. 2.4. The basic components of FTIR spectrophotometer are Light Source (IR), Interferometer, sample holder, a detector, signal processor and readout

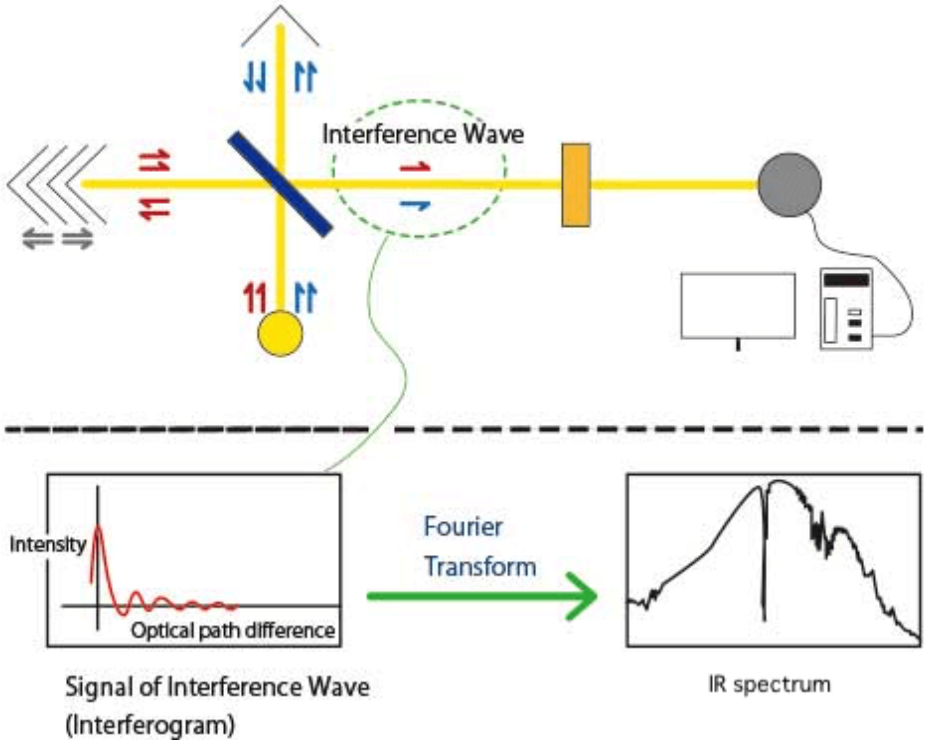


Fig.2.4-Interferrogram and Interferrogram wave signal



Fig2.5- Fourier transform Infrared spectrometer

1. source : Infrared energy is emitted from a black body source. Commonly used sources are Globar filament and Nernst glower.

2. interferometer : The beam of radiation enters the interferometer where the "spectral encoding" occurs.

Interferometer employs a beam splitter which divides the incoming infrared beam into two optical beams. One beam reflects off of a mirror which is fixed in position and the other beam reflects off of a moving mirror. The two beams reflect off of their respective mirrors and are recombined to a single beam when they return at the beam splitter. Depending on the relative path lengths, these two beams interfere with each other.

The interferometer produces interferogram signal which include all of the infrared frequencies "encoded" into it.

3. sample : The beam enters the sample chamber where it is transmitted through or reflected from the sample surface, depending on the type of analysis being performed. This is where specific vibrational frequencies which are uniquely characteristic of the sample, are absorbed.

4.detector : The beam passes to the detector for final measurement. The detector measures the interferogram signal.

5. computer : The digitized signal is sent to the computer to carry out Fouriertransformation. Finally the sample infrared spectrum is presented to the user for interpretation.

UV-Visible Spectroscopy

Ultraviolet−Visible spectroscopy is a widely used analytical method for the quantitative and qualitative characterization of nanomaterials and nanostructures. This method is important to both determine the concentration and study the electronic structure. UV-Visible spectral study is also used to determine the optical band gap.

The basic principle of quantitative UV-Vis spectroscopy lies in comparing the extent of absorption of a sample solution with that of a set of standards under radiation of selected wavelength through the application of Beer-Lambert law. The Beer-Lambert law states that the absorbance of a solution is directly proportional to the concentration of the absorbing species in the solution and the path length.

According to Beer-Lambert's law,

$$A = log_{10}(I_0/I) = \epsilon CL \qquad (2.7)$$

Where, A is measured absorbance, is the intensity of light passing through reference cell, is the intensity of light passing through sample cell, is the molar extinction coefficient, is the concentration of the light absorbing substance and is the path length of the sample.

Extinction coefficient or the integral absorption over an absorption band gives the magnitude of the transition dipole moment and are also dependent on geometry and molecular structure.

The light sensitive detector measures the intensity of light transmitted from the cuvettes and passes the information to a meter that records and displays the value to the operator on an LCD screen. The sample beam and reference beam both are measured at the same time. The intensity of the sample beam is defined as I and the intensity of the reference beam is defined as I0. Over a short period of time, the Spectrometer automatically scans all the component wavelengths in the manner described. The ultraviolet (UV) region scanned is normally from 200 to 400 nm, and the visible region is from 400 to 800 nm. A complete spectrum of the absorption at all wavelengths is recorded.

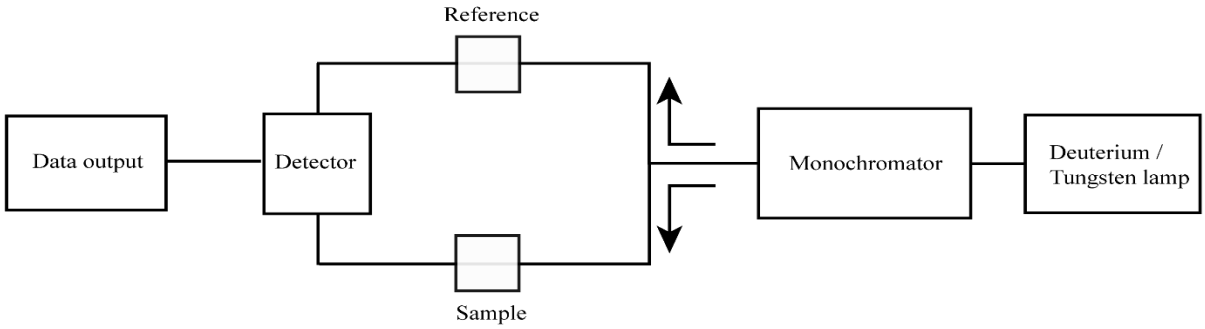


Fig.2.6-Schematic diagram of UV Vis spectroscopy

Working Principle :

UV-Visible spectrophotometers consist of a number of fundamental components : Light Sources (UV and VIS), monochromator, sample holder, a detector, signal processor and readout. The radiation source used is often a tungsten filament, a deuterium arc lamp which is continuous over the ultraviolet region, and more recently xenon arc lamps for the visible wavelengths. The commonly used detector is a photodiode or a charge coupled device (CCD). Photodiodes are used with monochromators, so that only light of a single wavelength reaches the detector. When measuring absorbance at the particular region, the other lamp has to be turned off. Fig. 2.6 shows schematic diagram of UV−Vis Spectrophotometer.The light source is monochromator which splits the incident beam of light into two equal intensity beams (sample and reference beam) by a half mirrored device before it reaches the sample. The sample beam, passes through a cuvette containing a solution of the compound being studied in a transparent solvent and the reference beam, passes through an identical cuvette containing only the solvent. Quartz or fused silica cuvettes are required for UV−Vis spectroscopy.

The light sensitive detector measures the intensity of light transmitted from the cuvettes and passes the information to a meter that records and displays the value to the operator on an LCD screen. The sample beam and reference beam both are measured at the same time. The intensity of the sample beam is defined as I and the intensity of the reference beam is defined as I0. Over a short period of time, the Spectrometer automatically scans all the component wavelengths in the manner described. The ultraviolet (UV) region scanned is normally from 200 to 400 nm, and the visible region is from 400 to 800 nm. A complete spectrum of the absorption at all wavelengths is recorded.

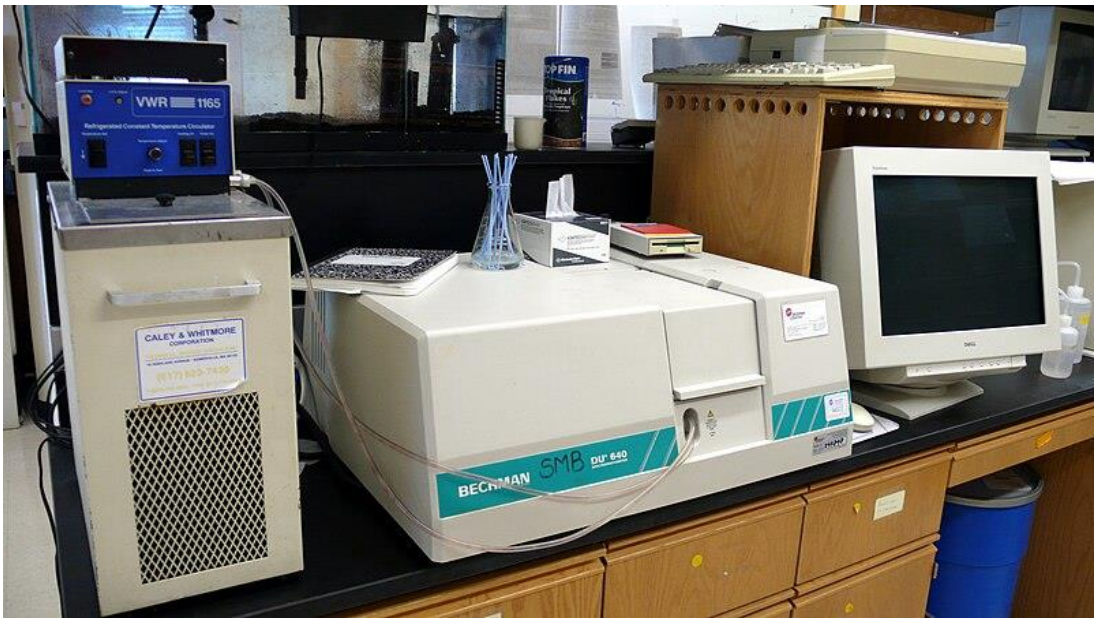


Fig2.7-UV Vis spectrometer

Band gap determination :

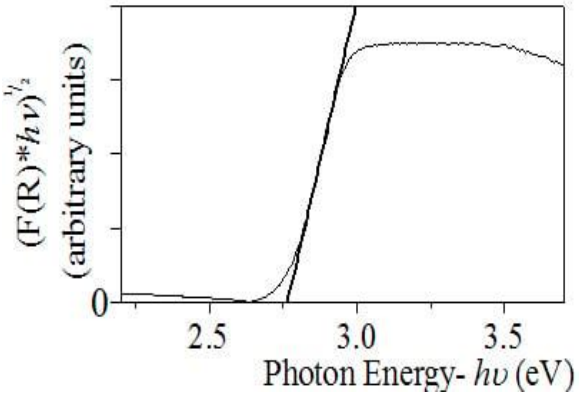
Using the recorded data of absorption spectrum in the whole range of wavelength, we can calculate the absorption coefficient ( ) of the material.

The relation between absorption coefficient and photon energy was deduced by Tauc and represented as,

$$(\alpha h\gamma)^{1/n}=A(h\gamma-E_g) \qquad (2.7)$$

Where is the absorption coefficient, assumes values like 2 and 1/2 in accordance with indirect and direct allowed transitions and , is photon energy, is band gap and A is proportionality constant

Fig2.8-Tauc Plot



According to equation the plot of $(\alpha h\gamma)^{1/n}$ versus hγ must be a straight line and from its intercept on the axis, band gap of the material can be determined.

Photoluminescence Spectroscopy:

The basic instrumental needs for monitoring fluorescence and phosphorescence—a source of radiation, a means of selecting a narrow band of radiation, and a detector—are the same as those for absorption spectroscopy. The unique demands of both techniques, however, require some modifications to the instrument designs seen earlier in Figure 10.25 (filter photometer), Figure 10.26 (single-beam spectrophotometer), Figure 10.27 (double-beam spectrophotometer), and Figure 10.28 (diode array spectrometer). The most important difference is the detector cannot be placed directly across from the source. Figure 10.52 shows why this is the case. If we place the detector along the source's axis it will receive both the transmitted source radiation, PT, and the fluorescent, If, or phosphorescent, Ip, radiation. Instead, we rotate the director and place it at 90o to the source.

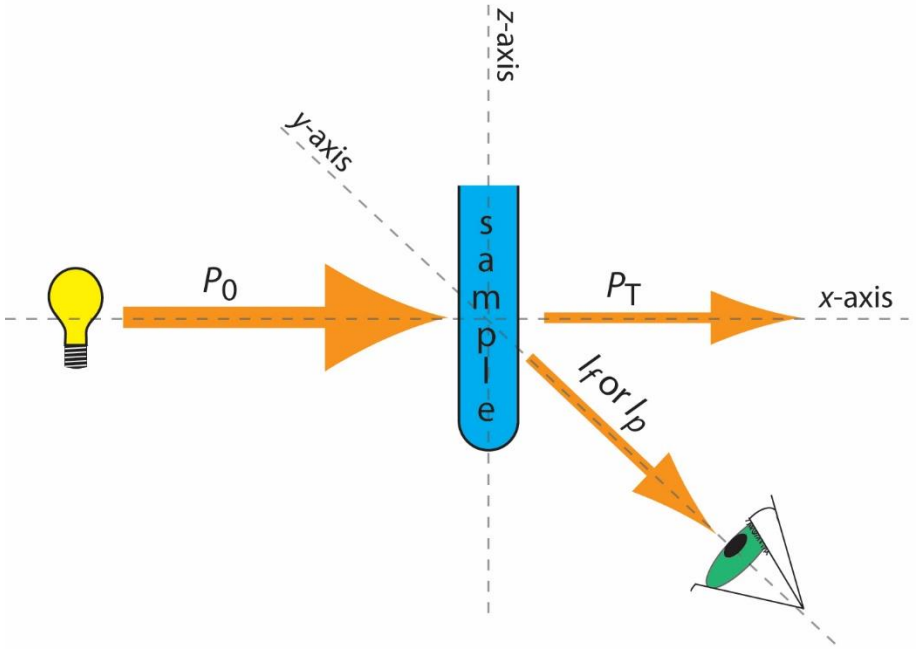


Fig2.9-Schematic diagram showing the orientation of the source and the detector when measuring fluorescence and phosphorescence

Following figure shows the basic design of an instrument for measuring fluorescence, which includes two wavelength selectors, one for selecting an excitation wavelength from the source and one for selecting the emission wavelength from the sample. In a **fluorimeter** the excitation and emission wavelengths are selected using absorption or interference filters. The excitation source for a fluorimeter is usually a low-pressure Hg vapor lamp that provides intense emission lines distributed throughout the ultraviolet and visible region (254, 312, 365, 405, 436, 546, 577, 691, and 773 nm). When a monochromator is used to select the excitation and emission wavelengths, the instrument is called a **spectrofluorimeter**. With a monochromator the excitation source is usually high-pressure Xe arc lamp, which has a continuous emission spectrum. Either instrumental design is appropriate for quantitative work, although only a spectrofluorimeter can be used to record an excitation or emission spectrum.

Light Sources

Specific light sources are chosen depending on the application.

Arc and Incandescent Xenon Lamps:

The high-pressure xenon (Xe) arc is the most versatile light source for steady-state fluorometers now. It can provides a steady light output from 250 - 700 nm with only some sharp lines near 450 and 800 nm. The reason that xenon arc lamps emit a continuous light is the recombination of electrons with ionized Xe atoms. These ions produced by collision between Xe and electrons. Those sharp lines near 450 nm are due to the excited Xe atoms that are not ionized.

During fluorescence experiment, some distortion of the excitation spectra can be observed, especially the absorbance locating in visible and ultraviolet region. Any distortion displayed in the peaks is the result of wavelength-dependent output of Xe lamps. Therefore, we need to apply some mathematic and physical approaches for correction.

High Pressure Mercury Lamps

Compared with xenon lamps, Hg lamps have higher intensities. The intensity of Hg lamps is concentrated in a series of lines, so it is a potentially better excitation light source if matched to certain fluorophorescence.

Xe-Hg Arc Lamps

High-pressure xenon-mercury lamps have been produced. They have much higher intensity in ultraviolet region than normal Xe lamps. Also, the introduction of Xe to Hg lamps broadens the sharp-line output of Hg lamps. Although the wavelength of output is still dominated by those Hg lines, these lines are broadened and fit to various fluorophores better. The Xe-Hg lamp output depends on the operating temperature.

Low Pressure Hg and Hg-Ar Lamps

Due to their very sharp line spectra, they are primarily useful for calibration purpose. The combination of Hg and Ar improve the output scale, from 200 - 1000 nm.

Other Light Source:

There are many other light source for experimental and industrial application, such as pulsed xenon lamps, quartz-tungsten halogen (QTH) lamps, LED light sources, etc.

Monochromators

Most of the light sources used provide only polychromatic or white light. However, what is needed for experiments are various chromatic light with a wavelength range of 10 nm. Monocharomators help us to achieve this aim. Prisms and diffraction gratings are the two main kinds of monochromators used, although diffraction gratings are most useful, especially in spectrofluorometers.

Dispersion, efficiency, stray light level and resolution are important parameters for monochromators. Dispersion is mainly determined by slit width and expressed in nm/mm. It is prepared to have low stray light level. Stray light is defined as light transmitted by the monochromator at wavelength outside the chosen range. Also, a high efficiency is required to increase the ability to detect low light levels.

Resolution depends on the slit width. There are normally two slits, entrance and exit in a fluorometers. Light intensity that passes through the slits is proportional to the square of the slit width. Larger slits have larger signal levels, but lower resolution, and vice verse. Therefore, it is important to balance the signal intensity and resolution with the slit width.

Optical filters

Optical filters are used in addition to monochromators, because the light passing through monochromator is rarely ideal, optical filters are needed for further purifying light source. If the basic excitation and emission properties of a particular system under study, then selectivity by using optical filters is better than by the use of monochromators. Two kinds of optical filter are gradually employed: colored filters and thin-film filters.

Colored Filters

Colored filters are the most traditional filter used before thin-film filter were developed. They can be divided into two categories: monochromatic filter and long-pass filter. The first one only pass a small range of light (about 10 - 25 nm) centered at particular chosen wavelength. In contrast, long pass filter transmit all wavelengths above a particular wavelength. In using these bandpass filters, special attention must be paid to the possibility of emission from the filter itself, because many filters are made up of luminescent materials that are easily excited by UV light. In order to avoid this problem, it is better to set up the filter further away from the sample.

Thin-film Filters

The transmission curves of colored class filter are not suitable for some application and as such they are gradually being substituted by thin-film filters. Almost any desired transmission curve can be obtained using a thin film filter.

Detectors

The standard detector used in many spectrofluorometers is the InGaAs array, which can provides rapid and robust spectral characterization in the near-IR. And the liquid-nitrogen cooling is applied to decrease the background noise. Normally, detectors are connected to a controller that can transfer a digital signal to and from the computer.

Cyclic Voltametry:

Cyclic voltammetry is the most widely used technique for acquiring qualitive data and information about electrochemical reactions. It offers a rapid location of redox potentials of the electroactive species. A method for measuring the current response of a redox active solution to a linearly cycled potential sweep between two or more pre- set values is called cyclic voltammetry. It is a valuable technique for quickly obtaining details about the redox processes' thermodynamics, the analyte's energy levels, and the kinetics of electronic-transfer reactions. Cyclic voltammetry utilises a three-electrode setup, consisting of a working electrode, reference electrode, and counter electrode, similar to other methods of voltammetry. The electrolyte solution, a reference solution, and the three electrodes are initially introduced to an electrochemical cell in order to perform cyclic voltammetry

▪ Operation:

In cyclic voltammetry the voltage is swept between two values at a fixed rate, however now when the voltage reaches V2, the scan is reversed and the voltage is swept back to V1. A typical voltammogram recorded for a reversible single electrode transfer reaction is shown in below. Again, the solution contains only a single electrochemical reactant. For a reversible electrochemical reaction, the CV record has certain well-defined characteristics.

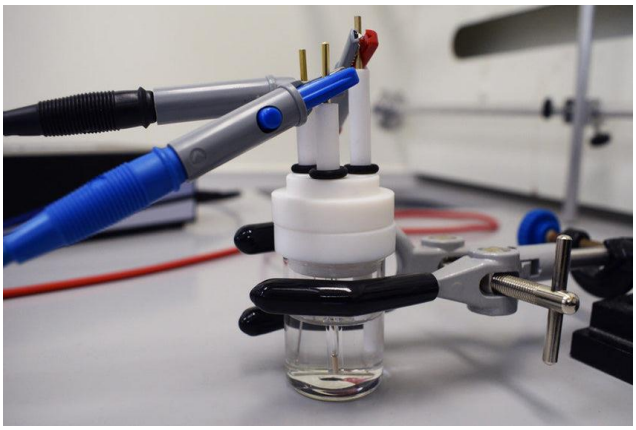


Fig2.10-Cyclic Voltametry

1. The voltage separation between the current peaks is cyclic
2. The positions of peak voltage do not alter as a function of voltage scan rate.
3. The ratio of the peak currents is equal to one.
4. The peak currents are proportional to the square root of the scan rate.

The CV for cases where the electron transfer is not reversible show considerably different behaviour from their reversible counterparts. By analysing variation of peak position as a function of scan rates, it is possible to gain an estimate for the electron transfer rate constant.

Reference:

1.Z. Yang, Z. Z. Ye, Z. Xu and B. H. Zhao, "Effect of the Morphology on the Optical Properties of ZnO Nanos tructured," Physica E: Low-Dimensional Systems and Nanostructures, Vol. 42, No. 2, December 2009, pp. 116- 119. doi: 10.1016/j.physe.2009.09.010

2. Thermo Nicolate, Introduction to Fourier Transform Infrared Spectrometry, © 2001 Thermo Nicolet Corporation.

3. Kortüm, G. Reflectance Spectroscopy: Principles, Methods, Applications; Kortüm, G., Ed.; Springer: Heidelberg/Berlin, Germany, 1969.

4. Frei, R.W.; Frodyma, M.M.; Lieu, V.T. Diffuse reflectance spectroscopy. In Instrumentation for Spectroscopy. Analytical Atomic Absorption and Fluorescence Spectroscopy. Diffuse Reflectance Spectroscopy; Svehla, G., Ed.; Wilson & Wilson's Comprehensive Analytical Chemistry; Elsevier Scientific Publishing Company: Amsterdam, The Netherlands, 1975; Volume 4, Chapter 3, pp. 263–345.

5. Höpe, A. Diffuse Reflectance and Transmittance. In Spectrophotometry: Accurate Measurement of Optical Properties of Materials; Germer, T.A., Zwinkels, J.C., Tsai, B.K., Eds.; Experimental Methods in the Physical Sciences; Academic Press Elsevier Inc.: Amsterdam, The Netherlands, 2014; Volume 46, Chapter 6, pp. 179–219.

6. Lambert, J.H. Lambert's Photometrie. Photometria Sive De Mensura Et Gradibus Luminis, Colorum et Umbrae (1760); Anding, E., Ed.; Ostwald's Klassiker der exakten Wissenschaften; Verlag von Wilhelm Engelmann: Leipzig, Germany, 1892; Volume 31.

7.Bouguer, P. Traité d'optique sur la gradation de la lumiere; l'Abbé de la Caille, M., Ed.; De l'Imprimerie de H.L. Guerin & L.F. Delatour: Paris, France, 1760.

8. Ångström, K. Ueber die Diffusion der strahlenden Wärme von ebenen Flächen. Ann. Phys. 1885, 262, 253–287. [CrossRef]

9. Messerschmitt, J.B. Ueber diffuse Reflexion. Ann. Phys. 1888, 270, 867–896. [CrossRef]

10. Seeliger, H. Zur Photometrie zerstreut reflectirender Substanzen. In Sitzungsberichte der Mathematisch-Physikalischen Classe der k. b. Akademie der Wissenschaften zu München; Franz, G., Ed.; Verlag der K. Akademie: Munich, Germany, 1888; Volume 18, pp. 201–248.

11. Lommel, E. Die Photometrie der diffusen Zurückwerfung. Ann. Phys. 1889, 272, 473– 502. [CrossRef]

12. Uljanin, W. Ueber das Lambert'sche Gesetz und die Polarisation der schief emittirten Strahlen. Ann. Phys. 1897, 298, 528–542. [CrossRef]

13. Wright, H. Die diffuse Reflexion des Lichtes an matten Oberflächen. Ann. Phys. 1900, 306, 17–41. [CrossRef]

14. Pokrowski, G.I. Zur Theorie der diffusen Lichtreflexion. Z. Phys. 1924, 30, 66–72. [CrossRef] 15. Schulz, H. Untersuchungen über die Reflexion a teilweise lichtzerstreuenden Flächen. Z. Phys. 1925, 31, 496–506. [CrossRef]

16. Harrison, V.G.W. The light-diffusing properties of magnesium oxide. Proc. Phys. Soc. 1946, 58, 408–419. [CrossRef]

17. Torrent, J.; Barrón, V. Diffuse Reflectance Spectroscopy. In Methods of Soil Analysis Part 5–Mineralogical Methods; Number 5 in the Soil Science Society of America Book

Series; Ulery, A.L., Drees, L.R., Eds.; Soil Science Society of America Inc.: Madison, WI, USA, 2008; Volume 5, Chapter 13, pp. 367–385.

18. Blake, T.A.; Johnson, T.J.; Tonkyn, R.G.; Forland, B.M.; Myers, T.L.; Brauer, C.S.; Su, Y.F.; Bernacki, B.E.; Hanssen, L.; Gonzalez, G. Methods for quantitative infrared directional-hemispherical and diffuse reflectance measurements using an FTIR and a commercial integrating sphere. Appl. Opt. 2018, 57, 432–446. [CrossRef]

19. Clarke, F.J.J.; Compton, J.A. Correction Methods for Integrating-Sphere Measurement of Hemispherical Reflectance. Color Res. Appl. 1986, 11, 253–262. [CrossRef]

20. Kortüm, G.; Braun, W.; Herzog, G. Prinzip und Meßmethodik der diffusen Reflexionsspektroskopie. Angew. Chem. 1963, 75, 653–661. [Cross Ref]

21. Hanssen, L. Integrating-sphere system and method for absolute measurement of transmittance, reflectance, and absorptance of specular samples. Appl. Opt. 2001, 40, 3196–3204. [CrossRef] [PubMed]

22. Jacquez, J.A.; McKeehan, W.; Huss, J.; Dimitroff, J.M.; Kuppenheim, H.F. An Integrating Sphere for Measuring Diffuse Reflectance in the Near Infrared. J. Opt. Soc. Am. 1955, 45, 781–785. [Cross Ref]

23. Goebel, D.G.; Caldwell, B.P.; Hammond, H.K. Use of an Auxiliary Sphere with a Spectro reflectometer to Obtain Absolute Reflectance. J. Opt. Soc. Am. 1966, 56, 783– 788. [CrossRef]

24. Adams, J.B. Interpretation of Visible and Near-Infrared Diffuse Reflectance Spectra of Pyroxenes and other Rock-Forming Minerals. In Infrared and Raman Spectroscopy of Lunar and Terrestrial Minerals; Karr, C., Ed.; Academic Press Inc.: London, UK, 1975; Chapter 4, pp. 91–115.

25. Photoluminescence Spectroscopy, Physics U600, Adv Lab I – Physics of Waves and Optics – Summer 2004, D. Heiman, North eastern University, 6/1/2004.

26. J. Reichman, Handbook of Optical Filters for Fluorescence Microscopy (Chroma Technology, Brattleboro, 2010).

27. C. Ronda, Luminescence from Theory to Applications (Wiley-VCH, New York, 2008).

28. I. Parreu, J.J. Carvajal, X. Solans, F. Díaz, M. Aguiló, Chem. Mater. 18, 221 (2006).

29. Y. Hong, J. W. Y. Lam, and B. Z. Tang, Chem. Commun., 2009, 4332.

30. Photoluminescence Spectroscopyand its Applications, Ruquan Ye, Andrew R. Barron, OpenStaxCNX module: m38357. 31. M. Anpo, M. Kondo, S. Coluccia, C. Louis, and M. Che, J. Am. Chem. Soc., 1989, 111, 8791.

Chapter-3

LITERATURE REVIEW



Prussian blue and manganese doped Prussian blue as electrode material:

To achieve better electrochemical performance of supercapacitors, development of new electrode materials, especially nanostructured materials, with exceptional charge storage properties and rate capability is essential. Coordination compounds such as PB & PBAs are a new class of electrode materials prepared by chemical interaction of organic linkers and metal ions or clusters owing to their properties such as tuneable pore sizes, high surface area, remarkable porosity, and ordered crystalline structures. Due to the promotion of charge transfer inside its open framework structure and redox behaviour of their metal cations, these nanostructures shows superior electrochemical performance in energy storage device, such as aqueous ion batteries and supercapacitors. Here some of the reviews of past work on this topic have been discussed briefly.

In his work, **Wessells et al**. in 2011 synthesized NiHCF by a co-precipitation method. NiHCF electrodes were prepared by mixing NiHCF, amorphous carbon, polyvinylidene difluoride and graphite in a ratio of 80:9:9:2 in a solution of 1-methyl-2-pyrrolidinone and then deposited on carbon cloth. Electrochemical cycling of NiHCF electrode was performed in aqueous electrolyte (1 M $NaNO_3$ or 1 M KNO_3). For this study, current density of 60 mA g^{-1} was defined as 1C. During either sodium or potassium cycling, a specific capacity of 59 mAh g^{-1} was observed within a narrow 0.3 V range at a C/6 rate. During sodium cycling of NiHCF, 86.5% of its maximum low rate capacity was retained at a rate of 8.3C, and 67% was retained at a very high 41.7C rate. During potassium cycling of NiHCF, the maximum capacity of 85.5% and 66% was retained at a rate of 8.3C and 41.7C respectively. These results demonstrate NiHCF based electrode desirable for use in production of aqueous ion (e.g, Na, K) batteries.

Wang et al. in 2014 reported the electrochemical performance of NiHCF@MnO_2. NiHCF powders were synthesized through co-precipitation method. The strategy for preparing a NiHCF@MnO_2 electrode they followed electrodeposition method in two step. In step I, NiHCF, together with acetylene black, were coated on foam nickel current collector using polyvinylidene difluoride (PVDF) as a binder. In step II, the MnO_2 was anodically electroplated onto the NiHCF electrode. From CV, it was reported that NiHCF@ MnO2 achieved a capacitance of 224 F g^{-1} at a scan rate of 50 mV s^{-1}. From GCD, it was reported that NiHCF@ MnO_2 achieved a capacitance of 199.6 F g^{-1} at a current density of 1 A g^{-1} and 91.6% of this capacitance (182.8 F g^{-1}) was retained during cycling at a current density of 15 A g^{-1}. Obtained results make NiHCF@MnO_2 desirable as supercapacitive electrode materials.

Zhao et al. in 2014 reported the preparation and electrochemical performance of cobalt hexacyanoferrate (CoHCFe) nanoparticles. CoHCFe exhibited specific capacitance of 250 F g-1 in 0.5M Na2SO4 and capacitance retention of 93.5% after 5000 cycles. In addition, CoHCFe was paired up with

a carbon black modified rGO negative electrode to form asymmetric supercapacitor within working voltage of 2.4 V in Na2SO4 and delivered high energy densityof 34.4 Wh kg^{-1} at a power density of 2.5 kW kg^{-1}, and a high power density of 25 kW kg^{-1} at an energy density of 6.7 Wh kg^{-1}. Obtained results make CoHCFe as desirable electrode material for future energy storage applications.

Xiong et al. in 2015 synthesized Prussian blue analogues, $Mn[Fe(CN)_6]_{0.6667}{\cdot}nH2O$ (Mn-PBA), by a simple synthetic co-precipitation route and electrochemical performance was studied. This material exhibited a large capacity of 295.7 mA h g−1 after 100 cycles at a current density of 200 mA g−1 with a high Coulombic efficiency. Obtained results demonstrate MnPBA desirable as anode materials for lithium ion batteries.

Polypyrrole and nickel-cobalt hexacyanoferrate (PPy@NiCoHCF) based nanocomposite was synthesized by Ensafi et al. in 2015 using an electrochemical route. The electrochemical performance of the nanocomposite was studied by CV, GCD and EIS analysis, in an aqueous electrolyte of 0.5M K_2SO_4 and in a non-aqueous electrolyte of 0.5M LiClO4/ethylene carbonate : dimethyl carbonate (EC:DMC). Incorporation of NiCoHCF with PPy showed maximum capacitances of 529 F g^{-1} and 668 F g^{-1} at a current density of 1.0 A g^{-1} in aqueous and non-aqueous electrolytes, respectively. The nanocomposite also showed an excellent stability < 10% drop after 1000 cycles, high specific power density of 5600 W kg-1 and high specific energy density of 87 Wh kg-1 at 10 A g-1. Obtained results make PPy@NiCoHCF desirable as an electrode material to design supercapacitors.

PPy-PB-GO nanocomposite was synthesized by Zou et al. in 2016 via polymerization of pyrrole and formation of Prussian blue nanocubes on GO. The galvanostatic chargedischarge study showed a specific capacitance of 525.4 F g^{-1} at a current density of 5 A g^{-1} in the potential range from 0.2 to 0.6 V, obtained in 1M KNO3 electrolyte. The as-prepared supercapacitor also showed specific capacitance retention of 96% after 2000 cycles. Obtained results signify PPy-PB-GO nanocomposite as a promising electrode material for future energy storage devices.

Zhang et al. in 2017 reported the electrochemical performance of eNiHCF@C composite as a cathode material. Cyclic voltammetry curves at 5 mV s-1 showed one pair of redox peaks within a potential window of 0-1 V (vs. Ag/AgCl), which specified the redox couple of Fe(II)/Fe(III). The galvanostatic charge-discharge profiles showed that the resultant composite exhibited good capacity retentions both for rate capability of 93% at 0.1 A g-1 for 2 A g-1 and cycle stability of 94% after 900 cycles at 0.5 A g-1. The performance of eNiHCF@C composite combined with rGO also showed initial capacity of 94% after 5000 cycles at 2 A g^{-1}.

A new method was demonstrated by Nie et al. in 2017 to enable nickel hexacyanoferrate (NiHCF) nanocrystals as an excellent host for sodium ion storage by functionalization using the solution of 7,7,8,8-tetracyanoquinododimethane (TCNQ) redox molecule. Experimental results indicated that TCNQ molecule bridging with Fe atoms in NiHCF as an electrical highway for electron motion and

conductivity enhancement. The NiHCF/TCNQ exhibited high specific capacity of 35 mAh g−1 after 2000 cycles corresponding to a capacity loss of 0.035% decay per cycle, fast kinetics and good cycling stability due to its high electronic conductivity, open framework structure, nanocrystal, and interconnected mesopores.

Wang et al. in 2017 reported preparation and electrochemical performance of cobalt hexacyanoferrate and reduced graphene oxide based nanocomposite (CoHCF@rGO). This nanocomposite delivered a maximum specific capacitance of 361 F g^{-1} at the scan rate of 2 mV s-1 in Na2SO4 aqueous electrolyte. A CoHCF@rGO electrode and an AC negative electrode were employed to assemble an asymmetric supercapacitor, which operated at a cell voltage of 2.0 V and exhibited a high energy density of 39.6Wh kg-1 at a power density of 1.0 kW kg-1. The results make CoHCF@rGO nanocomposites as a promising electrode material for future supercapacitors.

Zhou et al. in 2017 reported electrochemical performance of cubic PBs. As-synthesized Prussian blue cubes were mixed with PTFE and acetylene black in a weight ratio of 8:1:1 with the help of ethanol to make electrodes. The PB electrode exhibited high reversible capacity of 80 mAh g-1 at the current density of 0.5 A g-1 with 98% capacity retention over 900 cycles due to better potassium ion storage capability and structure stability. A PB positive electrode and an activated carbon negative electrode were employed to assemble a K ion supercapacitor which exhibited good cycling stability at the current density of 2 A g-1 over 1200 cycles, and delivered an energy density of 28 Wh kg-1 at a power density of 214W kg-1.

Sookhakian et al. in 2017 studied the combination of N-graphene and PB as a hybrid battery-supercapacitor electrode which showed highest capacity of 660 C g-1 at 1 A g-1 with 84.7% capacity retention at 6 A g-1 after 1500 cycles. Obtained results suggest N-graphene and PB composite as a promising electrode material for future energy storage devices.

Manganese hexacyanoferrate and multi-walled carbon nanotubes (MnHCF@MWCNTs) based nanocomposite was fabricated by chemical precipitation method at room temperature and further investigated as supercapacitive electrode material by Zhang et al. in 2018. Specific capacities of MnHCF@MWCNTs nanocomposite, MnHCF and MWCNTs were 370.4, 200.1 and 45.8 C g^{-1} at the scan rate of 8 mV s^{-1}, respectively. As-fabricated nanocomposite exhibited rate capability of 370.4 C g-1 and 270.6 C g^{-1} at 1.0 A g^{-1} and 6.0 A g^{-1}, respectively and cycling stability of 87.4% capacitance retention after 2000 cycles at 1.0 A g^{-1}. This nanocomposite based electrode exhibited higher power density of 3867.8 W kg^{-1} with a suitable energy density of 35.7 Wh kg^{-1}. All of these results demonstrate MnHCF@MWCNT nanocomposite desirable as an electrode material for supercapacitors.

Bie et al. in 2018 synthesized Na-MHCFe (M = Mn, Fe, Co, Ni) powder by co-precipitation method. The electrochemical property of Na-MnHCFe, Na-FeHCFe, Na-CoHCFe, and NaNiHCFe samples were

analysed in the voltage range of 2.0-4.2 V. Mn-PBA showed large reversible capacity of 126 mAh g^{-1} at a current density of 30 mA g^{-1} and the Ni-PBA exhibited the best cyclability and rate performance though only 66 mAh g^{-1} was delivered, it showed almost 100% capacity retention over 50 cycles. These remarkable differences in electrochemical behaviours of the PBAs owing to their various properties make them desirable as an electrode material for sodium ion batteries.

Nickel-cobalt hexacyanoferrate and reduced graphene oxide (Ni-CoHCF@rGO) based nanocomposite was synthesized by Qiu et al. in 2018 through a reverse microemulsion method and studied its electrochemical performance. The Ni-CoHCF@rGO delivered high specific capacitances of 466 and 350 F g−1 at current densities of 0.2 A g^{-1} and 10 A g^{-1} respectively. It also delivered high energy density of 41.4 Wh kg^{-1} at a power density of 79.9W kg^{-1} and a high power density of 3957.6Wkg−1 at an energy density of 31.1Wh kg^{-1} and exhibited a capacity retention of 90% after 1000 cycles at a current density of 1A g^{-1}. These results signify Ni-CoHCF@rGO as electrode materials for superior supercapacitors and sodium ion batteries.

In this work, electrochemical performance of a PBA type $Fe_4Fe(CN)6$ cathode was studied by Zhou et al. in 2019 in 5 m Al(CF3SO3)3 Water in-Salt electrolyte (Al-WISE) within a potential window of 2.65 V. The Fe-PBA cathode, exhibited a high discharge capacity of 116 mAh g^{-1} and the superior cycle life of >100 cycles with capacity fading of 0.39% per cycle. All of these results make Fe-PBA desirable as cathode materials for aqueous Al-ion batteries.

MnHCCr electrode was fabricated by Wheeler et al. in 2019 to study its electrochemical performance for sodium ion batteries. Electrochemical measurements were performed on three electrode test cells inside an Ar-filled glovebox. The water-in-salt (WiS) electrolyte used was sodium bis-fluorosulfonylimide (NaFSI) in water, which showed a lower stability limit of −1.07 V vs SHE and a stability window of 2.5 V at current density of 10 μA cm^{-2} Electrochemical performance of MnHCCr exhibited reversible sodium insertion at −0.86 V vs SHE and showed a capacity of 62 mAh g−1 in a high voltage water-in-salt electrolyte. Further reduction in potential than −1.3 V vs SHE in an organic electrolyte (1 M NaClO4 in PC) showed decomposition of the crystalline structure.

Ni-doped cobalt hexacyanoferrate (NiCoHCF) microcubes were synthesized by Qiu et al. in 2019 via co-precipitation method. The electrochemical study of NiCoHCF microcubes as supercapacitive electrode materials showed a high specific capacitance of 466 F g-1 at a scan rate of 5 mV s-1 and good cycling stability of retaining 87.9% after 2000 cycles in 1M Na_2SO_4 under 0-1 V at 2 A g^{-1} when the molar ratio of nickel-cobalt was 1:2 mmol.

Wang et al. in 2019 fabricated MnHCF@PEDOT composite based cathode through in situ polymerization method. In case of GCD study, a current density of 150 mA g-1 was defined as 1C. Due to the synergistic effect of Mn/Fe dissolution, the composite electrode exhibited a high capacity of 147.9 mAh g^{-1} at 0.1C and 78.2% capacity retention after 1000 cycles. Even at a low temperature of -10 ºC, MnHCF@PEDOT also delivered a high capacity of 87.0 mAh g^{-1} and maintained 71.5 mAh g^{-1} (82.2%)

after 500 cycles. These results demonstrate MnHCF@PEDOT desirable as cathode materials for sodium ion batteries.

Tang et al. in 2020 reported $K_xMnFe(CN)_6$ as an attractive cathode candidate for alkali-ion batteries. In this report, electrochemical characterizations were performed to study the intercalation properties including voltages, interstitial sites, migration barriers and structural evolutions of Li+, Na+, K+ in $MnFe(CN)_6$ framework. This material exhibited reversible capacities of 120.9, 117.1 and 104.8 mAh g−1 for Li, Na, and K storage, respectively. Basically the lower migration energy barriers of Na+ result the best rate performances for Na+ storage. The MnHCF electrode showed excellent capacity retention of 83.4%, 82.3% and 92.4% over 100 cycles for Li, Na, and K storage respectively.

Nickel hexacyanoferrate and carbon nanotubes (NiHCF@CNTs) based nanocomposite was fabricated by Yuan et al. in 2020 via a facile route. Transmission electron microscopy (TEM) images characterized that CNTs were universally tangled with randomly aggregated NiHCF particle. NiHCF@CNTs delivered a discharge capacity of 54.1 mAh g^{-1} at 0.1 A g^{-1} and cycle life with a capacity retention of 80% over 10000 cycles at 10 A g^{-1}. Exceptionally, this material exhibited excellent rate capability with a capacity of 47.9 mAh g^{-1} even at an ultrahigh current density of 10 A g^{-1}. Obtained result suggests that developing pseudocapacitive materials is a feasible pathway to upgrade the rate performance of PBAs as cathodes for aqueous Na-ion batteries.

Shi et al. in 2020 reported a novel strategy for in-situ growth of PB micro-nano particles in the electrospun Fe-rich porous carbon fibers. The redox behaviour of the PB@CNF self supporting electrode was investigated by electrochemical measurement. From CV plot, specific capacity of 318.4 F g^{-1} (potassium ions) was achieved. From GCD analysis, this electrode delivered specific capacity of 302.3 F g^{-1} at a current density of 0.3 A g^{-1} in 1M KCl electrolyte owing to the high PB loading, excellent conductivity of PB@CNF and synergistic effect between carbon nanofiber and PB. These obtained results make PB@CNF electrode desirable candidate for use in production of supercapacitors and batteries.

Zhu et al. in 2020 fabricated the Ni_2CoHCF@NF material by growing nickel cobalt hexacyanoferrate (Ni_2CoHCF) on nickel foam via co-precipitation method, and studied its electrochemical performance. The obtained specific capacitance was 1300 F g^{-1} at the current density of 0.5 A g^{-1}. This electrode retained 85.57% of its initial specific capacitance after 2000 cycles at the current density of 10 A g^{-1}. The energy density achieved was 30.59Wh kg^{-1} at the power density of 378.7 W kg^{-1}. Obtained results suggest Ni2CoHCF@NF desirable as an electrode material for supercapacitor.

Song et al. in 2020 fabricated the CoHCF@MnO2 composite material based asymmetrical supercapacitors and studied its electrochemical performance. The CoHCF@MnO2 nanocomposite exhibited a specific capacitance of 385 F g-1 owing to the reversible electrochemical reactions of

Co^{3+}/Co^{2+}, Fe^{3+}/Fe^{2+} and Mn^{4+}/Mn^{3+} redox couples. A CoHCF@MnO2 electrode and an AC negative electrode were employed to assemble an asymmetric supercapacitor, within a working voltage of 2.0 V and delivered maximum energy density of 37.6 Wh kg^{-1} and maximum power density of 1.1 kW kg-1. Obtained results demonstrate CoHCF@MnO_2 as a desirable cathode material for future energy device.

Zhu et al. in 2020 synthesized hollow cobalt-iron Prussian blue analogue (Co_2HCFe) via coprecipitation method and studied its electrochemical performance. It was reported that Co2HCFe achieved specific capacitance of 2526 F g^{-1} at the current density of 0.5 A g^{-1}, in 3M KOH, while remaining a capacity retention rate of 90.25% after 2000 cycles. Obtained results suggest Co_2HCFe nanocubes as a promising electrode material for future energy storage devices.

Prussian blue and manganese doped Prussian blue in optical sensor:

Renren Deng et al. reported a novel design, based on a combination of lanthanide- upconversion nanoparticles and manganese dioxide nanosheets,forrapid,selective detection of glutathione in aqueous solutions and living cells. In this approach, manganese dioxide (MnO_2) nanosheets formed on the surface of nanoparticles serve as an efficient quencher for upconverted luminescence. The luminescence can be turned on by introducing glutathione that reduces MnO2 into Mn2+. The ability to monitor the glutathione concentration intracellularly may enable rational design of a convenient platform for targeted drug and gene delivery**.**

To investigate the capability of MnO_2-modified UCNPs for monitoring intracellular GSH levels in cancer cells, they incubated two types of cancer cell lines (HepG2 human hepatoblastoma and HeLa cervical carcinoma cells) with the nanoparticles and subsequently analyzed the results under an optical microscope equipped with a 980-nm laser. HepG2 cells incubated with the nanoparticles (100 μg/mL) for 3 h exhibited a strong luminescence emission, indicating a high level of GSH in hepatoblastoma cells. However, addition of buthionine sulfoximine (BSO, a glutathione synthesis inhibitor:13 100 μM) or N-methylmaleimide (NMM, a GSH scavenger:4a 500 μM) resulted in a significant decrease of the luminescence intensity. In parallel experiments, they observed a clear emission enhancement for HeLa cancer cells treated with α-lipoic acid (LPA, a GSH synthesis enhancer:14 500 μM). When NMM (500 μM) was further added to LPA-treated HeLa cells, a distinct decrease of luminescence intensity was observed. Taken together, these results strongly support the feasibility of intracellular GSH monitoring by MnO_2-modified UCNPs.

Wenwen Zhu et al. successfully demonstrated application of Prussian blue and manganese doped prussian blue in vivo experiments for effectively tumor ablation. In this work, a multifunctional nanoplatform based on Mn^{2+} doped PB (PB:Mn) nanocubes for bimodal imaging and PTT with enhanced performance was demonstrated. In this system, doping Mn2+ into PB nanocubes led to a

higher absorption at NIR and a stronger T1-MR contrast ability. Surface modification was successfully carried out on PB:Mn nanocubes, improving their stability in physiological conditions. Biomodal PA/MR imaging was conducted, revealing the effective tumor accumulation of those nanocubes after i.v. injection. Effective in vivo PTT was further demonstrated with i.v. injection of PB:Mn(15%)-PEG and NIR laser irradiation of tumors. No obvious toxicity was observed on those mice after injection of PB:Mn (15%)-PEG nanocubes. Our results successfully demonstrated that doping Mn^{2+} into PB nanocubes can achieve both enhanced T1-MR contrasting effect and improved NIR absorption, which are favorable for future imaging-guided photothermal cancer therapy.

Shunxin Tang et al. in 2023 constructed a novel many birds-with-one-stone GSH depletion-mediated in situ transformation strategy for enhanced tumor-specific PA imagingguided photoimmunotherapy. Compared with the use of engineered PB NCs directly, t-PB NCs have the advantage of being only transformed into its therapeutic form in a GSH specific manner, and thus reduce cytotoxic effects towards healthy cells. Moreover, the in situ transformed PB NCs can also support precise imaging and regional phototherapy of tumor tissues. The excellent GSH depletion ability during the transformation endows the t-PB NCs with enhanced PDT capacity in the tumor cells, which amplifies the immunogenicity of the tumor cells and promotes a powerful ICD effect. Furthermore, the GSH depletion-mediated transformation of t-PB NCs in DCs promotes the maturation and activation of this immune cell population, which further allows t-PB NC mediated photoimmunotherapy to counteract the oncogenic events in the primary tumor, but also inhibits the growth of distal metastases. Taken together, our GSH depletion mediated in situ transformation strategy not only represents a promising tool to enhance precise tumor spatial PA imaging and regional phototherapy, but also offers novel insights into the application of metal complex-nanocrystals for efficient photoimmunotherapy with immunosuppressive regulation potential.

Reference:

1. Colin D. Wessells, Sandeep V. Peddada, Robert A. Huggins and Yi Cui : Nano Lett. 2011, 11, 5421–5425

2. Yu Wang and Qianwang Chen : ACS Applied Material and Interfaces 2014 6 6196−6201

3. Feipeng Zhao, Yeyun Wang, Xiaona Xu, Yiling Liu, Rui Song, Guang Lu, and Yanguang Li : ACS App . M t I t f s 2014 6 11007−11012

4. Peixun Xiong, Guojin Zeng, Lingxing Zeng and Mingdeng Wei : Dalton Trans., 2015, 44, 16746 5. Ali Asghar Ensafi, Najmeh Ahmadi and Behzad Rezaei : RSC Adv., 2015, 5, 914

6. Yongjin Zou, Qingyong Wang, Cuili Xiang , Zhe She , Hailiang Chu , Shujun Qiu , Fen Xu, Shusheng Liu , Chengying Tang , Lixian Sun : Electrochimica Acta 188 (2016) 126–134

7. Dapeng Zhang, Junshu Zhang, Zengxu Yang, Xiaochuan Ren, Hongzhi Mao, Xianfeng Yang, Jian Yang and Yitai Qian : Chem. Commun., 2017, 53, 10556

8. Ping Nie, Jiaren Yuan, Jie Wang,, Zaiyuan Le, Guiyin Xu, Liang Hao, Gang Pang, Yuting Wu, Hui Dou, Xiaohong Yan and Xiaogang Zhang : ACS Appl. Mater. Interfaces 2017, 9, 20306−20312

9. Jian-Gan Wang, Zhiyong Zhang , Xingrui Liu , Bingqing Wei : Electrochimica Acta 235 (2017) 114–121

10. Lei Zhou, Mingyan Zhang , Yanfang Wang , Yusong Zhu , Lijun Fu, Xiang Liu, Yuping Wu, Wei Huang : Electrochimica Acta 232 (2017) 106–113

11. M. Sookhakian, W.J. Basirun , Mohd Asri Mat Teridi , M.R. Mahmoudian , Majid Azarang , Erfan Zalnezhad , G.H. Yoon , Y. Alias : Electrochimica Acta 230 (2017) 316–323

12. Xiaojuan Zhang , Ping He, Xingquan Zhang , Caixia Li, Huanhuan Liu, Shuai Wang , Faqin Dong : Electrochimica Acta 276 (2018) 92-101

13. Xiaofei Bie , Kei Kubota , Tomooki Hosaka , Kuniko Chihara , Shinichi Komaba : Journal of Power Sources 378 (2018) 322-330

14. Xiaoming Qiu, Yongchang Liu, Luning Wang, Li-Zhen Fan : Applied Surface Science 434 (2018) 1285–1292

15. Anxing Zhou, Liwei Jiang, Jinming Yue, Yuxin Tong, Qiangqiang Zhang, Zejing Lin, Binghang Liu, Chuan Wu, Liumin Suo, Yong-Sheng Hu, Hong Li, and Liquan Chen : ACS 2019 11 41356−41362

16. Samuel Wheeler, Isaac Capone, Sarah Day, Chiu Tang and Mauro Pasta : Chem. Mater. 2019 31 2619−2626

17. Yun Qiu, Ying Lin , Haibo Yang, Lei Wang : Journal of Alloys and Compounds 806 (2019) 1315-1322

18. Xiao Wang, Baoqi Wang, Yuxin Tang, Ben Bin Xu, Chu Liang, Mi Yana and Yinzhu Jiang : J. Mater. Chem. A, 2020, 8, 3222

19. Yun Tang , Wei Li , Pingyuan Feng , Min Zhou , Kangli Wang , Kai Jiang : Chemical Engineering Journal 396 (2020) 125-269

20. Yingbo Yuan, Duan Bin, Xiaoli Dong, Yonggang Wang, Congxiao Wang, and Yongyao Xia : ACS Sust b Ch . E . 2020 8 3655−3665

21. Wei Shi, Pengfei Nie, Guodong Zhu , Bin Hu , Jianmao Yang , Jianyun Liu : Chemical Engineering Journal 388 (2020) 124162

22. Xuezhen Zhu, Haisheng Tao, Maoguo Li : International Journal of Hydrogen Energy 45 (2020) 14452-14460

23. Zhaoxia Song , Wei Liu , Quan Zhou , Li Zhang , Zheng Zhang , Hongda Liu , Jiaqi Du , Junlin Chen , Guichang Liu , Zhongfu Zhao : Journal of Power Sources 465 (2020) 228266

24. Peiyao Zhu, Xiaxia Li, Hang Yao, Huan Pang : Journal of Energy Storage 31 (2020) 101544 25. Emad S. Goda , Seungho Lee , Muhammad Sohail , Kuk Ro Yoon : Journal of Energy Chemistry 50 (2020) 206-229

Chapter-4

SYNTHESIS



Synthesis method of prussian blue:

Chemicals: Analytically graded potassium hexacyanoferrate $K_4Fe(CN)_6,3H_20$;Merck Chemicals,Ferric Chloride [$FeCl_3,6H_20$;Sigma Aldrich],Manganese Nitrate [$Mn(NO_3)_2,14H_20$, Citric acid[Merck chemicals],acetone [Merck Chemicals] and di-ionized water were used in this experiment.

Synthesis Procedure of Prussian blue:Prussian blue was synthesized using a facile reflux method. This typical synthesis process can be described in following steps. First of all, a 120 mL aqueous solution of $K4[Fe(CN)_6],3H_2O$ (0.03378 g) and 0.392 g of citric acid was added dropwise to a continuously stirred Fe^{3+} aqueous solution, containing initially of $FeCl_3$, $6H_2O$ (0.0216 g) and 0.392 g of citric acid in 120 mL of water, when 60^{o}C temperature was reached. Here, citric acid basically acts as a surface-capping agent to control the size and to prevent agglomeration.After completion of adding, the mixed solution was kept stirred for 1h 30 minutes maintaining 60^{o}C temperature then let it cool normally. A bright blue solution was obtained and this was washed four times with acetone using centrifuge at 12000 rpm. for first two wash ,sample was centrifused for 20 minutes .Finally bluish product was collected and it was dried overnight in a vacuum oven at 60^{o}C.

Synthesis method of manganese doped prussian blue:

Chemicals: Analytically graded potassium hexacyanoferrate $K_4Fe(CN)_6,3H_20$;Merck Chemicals,Ferric Chloride [$FeCl_3,6H_20$;Sigma Aldrich],Manganese Nitrate [$Mn(NO_3)_2,14H_20$, Citric acid[Merck chemicals],acetone [Merck Chemicals] and di-ionized water were used in this experiment

Synthesis procedure for manganese doped prussian blue: Manganese doped prussian blue was synthesized by facile reflux method.Manganese was doped in several concentration (5%,15%,30%,50%).Here 0.001g,0.003g,0.006g,0.01g of manganese nitrate were used for 5%,15%,30% and 50% doping.120ml of acqueous solution of $k_4[Fe(CN)_6],3H_2O$ (0.03378g) and citric Acid (0.392g) was added dropwise to the 120ml solution of citric Acid (0.392g) ,ferric chloride and manganese nitrate .0.02052g,0.01836g,0.01512g and 0.0108g of ferric chloride was used for 5%,15%,30% and 50% manganese doping.The mixture was stirred for 1hr 30minutes at 60^{o}C and then let it cool for 30 minutes.A blue solutionis obtained which was washed four times with acetone using centrifuse at 12000rpm .With the increase of the concentration of doped manganese ,the colour of blued mixture faded.

Chapter-5

RESULT AND DISCUSSION



XRD Analysis:

The crystal structure of the as-synthesized prussian blue and its analogues was analyzed by X-ray diffraction (XRD), shown in Fig. . The prepared samples PB60, MnPB(5%), MnPB(15%), MnPB(30%),MnPB(50%) were scanned in 2θ mode from 10°– 80°.

The four highly intense diffraction peaks at 2θ = 17.40°, 24.84°, 35.41°, 39.76° corresponds to the (2 0 0), (2 2 0), (4 0 0) and (4 2 0) planes of PB_{60}. All reflections can be well indexed into face centered cubic $Fe_4[Fe(CN)_6]_3$,nH2O with a space group of Fm3m. The lattice constant obtained is a =b=c=10.16°and α=β=ɣ=90°, which agrees well with the existing JCPDS card no. 730687. There is no evidence in the XRD pattern for the presence of other phase or impurities in PB_{60} sample.

The XRD pattern of the sample MnPB(5%), MnPB(15%), MnPB(30%)and MnPB(50%) are shown in the Fig. 5.2 (b),(c),(d),(e) respectively. The three highly intense diffraction peaks at 2θ = 17.44°, 24.75°, 35.27 ,39.63 corresponds to the (2 0 0), (2 2 0) and (4 0 0),(4 2 0) planes of MnPB.

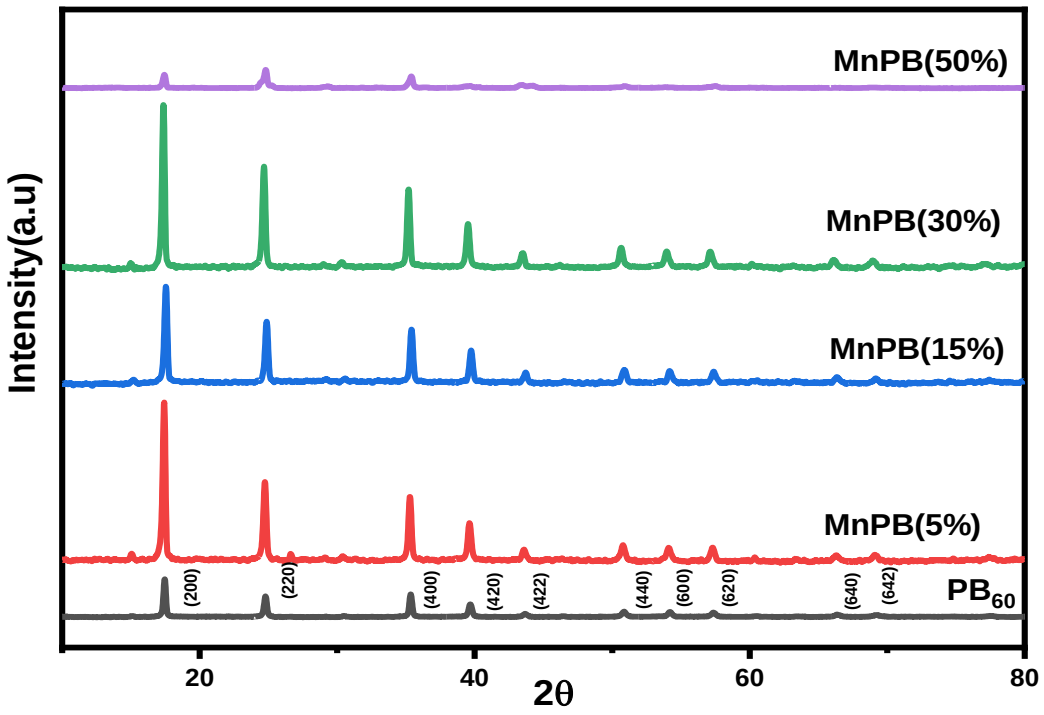
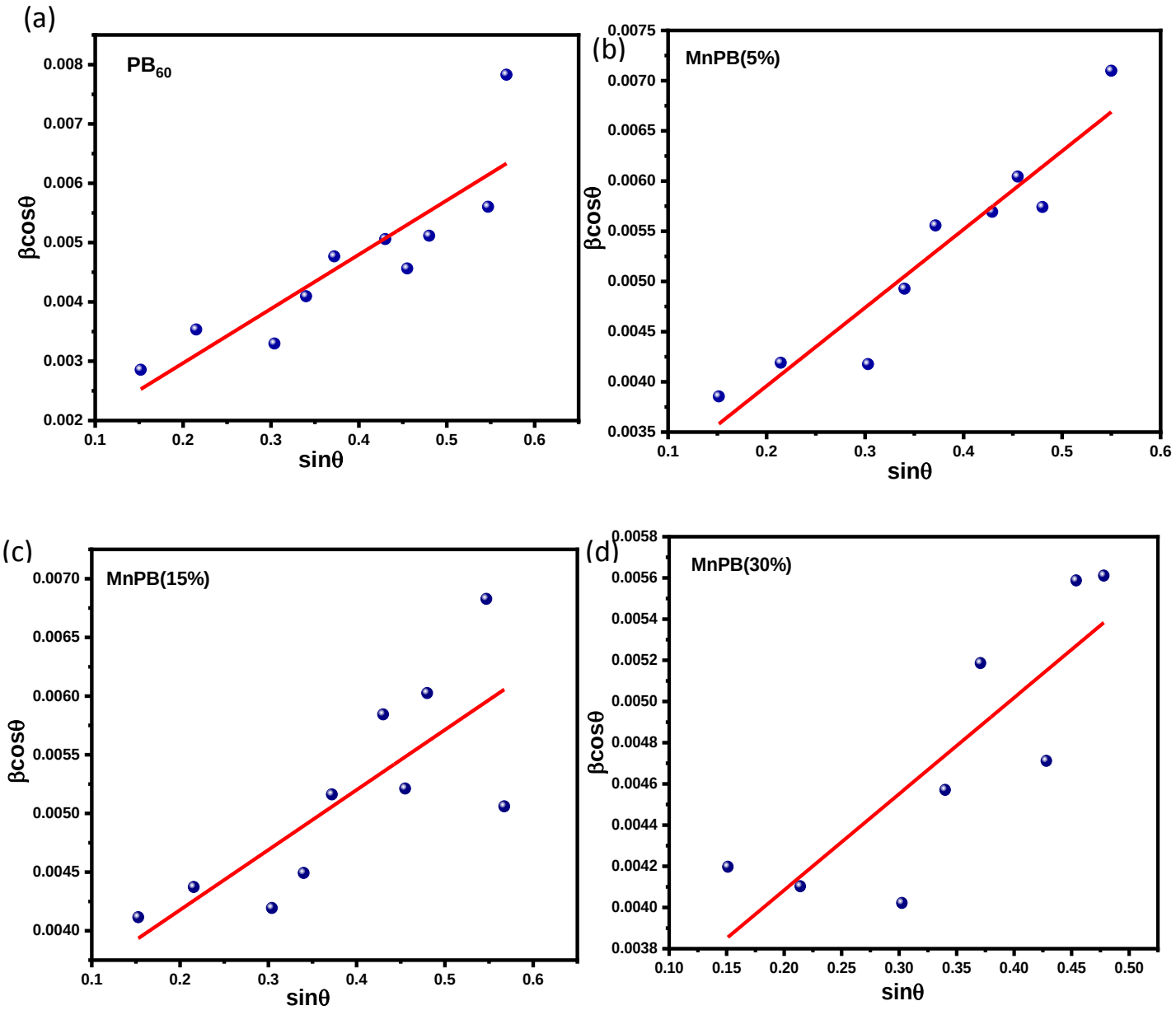


Fig.5.1-Xrd plot (a)PB_{60}(b)MnPB(5%),MnPB(15%),MnPB(30%),MnPB(50%)

The XRD pattern for each sample shows corresponding sets of peaks characteristic of Prussian blue like face centered cubic lattices. The absence of diffraction peaks corresponding to particular plane confirms the destructive interference have occurred from those planes.The particle size can be calculated from from xrd using Williamson Hall plot.

Williamson-Hall Plot:

Using Williamson Hall plot the crystalline size and tension PB_{60}, Mn:PB(5%) ,Mn:PB(15%) ,Mn:PB(30%),Mn:PB(50%) have calculated.As the percentage of manganese increases the crystalline size is also increases.



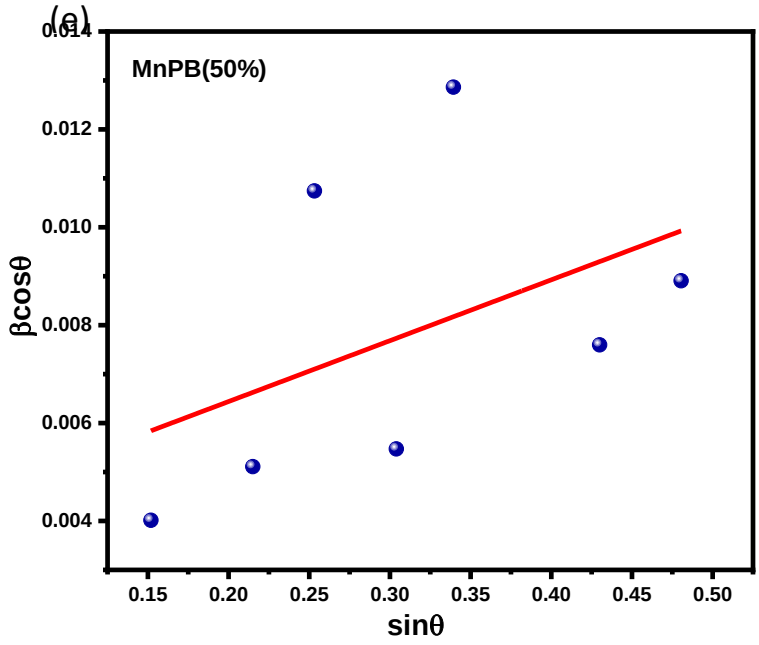


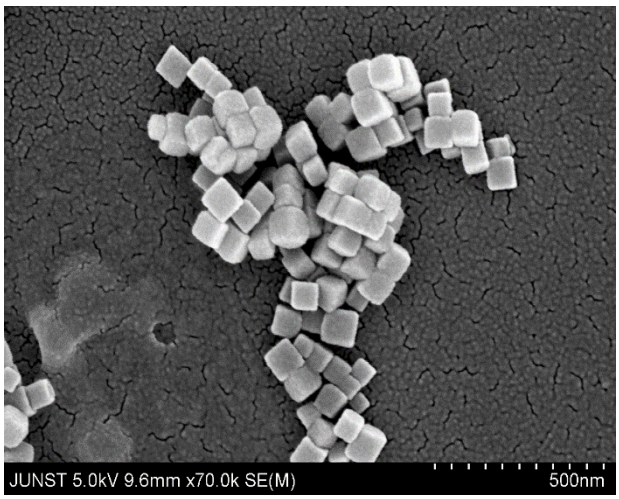
Fig5.2-Williamson Hall plot of (a)PB60(b)MnPB(5%),MnPB(15%),MnPB(30%),MnPB(50%)

	Crystalline size(nm)	**strain**
PB_{60}	15.84	4.85E-4
MnPB(5%)	18.56	4.1E-4
MnPB(15%)	28.27	3.875E-4
MnPB(30%)	31.01	3.775E-4
MnPB(50%)	43.30	3.456E-4

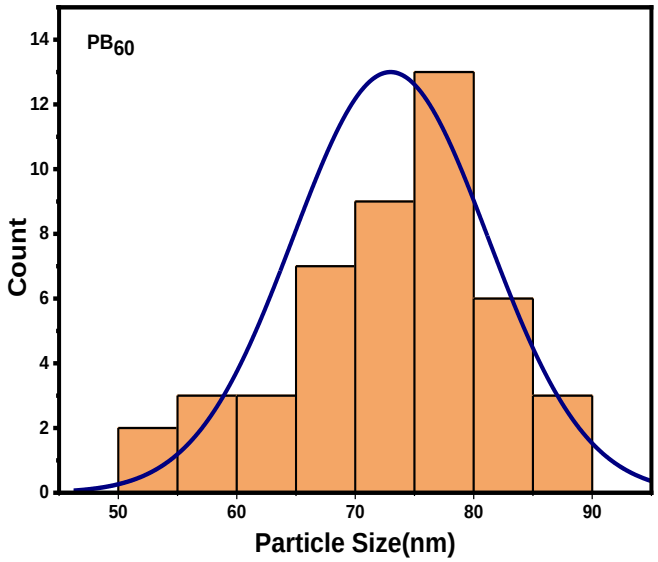
FEESEM Analysis:

The morphology and structure of PB60 and Mn doped prussian blue sample was observed by field emission scanning electron microscopy (FESEM). As shown in Fig. 4.4, the PB60nnanoparticles are all well-defined nanocubes with a uniform edge length of around 73 nm .As the percentage of Mn doping increases the average particle size also increases . The atomic radius of Mn2+ is 0.082nm where as the atomic radius of Fe3+ is 0.064nm.

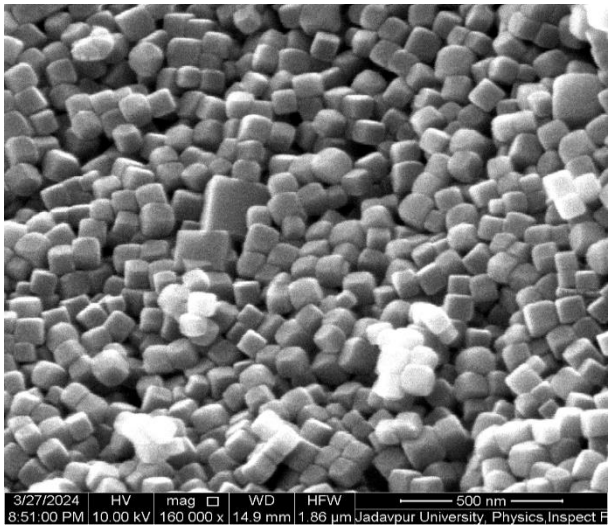
(a)



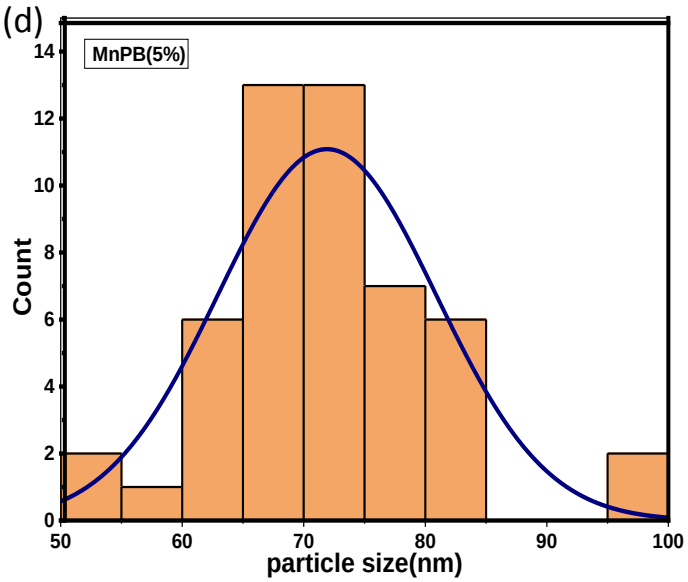
(b)



(c)



(d)



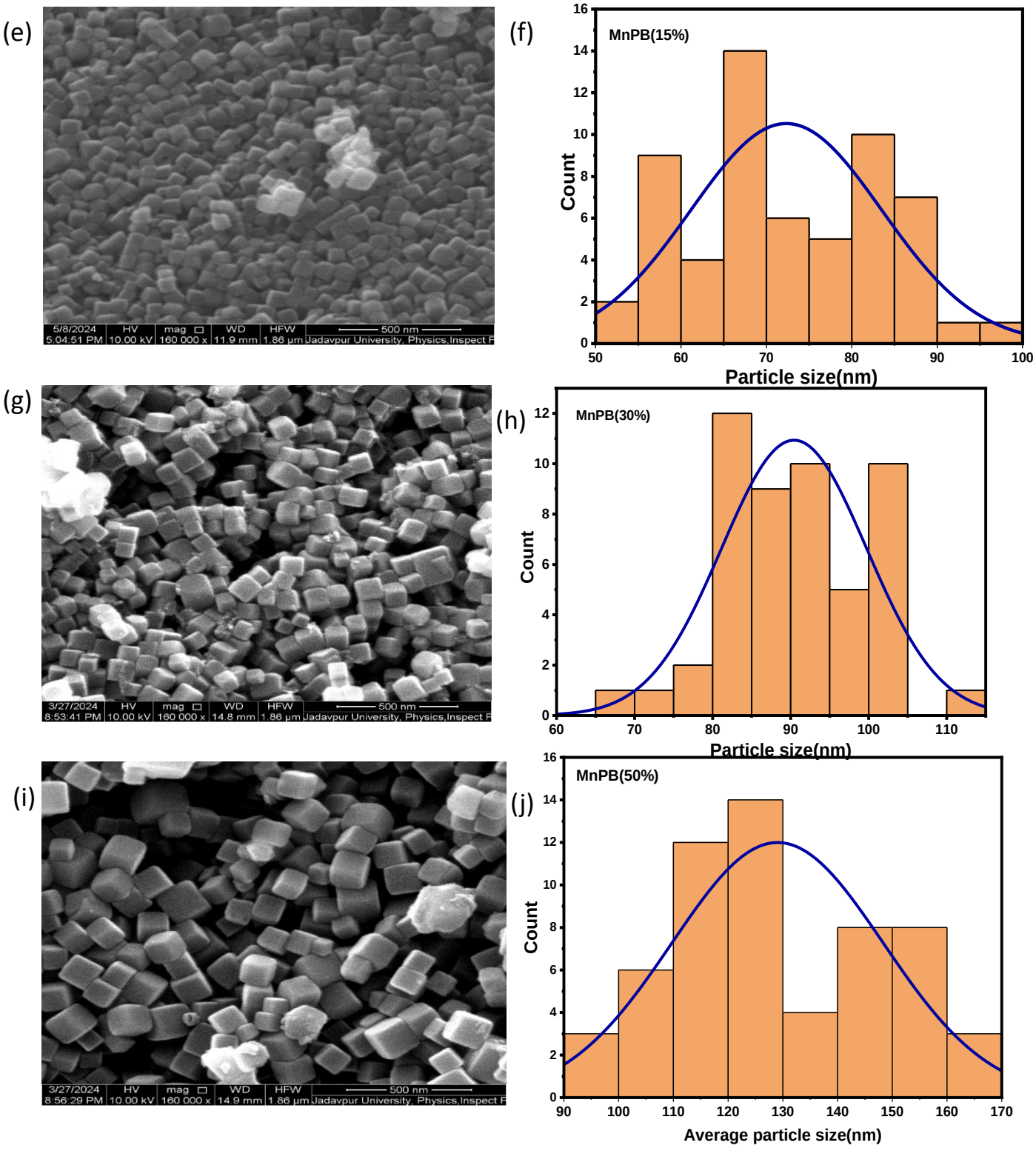


Fig.5.3-FESEM image of (a)PB60(c)MnPB(5%)(e)MnPB(15%)(g)MnPB(30%)(i)MnPB(50%) Histogram image of(b) PB60(d)MnPB(5%)(f)MnPB(15%)(h)MnPB(30%)(j)MnPB(50%)

FTIR Spectra Analysis:

The absorbtion peak at 1603 cm^{-1} and 3390cm^{-1} are assigned to bending The absorbtion peak at 1603 cm^{-1} and 3390cm^{-1} are assigned to bending and stretching vibration of –OH group of the crystal water in the framework and the band at 593 cm^{-1} should be attributed to Mn-O vibration in the MnO_6 octahedra. The strong peak at 2087 cm^{-1} is related to the stretching vibration of CN group coordinated by Fe2+ and Mn2+ stretch ligands (Fe^{II}-CN-Fe^{III}).

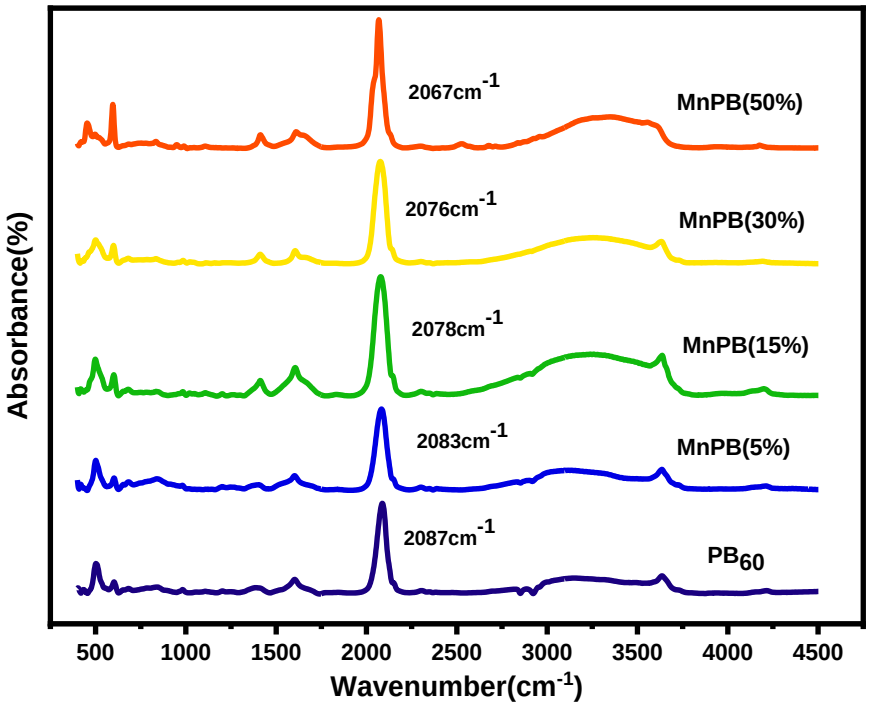


Fig- 5.4-

FTIR spectra of synthesized samples PB_{60}, MnPB(5%), MnPB(15%), MnPB(30%),MnPB(50%)

According to literature, typical vibration bands of Fe3+-NC-Fe^{2+} and Mn^{2+}-NC-Fe^{2+}, which locate at 2084 and 2063 cm^{-1} . When the manganese is doped to the prussian blue ,the stretching vibration of FeII-CN-FeIII shifts to the lower wave number,that would appear as a superimposed and broad band with two contributions of asymmetric vibrations of the bridged cyanides Mn^{2}+-NC-Fe^{2+} and Fe^{3+}-NC-Fe^{2+}.

As the increase of Mn^{2+} doping level, this IR band shifted to lower wavenumbers, further indicating that Fe^{3+} was partly replaced by Mn^{2+} (both with 5 unpaired 3d electrons) in the coordination structure matrix of PB:Mn samples.

Sample	Wavenumber(cm^{-1})
PB_{60}	2087
MnPB(5%)	2083
MnPB(15%)	2078
MnPB(30%)	2076
MnPB(50%)	2067

UV- Visible Spectra Analysis:

The optical properties of the obtained PB:Mn nanocubes were then studied. Figure 1f showed the UV−vis−NIR spectra of PB:Mn nanocubes with the same total metal ion concentrations (a sum of [Fe] + [Mn]).

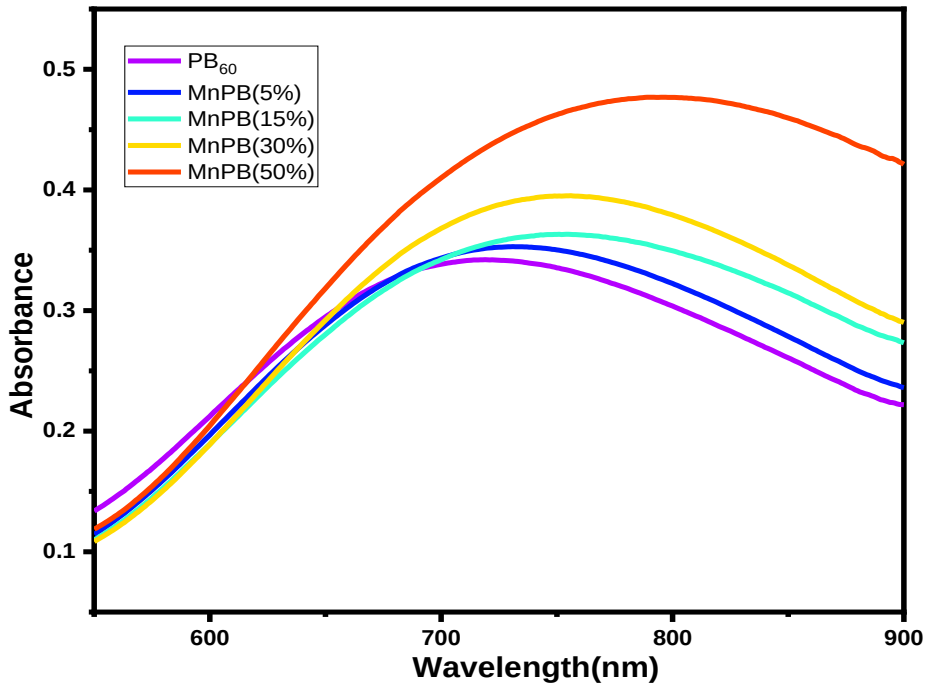


Fig- 5.5-UV Vis spectra of synthesized samples PB_{60}, MnPB(5%), MnPB(15%), MnPB(30%),MnPB(50%)

A broad absorption band from 500 to 900 nm with a strong absorption peak at 720 nm was observed for PB nanocubes, corresponding to the energy of the metal-to-metal charge transfer (MMCT) between Fe^{2+} and Fe^{3+} through the cyanide bridge.

Interestingly, after doping Mn^{2+} into PB nanocubes, it was found that the color of the solution also changed from blue to green with the increasing of Mn2+ doping ratio, and the absorbance peak was obviously red-shifted to 726, 748,759, and 790 nm for PB:Mn(5%), PB:Mn(15%), and PB:Mn(30%),PB:Mn(50%) respectively. This red-shifted absorbance in PB:Mn samples could be explained by changes in the electron density and orbital energies of the cyanide bonds due to the presence of Mn2+ in the lattice.

-

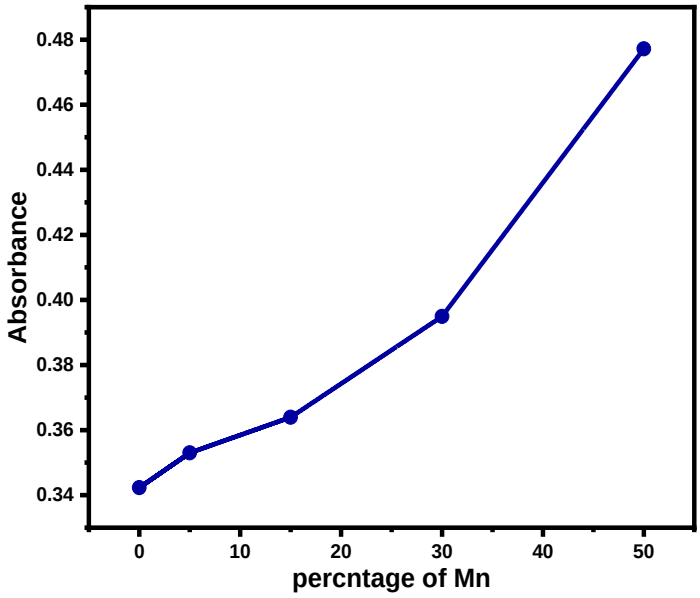


Fig5.6-Maximum absorbance of UV Vis spectra Vs Mn percentage

The absorption peak at around 216 nm is corresponds to transitional metal to cyanide transition. Obtained band gap (Eg) of PB_{60} from Tauc plot is 1.20 eV. The relation between absorption coefficient (α) and photon energy (hγ) was deduced by Tauc and is represented as,

$$(\alpha h\gamma)^{1/n} = A(h\gamma - Eg) \quad \text{.....(5.3)}$$

Where α is the absorption coefficient,

for direct allowed transitions, hγ is photon energy, E_g is band gap and A is proportionality constant. Using equation band gap of the prepared samples can be calculated

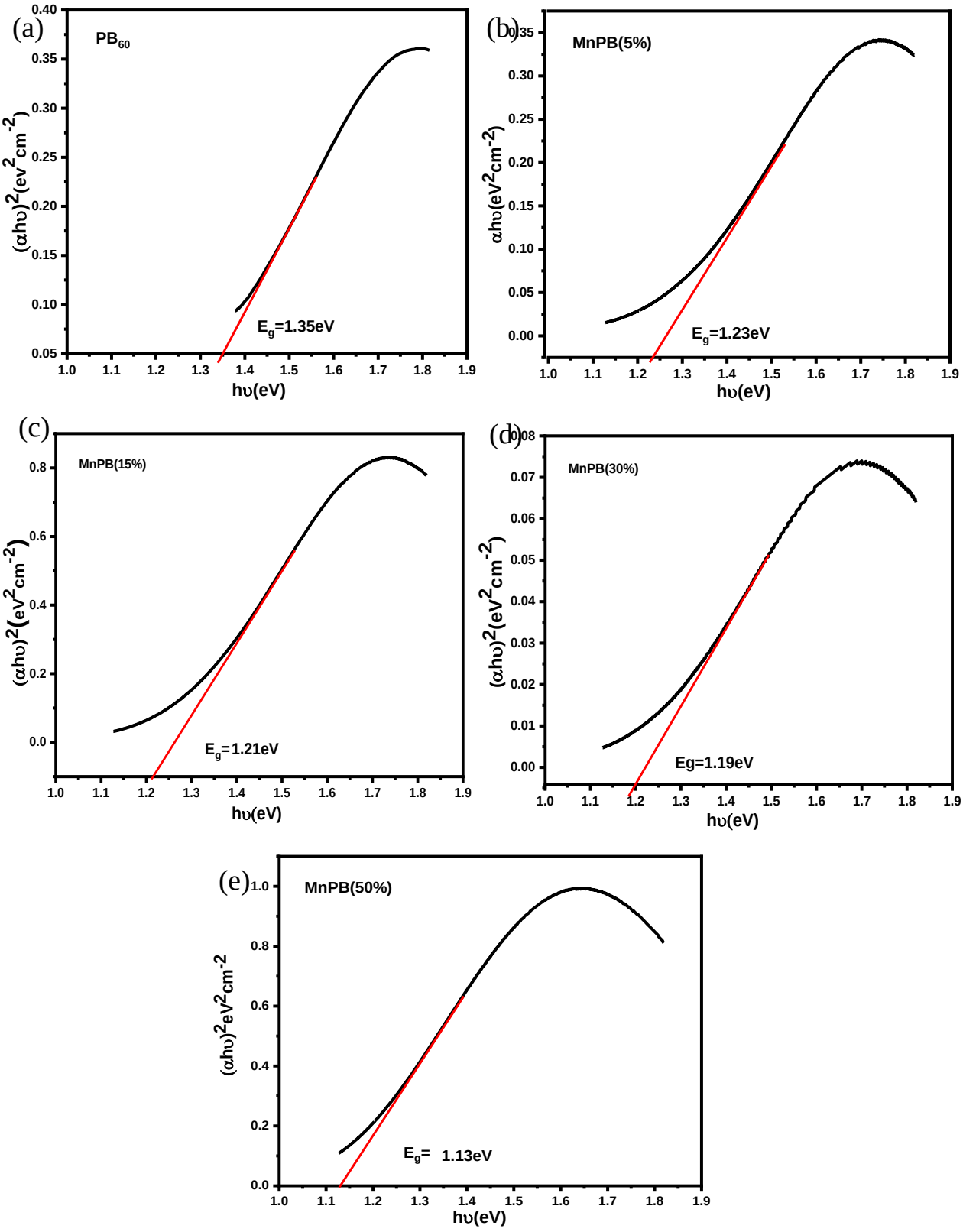


Fig- 5.7-UV band gape from Tauc plot of synthesized samples(a) PB_{60}, (b)MnPB(5%), .
(C)MnPB(15%), (d)MnPB(30%),(e)MnPB(50%)

Photoluminescence Spectroscopy:

Luminescence is one of the most important method to reveal the energy structure and surface state of semiconductor nanoparticle .Prussian blue exhibit a typical semiconductive property at room temperature .We have investigated the photoluminescence property of prussian blue and manganese doped prussian blue at room temperature .

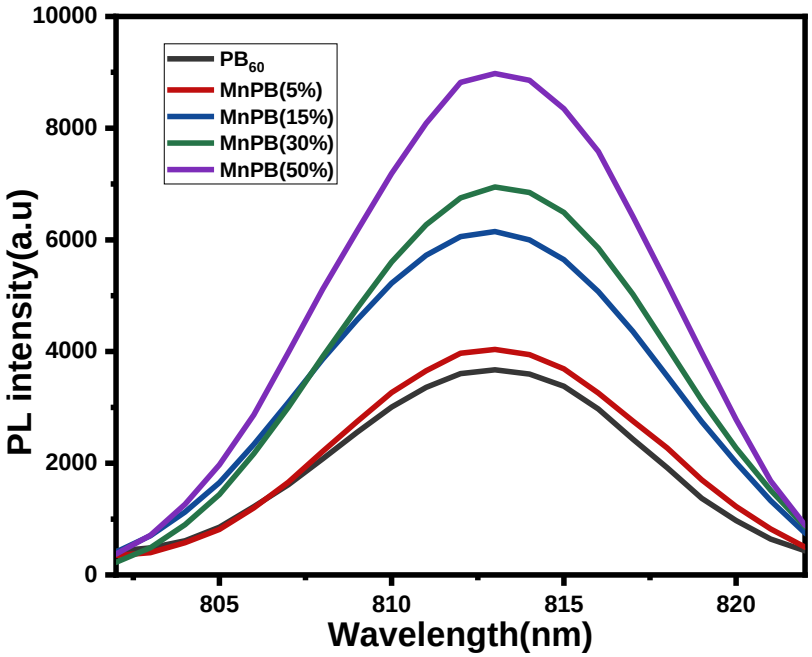


Fig- 5.8-Photoluminescenc spectra of synthesized samples PB_{60}, MnPB(5%), MnPB(15%),MnPB(30%),MnPB(50%)

PB and Mn doped prussian blue(0.02mg/ml) shows photoluminescence effect under the excitation of wavelength 406nm and emission at 813 nm.The PL emission intensity is the result of the recombination of photogenerated electrons and holes.Lower the intensity ,lower the recombination rate.As the percentage of manganese increases ,the PL intensity is also increases.More number of electrons are excited to higher energy state,leading to more radiative recombination event.

STUDY OF ELECTROCHEMICAL PROPERTY OF PB AND MN:PB

STUDY OF ELECTROCHEMICAL PROPERTIES OF PRUSSIAN BLUE AND MANGANESE DOPEDPRUSSIAN BLUE:

Electrochemical Sample Preparation: To prepare a working electrode, a gel type material was prepared by mixing the composite, graphite powder and polyvinylidene fluoride (PVDF) in a weight ratio of 65:30: 5 in 200 µL N-Methyle Pyrrolidine (NMP). The gel was then drop casted on the flat end of the Teflon coated graphite rod and dried in vacuum at temperature 60 degree for 12h. The electrochemical measurement was carried out with aqueous 0.5M Na_2SO_4 solution as electrolyte at room temperature.

The electrochemical performances of the samples were investigated by CS313 (Corrtest, China) multi-channel electrochemical workstation using Cyclic Voltammetry (CV). The cell consists of three electrode system, where platinum (Pt) electrode was used as the counter electrode, Ag /AgCl in saturated Na_2SO_4 solution was used as a reference electrode and graphite rod with a coating of active material on the open end was used as working electrode. The mass of the active electrode material in each electrode was about 0.07mg.

CV Study of as-Synthesized Samples: the CV curve PB_{60} at2, 5, 10, 20, 40, 60, 80 and 100 mV/s scan rates for cycle no. 1 respectively using aqueous 0.5M Na_2SO_4 solution as electrolyte within the potential range -0.4V to 0.7V.

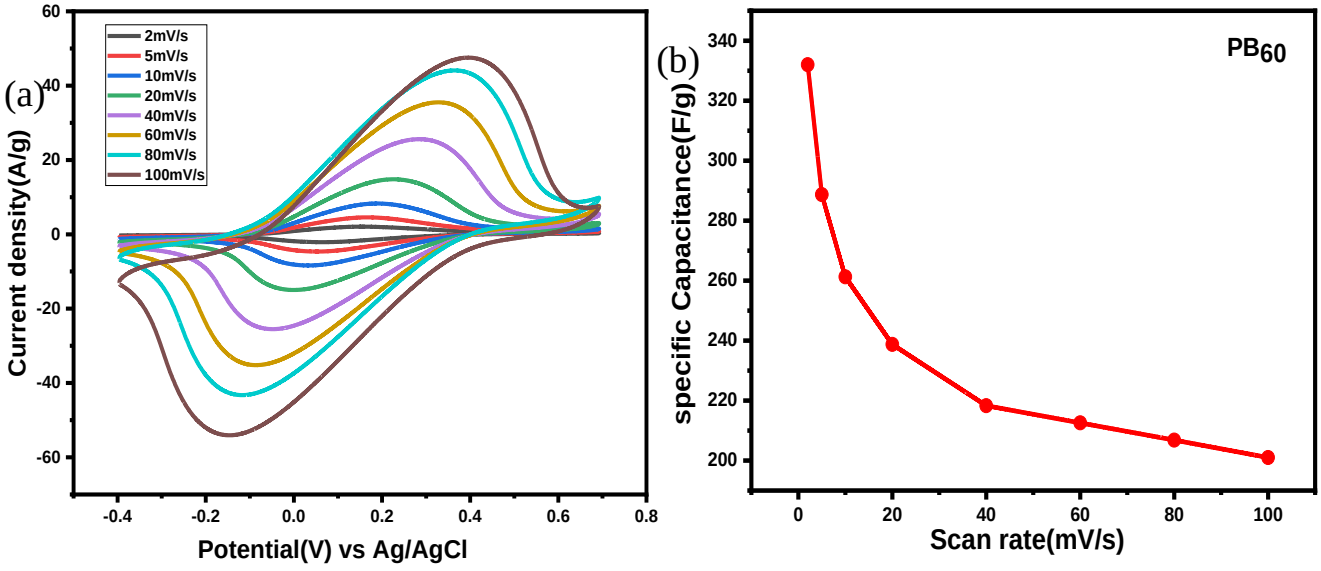


Fig5.9-(a)CV of PB_{60}(b) Specific capacitance vs scan rate of PB_{60}

The specific capacitance was calculated from the cyclic voltammetry (CV) curve using equation (5.4) where, m and k are the mass of the electroactive material and potential scan rate.

$$C_m=\frac{A}{2mk(V1-V2)} \quad (5.4)$$

The presence of separate redox peaks along with the deviation from the ideal rectangular shape of the CV curves suggests that the storage mechanism is due to the combined contribution of the non-faradaic and faradaic redox capacitances. There was no gas evolution observed at the electrode, suggesting that the sample possesses good stability in the wide potential window.PB_{60} offers the highest specific capacitance of 332F g^{-1} at 2 mV/s which is believed to be due to the intercalation or de-intercalation of Na^+ ions from the electrolyte into the $Fe_4[Fe(CN)_6]_3$ framework. Fig. 5.2 shows the variation of specific capacitance with the scan rate for PB_{60}sample. It can be seen that the specific capacitance decreases with the increasing scan rate shown in following table.

Scan rate (mV/s)	Specific Capacitance(F/g)
2	332
5	288.7
10	261.26
20	238.74
40	218.31
60	212.56
80	206.83
100	201.00

The variation of specific capacitance with scan rates depends mainly on three processes: (a) charge transfer in the electrode, (b) ion diffusion in the electrolyte and (c) adsorptions of the ions on the electrode surface. All these processes become slow at higher scan rates and thus specific capacitance decreases. However at lower scan rates, the ions get sufficient time to deeply penetrate into the inner active sites. Thus, both the inner and outer active sites of the electrode material contribute to the total specific capacitance and hence specific capacitance reaches maximum value at low scan rate and gradually decreases at higher scan rate.

At lower scan rates, the ions from Na_2SO_4 electrolyte solution need longer time to access the outer and inner surface of the electrode, which leads to the accumulation of a large number of ions at the surface

of active electrode, enhancing its charge storage capacity (enhanced capacitance). However, at higher scan rate, due to higher mobility and slow diffusion of redox electrolyte, the electrolyte ions can access only the outer surface of the electrode. As a result only a few ions get accumulated at the outer surface of the electrode, reducing the specific capacitance value. Thus the reduction of the rate performance of the capacitor at high scan rate is also related to the reduction of the electrolyte, not only related to the electrode material. The obtained results clearly indicate that the specific capacitance of a porous electrode strongly depends on applied scan rate. The specific capacitance value decreases with increase of scan rates, disclosing the specific capacitance value of an electrode material is strongly depend on the applied scan rates .

Normally, the cyclic voltammetry (CV) current of an electrode material is the combination of both Faradic adsorption/desorption i.e. redox current and non-Faradic capacitive current, which can be clearly explained according to the Power law . Thus, the total amount of charge stored in the electrode can be divided into three distinct components: the Faradic contribution from Na+ ion insertion process, the Faradic contribution from the charge transfer process at surface atoms, known as pseudocapacitance effect, and the non-Faradic double layer effect. Double layer effect and pseudocapacitive effect become prominent when the particle size of the electrode material reduces to nanoscale dimension (less than 50nm) due to high exposed surface area.

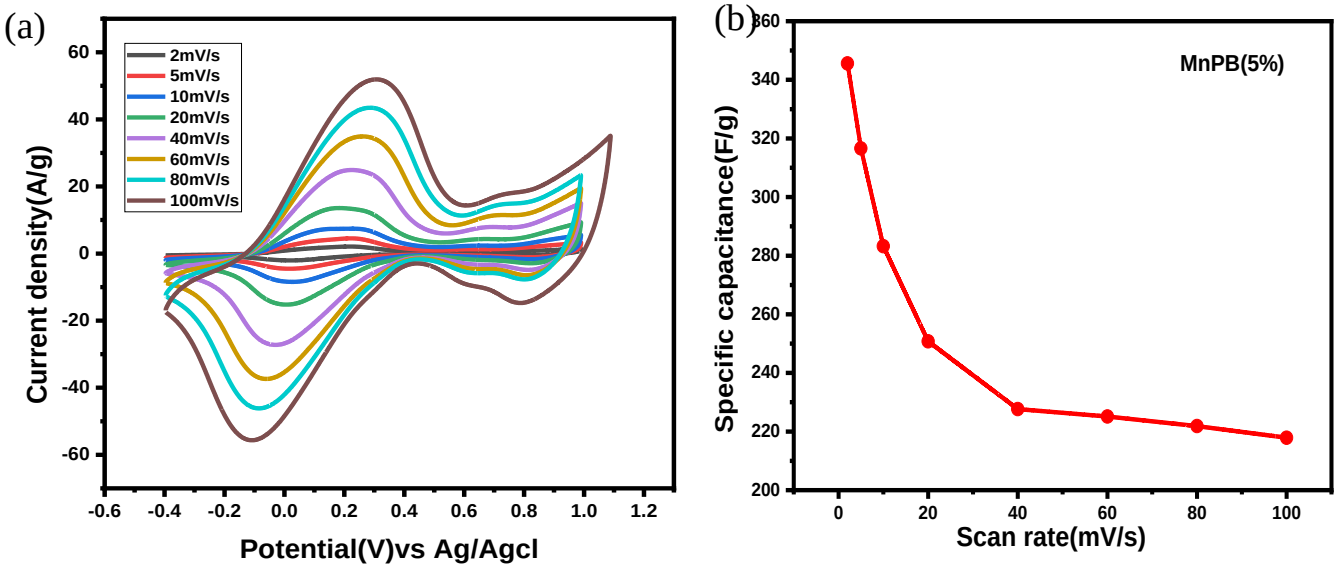


Fig5.10-(a)CV of Mn:PB(5%)(b) Specific capacitance vs scan rate of Mn:PB(5%)

MnPB(5%) offers the highest specific capacitance of 360F g^{-1} at 2 mV/s, figure(5.10) shows the variation of specific capacitance with the scan rate for PB_{60} sample. It can be seen that the specific capacitance decreases with the increasing scan rate shown in table

Scan rate(mV/s)	Specific Capacitance(F/g)
2	345.57
5	316.59
10	283.23
20	250.78
40	227.66
60	225.13
80	219.85
100	217.90

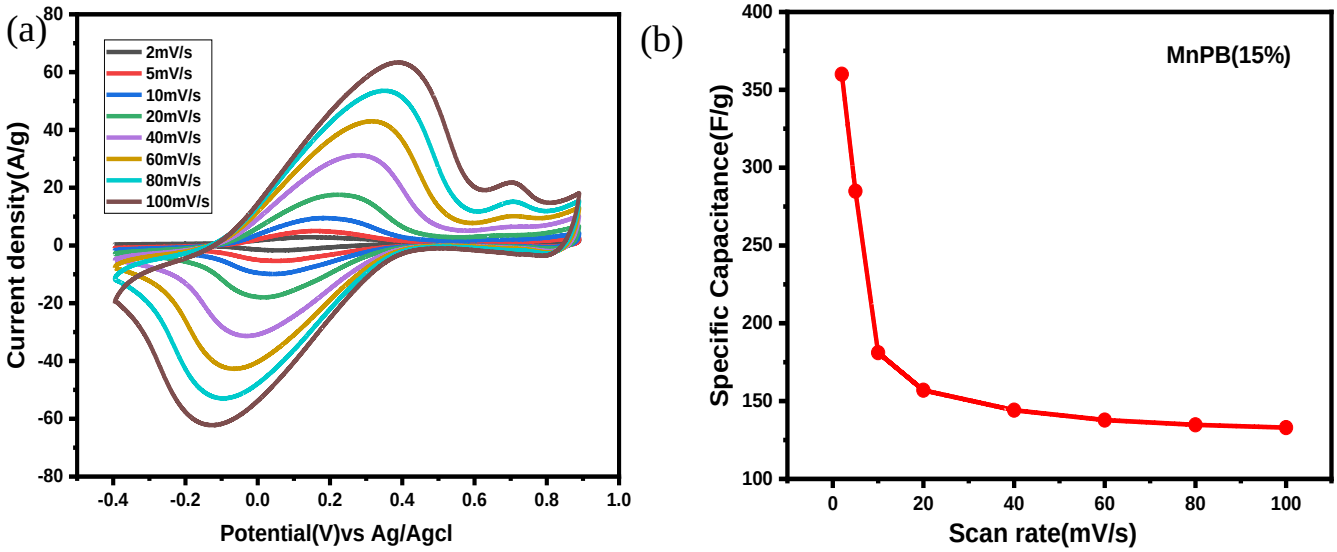


Fig5.11-(a)CV of Mn:PB(15%)(b) Specific capacitance vs scan rate of Mn:PB(15%)

MnPB1(15%) offers the highest specific capacitance of 360F g^{-1} at 2 mV/s

Scan rate(mV/s)	Specific Capacitance(F/g)
2	360
5	284.87
10	181.87
20	156.94
40	144.12
60	137.81
80	134.73
100	132.95

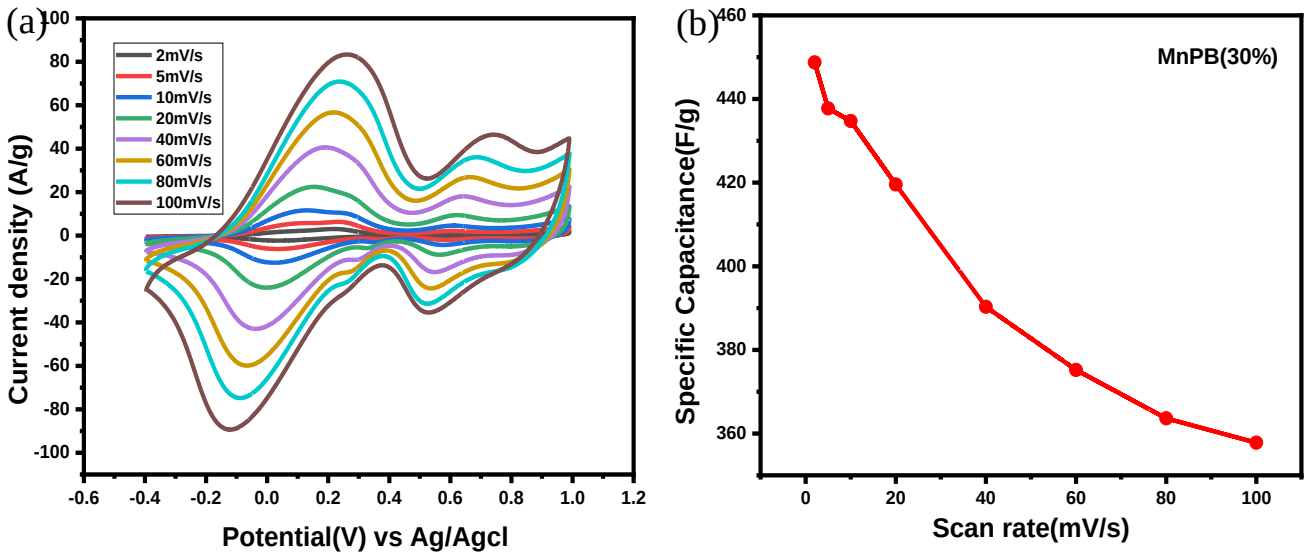


Fig5.12-(a)CV of Mn:PB(30%)(b) Specific capacitance vs scan rate of Mn:PB(30%)

MnPB(30%) offers the highest specific capacitance of 448F g^{-1} at 2 mV/s

Scan rate(mV/s)	Specific Capacitance(F/g)
2	448.75
5	437.75
10	434.75
20	419.56
40	390.30
60	375.21
80	363.63
100	357.81

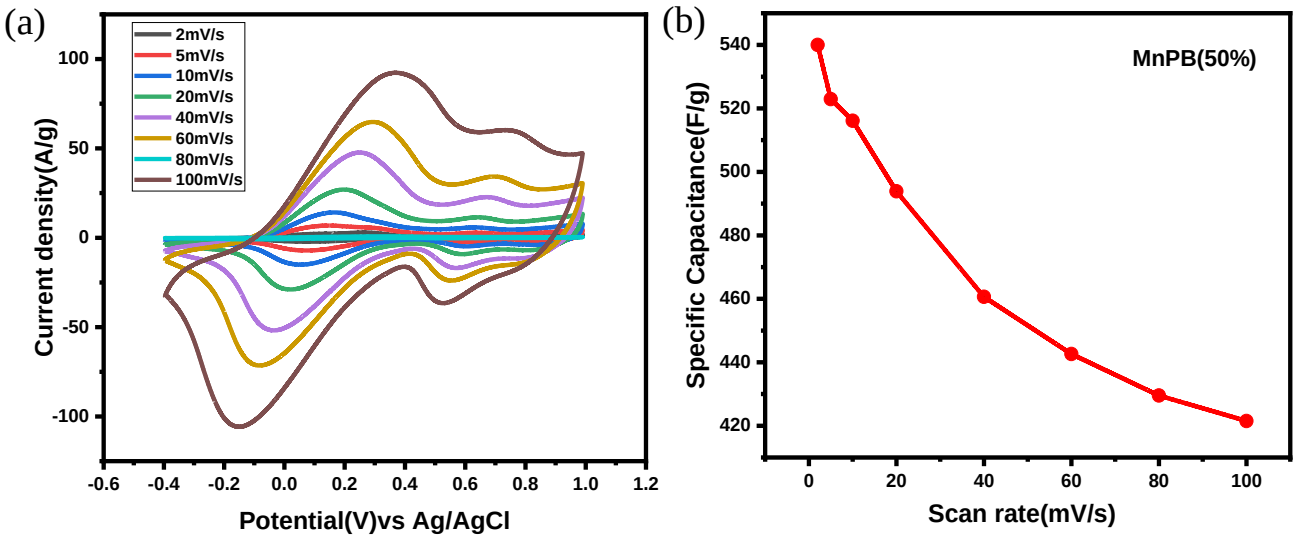


Fig5.13-(a)CV of Mn:PB(50%)(b) Specific capacitance vs scan rate of Mn:PB(50%)

MnPB(50%) offers the highest specific capacitance of 540F g^{-1} at 2 mV/s.

Scan rate (mV/s)	Specific Capacitance(F/g)
2	540.59
5	522.94

10	513.13
20	493.87
40	460..63
60	442.60
80	429.52
100	421.5

The scan rate dependence CV current of an electrode can be expressed as

$$I = av^{b} \quad (5.5)$$

where v is the scan rate (mVs^{-1}), a and b are the adjustable parameters. The 'b' value can be calculated from the slope of log (ip) vs log (v) plot at a fixed potential (V). It is well known that, for ideal diffusion controlled Faradic process of ions, the slope b=0.5 and the peak current i_p is proportional to the square root of the scan rate. Therefore, the peak current can be expressed by Eq(5.6)

$$i_p = 0.4958nFACD^{1/2}\left(\frac{\alpha nF}{RT}\right)^{1/2} \quad (5.6)$$

where n represents the electron number, F is the Faraday constant, A is the effective surface area of working electrode, C is the maximum concentration of Na+ in the lattice,αis the transfer coefficient, R is the ideal gas constant, T is the temperature in Kelvin, and D is the diffusion coefficient of Na+ ions. On the other hand, for non-Faradic capacitive current, i.e. for non-diffusion controlled process, the value of the slope b=1, and then the peak current (ip) follows the linear scan rate dependence expression Eq(5.7)

$$i=AC_md \quad (5.7)$$

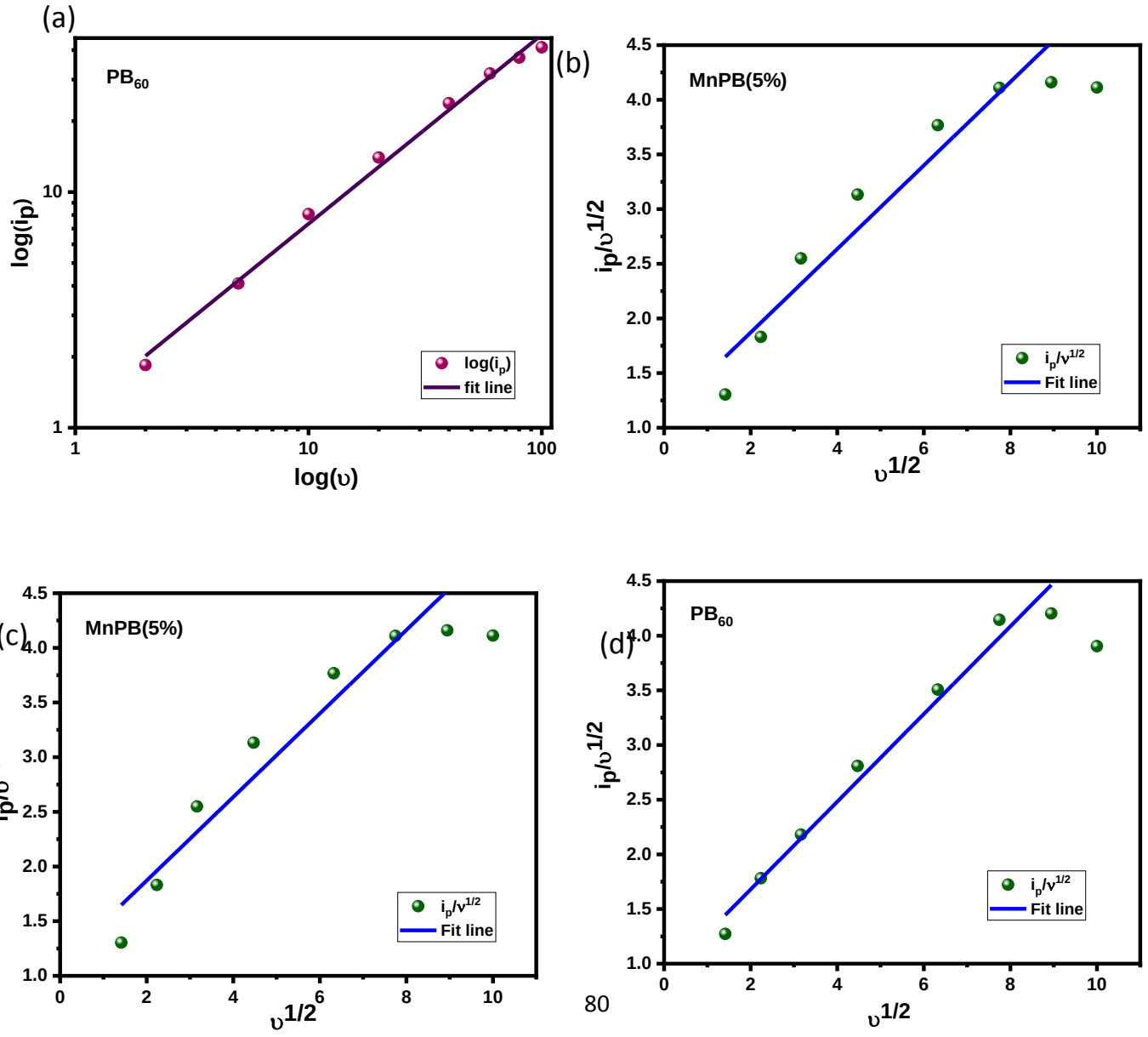
where A is the total electrode surface area, and Cd is the amount of capacitive storage per electrode surface area. Fig (5.14) shows the plot of scan rate dependence peak current log(i_p) vs log(v).

$$i_p=k_1v+k_2v^{1/2} \quad (5.8)$$

where i_p(V) presents the peak current at a given potential, k_1 and k_2 are constants, and v is the scan rate. The product k1v denotes the contribution of capacitive current (i_c) for a fixed dip(V)/dv, and $k_2v^{1/2}$ provides the diffusion controlled current (i_d) or redox reaction current for a fixed dip(V)/$dv^{1/2}$. The parameter k1 can be determined from the product AC_d of Eq. (5.7), while the parameter k_2 can be determined from the product $0.4958\ nFACD^{1/2}\left(\frac{\alpha nF}{RT}\right)^{1/2}$ of Eq. (5.6). Now, we can divide both the sides of Eq. (5.8) by $v^{1/2}$ to obtain Eq.

$$i_p(V)/\nu^{1/2}=K_1\nu^{1/2}+K_2 \quad (5.9)$$

The values of k_1 and k_2 can be determined from $i_p(V)/\nu^{1/2}$ vs $\nu^{1/2}$ plots. The slope and intercept of the linear fit correspond to the value of k_1 and k_2, which can quantitatively estimate the contributions of capacitive current (i_c) and diffusion current (i_d) at a fixed potential.



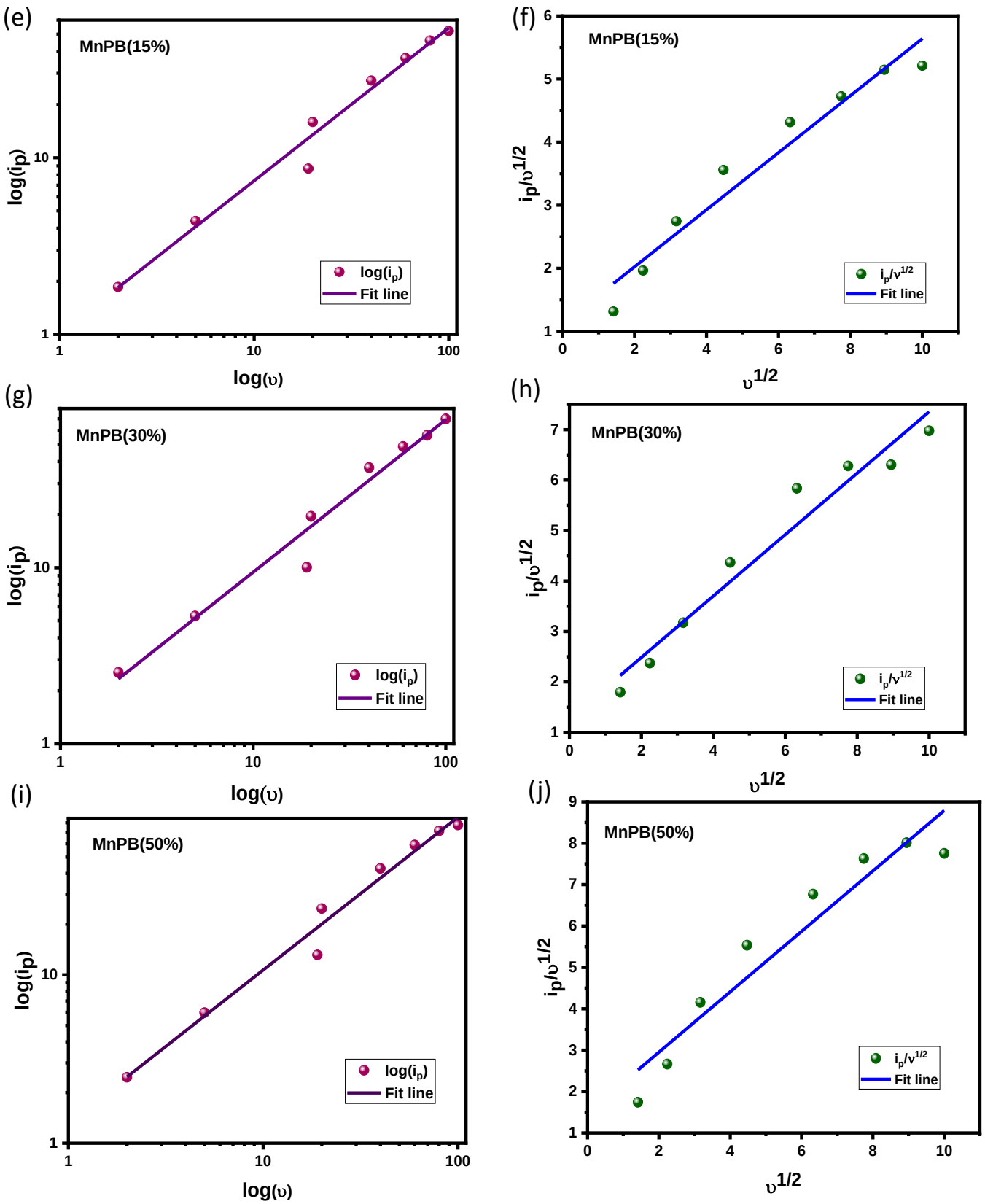


Fig5.14- log(i_p) vs log(v) plot of(a)PB_{60}(c)MnPB(5%)(e)MnPB(15%)(g)MnPB(30%)(i)MnPB(50%)

$i_p(V)/\nu^{1/2}$ vs $\nu^{1/2}$plot of (b)PB_{60}(d)MnPB(5%)(f)MnPB(15%)(h)MnPB(30%)(j)MnPB(50%)

Using equation $i = av^b$

Electrode material	b value
PB60	0.74196
Mn:PB(5%)	0.78192
Mn:PB(15%)	0.72113
Mn:PB(30%)	0.7611
Mn:PB(50%)	0.8232

The bes tlinear fitof the data to an apparent power law gives the b value of in between 0.5 and 1 (the maximum peak current has been considered), which can apparently be ascribed to a mixed process involving both the insertion of Na+ ions within the bulk of PB_{60} and Mn:PB nanoparticles, and the capacitive storage of Na^+ ions at the outer surface of the electrode.

From equation

$$i_p = k_1 v + k_2 v^{1/2}$$

Electrode material	K_1	K_2
PB60	0.38196	1.10765
Mn:PB(5%)	0.4009	0.87812
Mn:PB(15%)	0.4588	1.121
Mn:PB(30%)	0.60857	1.26919
Mn:PB(50%)	0.72907	1.49135

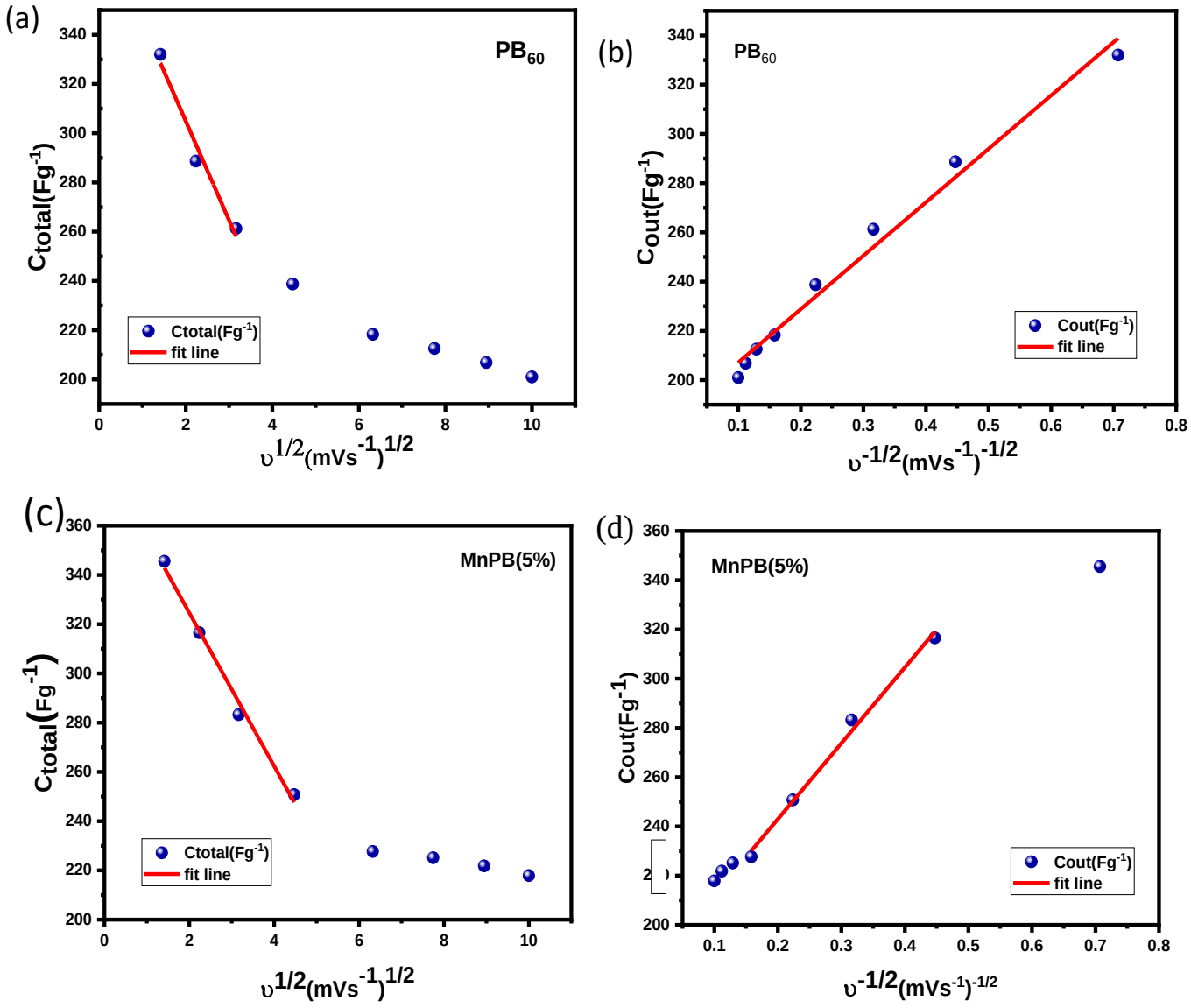
it can be proposed that the charge stored in the electrode is mainly contributed by the Faradic adsorption/desorption through redox charge transfer process, rather than capacitive mechanism, as has been well demonstrated by the “b” value from the CV curves using Power law

The charge storage mechanism of PB_{60} and manganese doped prussian blue sample is further understood by the method suggested by Trasatti. According to this model, the amount of charge stored is due to the combined effect of both double layer and pseudocapacitive mechanism and the specific capacitance may be written in the form

$C_{total} = C_{in} + C_{out}$ (5.10)

Where, C_{in} is the capacitance due to pseudocapacitive reaction (inner surface) and Cout is the capacitance due to EDLC mechanism (outer surface). At the diffusion of electrolyte ions inside the

pores are limited due to time constraints and the charge storage depends only on the interaction of the outer surface (C_{out}) which are in direct contact of the electrolyte. But the inner contribution (C_{in}) involves the effect of various defects such as voids, grain boundaries, pores, cracks etc. The total charge storage includes both outer and inner contributions and can be evaluated by extrapolating the specific capacitance versus $v^{1/2}$ curves assuming v tends to zero. At higher scan rates, the experimental data deviates from linear behavior due to the ohmic drop and irreversible redox reaction. Thus, we have fitted the data only at lower scan rates and extrapolating the fitted curve we get the maximum possible specific capacitance(C_{Total}). .Subsequently,a linear dependence of C_{Total} vs $v^{-1/2}$ plot gives the specific capacitance contribution from outer electrode surface at higher scan rates ($v \rightarrow \infty$) and it may be due to controlled ions diffusion into the electrode pores. The estimated total specific capacitance (C_T) and outer surface specific capacitance (C_{out}).



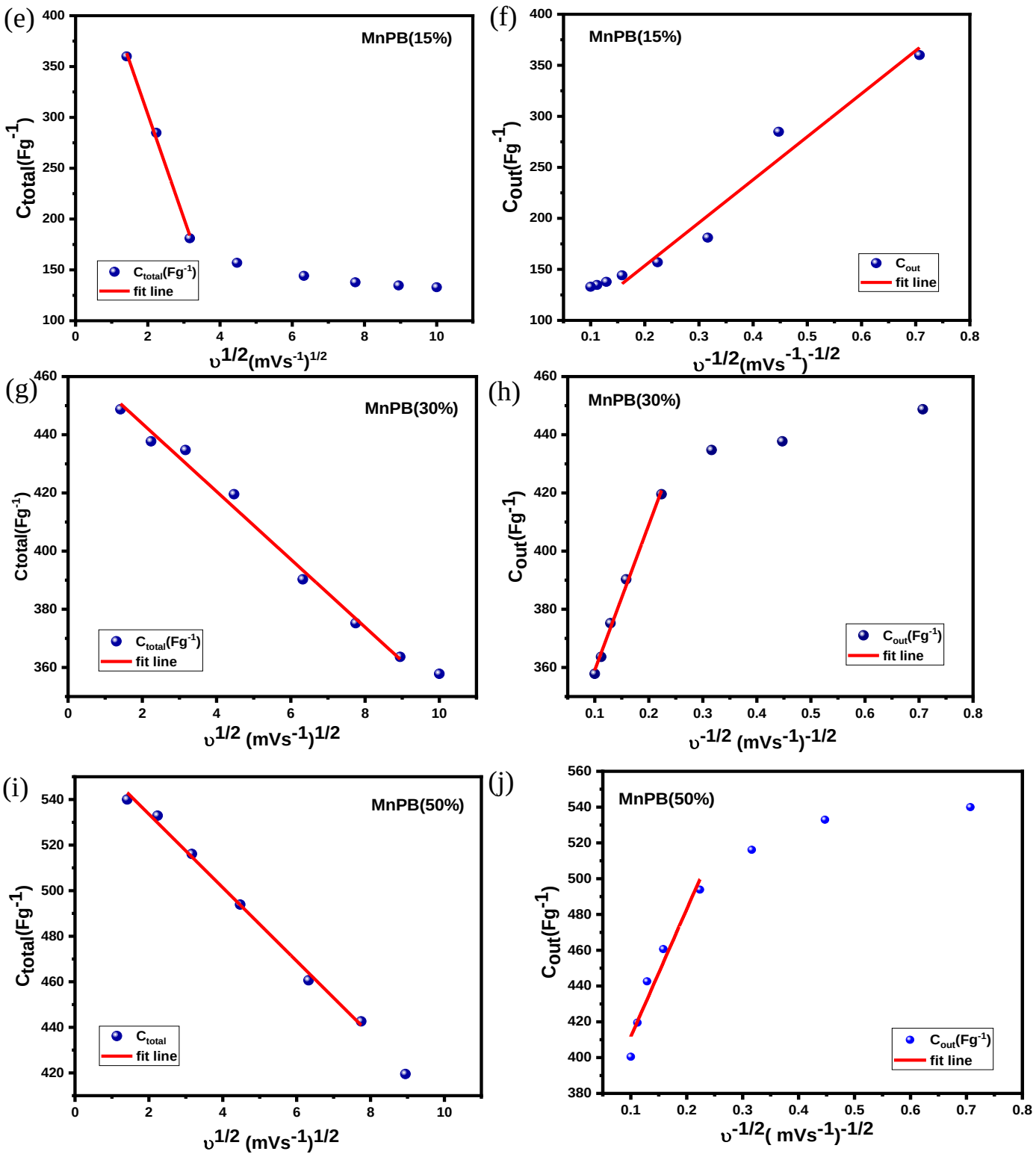


Fig5.15- C_{Total} vs $v^{1/2}$ plot of(a)PB_{60}(c)MnPB(5%)(e)MnPB(15%)(g)MnPB(30%)(i)MnPB(50%)

C_{out} vs $v^{-1/2}$ plot of (b)PB_{60}(d)MnPB(5%)(f)MnPB(15%)(h)MnPB(30%)(j)MnPB(50%)

The estimated total specific capacitance (C_T) and outer surface specific capacitance (C_{out}) for the prussian blue nanoparticles electrode were385.36 Fg−1 and 185.44Fg^{-1}, respectively. The value of specific capacitance contributed by the inner surface (C_{in}) of the electrode was estimated by subtracting C_{out} from CT, obtaining 200Fg^{-1}.For Mn:PB(5%) C_{total} and C_{out} were 398.4F/g and 180 F/g respectively.Cin is 218F/g.The percentage of C_{in} is greater than prussian blue.C total and Cout for Mn:PB(15%) are 438.20F/g and 69f/g respectively.Cin is 370F/g .The percentage of Cin is 84.44%.So the capacitance is mostly pseudocapacitance in nature. For Mn:PB(30%) C_{total} and C_{out} were 470F/g and 300 F/g respectively.C_{in} is 270F/g. C total and Cout for Mn:PB(50%) are 560.6 and 390.19F/g respectively. . Hence, it is confirmed that large number of active sites are present in the inner surface of the Mn:PB electrode, and the major fraction of the specific capacitance value comes from the contribution of inner sites rather than the outer surface of the electrode, i.e., the charge storage mechanism is strongly controlled by the Faradic adsorption/ desorption process. For Mn:PB (15%) pseudocapacitance is maximum.For higher doping concentration pseudocapacitance percentage decreases.

Galvanostatic charge discharge study on synthesized sample:

Galvanostatic charge discharge (GCD) curve is one of the most reliable technique to determine capacitance energy density, power density, equivalent series resistance and cycle life of a supercapacitor.It can be seen that the charge discharge profile deviate from typical linear variation of voltage with time. It is mainly due to the IR drop that increases with the increase of current rate.

The specific capacitance can be calculated from the GCD profile using equation

$$C\text{m}=\frac{i}{m\frac{dv}{dt}} \qquad (5.11)$$

where (i) is the applied current density (A g^{-1}) and dv/dt is the average slope of the discharge curve.

The electrochemical performance of the electrode made of prussian blue and manganese doped prussian blue nanoparticles was further studied by galvanostatic charge discharge (GCD) process at different current densities (1.428, 2.857, 4.286, 5.714 and 7.143Ag^{-1}). The GCD plots for the potential range −0.4 to+0.9V with respect to Ag/AgCl reference electrode, which is consistent with the potential range of CV measurement, i.e. same as CV potential window.

The GCD plots indicate the pseudocapacitor type behavior with very low current densities at the potential corresponding to the Faradic reactions of prussian blue and manganese doped prussian blue.At the beginning of discharge a sudden potential drop is found,which indicates the internal resistance is low within Na_2SO_4 electrolyte solution, as well as low contact resistance at the interface of current collector and electrolyte solution. The GCD plots indicate the pseudocapacitor type behavior with very low current densities at the potential corresponding to the Faradic reactions.

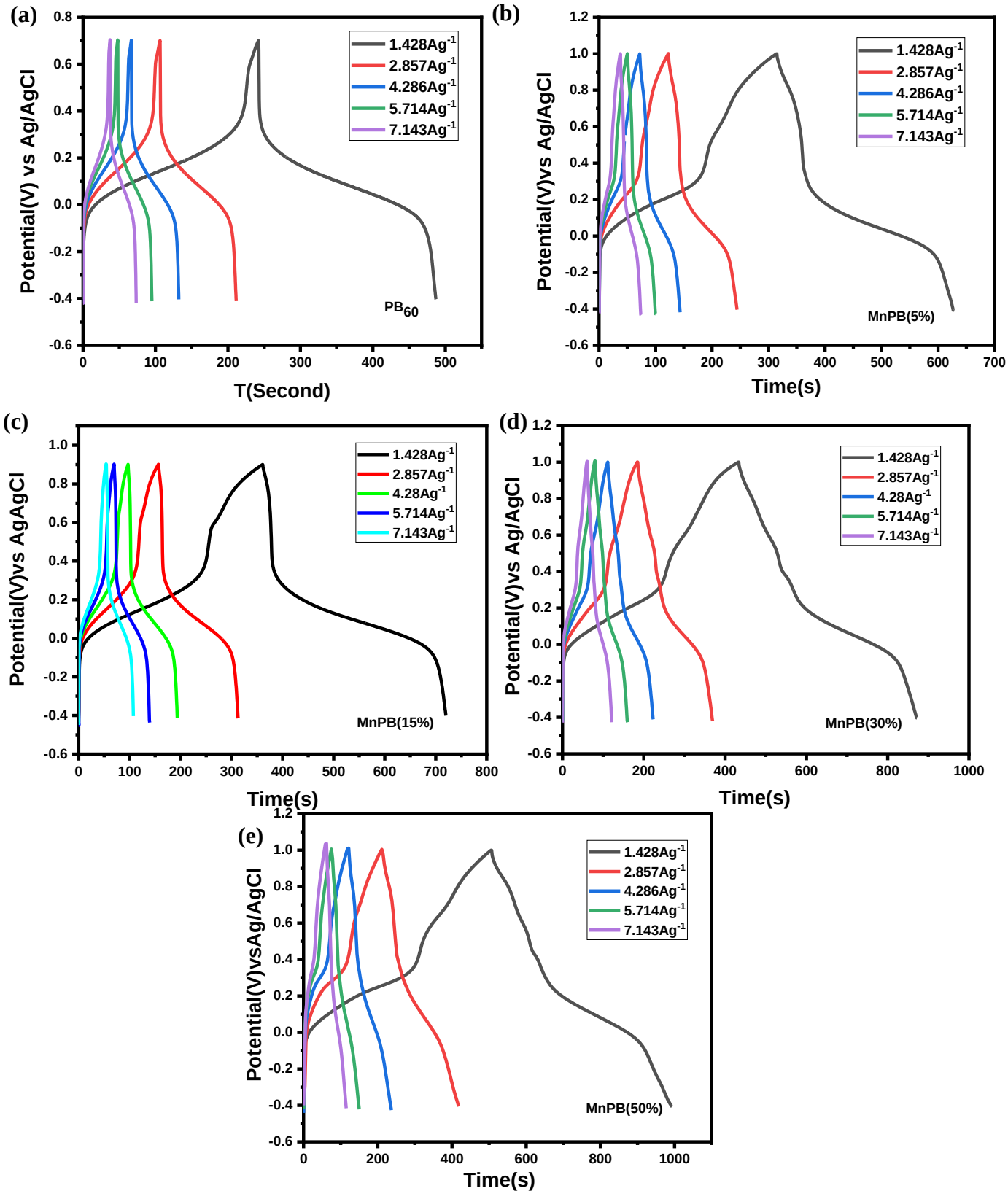


Fig5.16- galvanostatic charge discharge plot of .
(a)PB_{60}(c)MnPB(5%)(e)MnPB(15%)(g)MnPB(30%)(i)MnPB(50%)

Current density(A/g)	Specific capacitance for PB_{60} (Fg^{-1})	Specific capacitance for MnPB(5%) (Fg^{-1})	Specific capacitance for MnPB(15%) (Fg^{-1})	Specific capacitance for MnPB(30%) (Fg^{-1})	Specific capacitance for MnPB(50%) (Fg^{-1})
1.428	317.56	321.15	366.71	452.04	513.3
2.857	274.36	248.10	317.73	380.3	484.93
4.286	253.75	218.87	298.16	341.15	441.8
5.714	243.53	203.36	283	321.26	401.6
7.143	232.46	183.37	269.4	311.5	385.7

The GCD plots shows clearly that prussian blue and manganese doped prussian blue has pseudocapacitance behavior .For 15% doped percentage ,pseudocapacitance is 84.44% of total capacitance. The higher value of inner contribution to the specific capacitance suggests that the redox reaction plays a dominating role in storing the charges.At higher scan rate Ohmic drop becomes significant which introduces nonlinearity in the respective plots.

The overall electrochemical performance of the PB_{60} and Mn:PB electrode actually suggests its usability as a superior and ecofriendly asymmetric supercapacitor device in future.

Reference:

1. Yueqiang Lin, Longhai Zhang, Ya Xiong, Tong Wei, and Zhuangjun Fan : Energy Environ. Mater. 2020, 3, 323–345

2. Emad S. Goda , Seungho Lee , Muhammad Sohail , Kuk Ro Yoon : Journal of Energy Chemistry 50 (2020) 206-229

3. Colin D. Wessells, Sandeep V. Peddada, Robert A. Huggins and Yi Cui : Nano Lett. 2011, 11, 5421–5425

4. Yun Tang , Wei Li , Pingyuan Feng , Min Zhou , Kangli Wang , Kai Jiang : Chemical Engineering Journal 396 (2020) 125-269

5. Atanu Roy, Apurba Ray, Priyabrata Sadhukhan, Samik Saha, Sachindranath Das : Materials Research Bulletin 107 (2018) 379-390

6. Feipeng Zhao, Yeyun Wang, Xiaona Xu, Yiling Liu, Rui Song, Guang Lu, and Yanguang Li : ACS App . M t . I t f s 2014 6 11007−11012

7. Dezhi Yang, Jing Xu, Xiao-Zhen Liao, Yu-Shi He, Haimei Liu and Zi-Feng Ma : Chem. Commun., 2014, 50, 13377

8. Peixun Xiong, Guojin Zeng, Lingxing Zeng and Mingdeng Wei : Dalton Trans., 2015, 44, 16746 9. Dapeng Zhang, Junshu Zhang, Zengxu Yang, Xiaochuan Ren, Hongzhi Mao, Xianfeng Yang, Jian Yang and Yitai Qian : Chem. Commun., 2017, 53, 10556

10. Ping Nie, Jiaren Yuan, Jie Wang,, Zaiyuan Le, Guiyin Xu, Liang Hao, Gang Pang, Yuting Wu, Hui Dou, Xiaohong Yan and Xiaogang Zhang : ACS Appl. Mater. Interfaces 2017, 9, 20306−20312 11. Xiaojuan Zhang , Ping He, Xingquan Zhang , Caixia Li, Huanhuan Liu, Shuai Wang , Faqin Dong : Electrochimica Acta 276 (2018) 92-101

12. Xiaofei Bie , Kei Kubota , Tomooki Hosaka , Kuniko Chihara , Shinichi Komaba : Journal of Power Sources 378 (2018) 322-330

13. Xiao Wang, Baoqi Wang, Yuxin Tang, Ben Bin Xu, Chu Liang, Mi Yana and Yinzhu Jiang : J. Mater. Chem. A, 2020, 8, 3222

14. Anxing Zhou, Liwei Jiang, Jinming Yue, Yuxin Tong, Qiangqiang Zhang, Zejing Lin, Binghang Liu, Chuan Wu, Liumin Suo, Yong-Sheng Hu, Hong Li, and Liquan Chen : ACS App . M t . I t f s 2019 11 41356−41362

15. Samuel Wheeler, Isaac Capone, Sarah Day, Chiu Tang and Mauro Pasta : Chem. Mater. 2019 31 2619−2626

16. Yun Tang , Wei Li , Pingyuan Feng , Min Zhou , Kangli Wang , Kai Jiang : Chemical Engineering Journal 396 (2020) 125-269

CONCLUSIONS & FUTURE SCOPES

Conclusions :

In the present work, the Prussian blue (PB60) and manganese doped prussian blue (5%,15%,30%,50%) materials have been synthesized using low temperature facile reflux procedure. The synthesized samples were characterized by X-ray diffraction (XRD), Field emission scanning electron microscopy (FESEM), Fourier transform infrared spectroscopy (FTIR), UV-Visible and PL spectroscopy.

The structural study was conducted for XRD in a 2θ mode from 10º to 80º. The XRD pattern for each sample showed corresponding sets of peaks characteristic of Prussian blue like face centered cubic lattices. The crystal morphology of the prepared PB_{60} and Mn:PB sample were observed using FESEM. Pb_{60} ,Mn:PB(5%),Mn:PB(15%),Mn:PB(30%),MnPB(50%)nanoparticles are all well-defined nanocubes with a uniform edge length of around 70,72,79,91 and 130 nm are interconnected to form a continuous porous network. The framework crystalline structure constructed with cyanide ligands was verified using FTIR analysis. Ultraviolet−visible spectral study was recorded to understand the electronic structure and the optical band gap of the prepared samples.

For the application purpose we choose the electrochemical analysis of those prepared samples. The electrochemical measurement cyclic voltammetry (CV) and galvanostatic charge discharge of PB and Mn:PB sample was performed. Mn:PB(15%) delivered the highest specific capacitance of 438 F g^{-1} at 2 mV s^{-1} in aqueous 5M KOH electrolyte. Outer and inner capacitance of 69 F g-1 and 370 F g^{-1} respectively, was achieved from CV analysis. The higher value of inner contribution to the specific capacitance suggested that the redox reaction play a dominating role in storing the charges. From this, we can conclude that Mn doped prussian blue can be an excellent candidate for future energy storage devices.

Future Scopes :

a. By varying synthesis condition of Prussian blue and the doping percentage of its analogous, we can perform Rietveld refinement of the prepared samples to obtain its structural information and to study their electrochemical properties in non-aqueous electrolyte.

b. By incorporating conducting polymer (PANI, polypyrrole) and siloxene material with Prussian blue and its analogues, we can design asymmetric supercapacitor to investigate further improvements on its electrochemical performance.

c. Synthesis of Prussian blue analogues and delafossite oxide based composite material to study its electrochemical properties with the variation of electrolyte (aqueous, organic, ILs etc.). d. From all of the above electrochemical studies we can further calculate kinetic parameters related to charge transfer reaction using DFT (Density functional theory).

EXPLORATION OF PRUSSIAN BLUE AND MN DOPED PRUSSIAN BLUE IN OPTICAL SENSOR TO DETECT GLUTHATHOIN

Glutathione (GSH) is a kind of vital endogenous antioxygen as well as the most abundant intracell sulfhydryl product in biological systems. It has crucial and ubiquitous influence on numerous crucial biological activities, including defense against toxins and free radicals, keeping redox homeostasis, and regulating cell proliferation.1,2 Because of the redox feature of GSH, it can be simply reacted to form the dipolymer of GSH, glutathione disulfide (GSSG), as the response of oxidative forces within the human body. The concentration of GSH (or GSH/GSSG ratio) in human blood is related with some diseases, such as aging, Alzheimer's disease, cancers, and so forth, and further reflect the health level in some extent.4 Therefore, efficient detection of GSH in living biosystems is favorable to grasp GSH-related pathophysiological events.5 Various methods including high-performance liquid chromatography,6 electrochemistry, colorimetry, photoelectrochemistry,9surface-enhanced Raman spectroscopy, enzyme-linked immunosorbent, as well as fluorescent assays have exerted prospective assays for the detection of GSH.Among them, the fluorescent detection technique would be recommendable for the successful detection of GSH and intracellular imaging, owing to its nondestructive characteristics, realtime monitoring, rapid response, high selectivity and sensitivity, and the possibility of detection in a living system.

Tumor imaging and photoimmunotherapy hold great promise for precise and efficient tumor treatment. However, a tumor microenvironment (TME) with high redox level inhibits reactive oxygen species mediated treatment and immune response. The traditional "always-on" phototheranostic agents have often restricted the clinical translation due to their non-specific imaging signal and phototoxicity. Herein, a novel glutathione (GSH) depletion-mediated in situ transformation strategy is proposed, and the precursors of Berlin green nanocubes can be transformed into Prussian blue nanocubes (denoted as t-PB NCs) both in tumor cells and dendritic cells (DCs), which significantly enhance the accuracy of tumor-specific three-dimensional photoacoustic imaging and tumor regional phototherapy, reducing cytotoxic effects towards healthy cells. Moreover, with GSH depletion, t-PB NCs can also enhance phototherapy to induce powerful immunogenic cell death (ICD) and promote DC maturation. Thus, this many-birds-with-onestone GSH depletion-mediated in situ transformation strategy paves the way for tumor-specific precise photoacoustic imaging and efficient photoimmunotherapy.

GSH depletion-mediated in situ transformation strategy to enhance tumor-specific imaging and photoimmunotherapy by transforming GSH-sensitive Berlin green nanocubes (BG NCs, an analogue of Prussian blue nanocubes) into Prussian blue nanocubes31 (hereafter denoted as t-PB the NCs) both in tumor cells and DCs. Once the dormant BG NCs accumulate in the tumor site through the EPR effect and in tumor cells by endocytosis, Fe^{3+} in BG NCs transform into Fe^{2+} in t-PB NCs, thereby leading to GSH depletion and tumor-specific photoacoustic (PA) activation without signal interference from normal tissues. Moreover, the intracellular redox dyshomeostasis induced by GSH depletion enhanced ROS-mediated PDT and amplified immunogenicity of tumor cells to ultimately induce powerful ICD and promote DC maturation. When such a transformation was triggered in DCs, GSH depletion also promoted the ROS generation that stimulated the maturation of DCs and immune activation. Overall, this study has demonstrated that t-PB NCs can be activated as valuable phototheranostic agents both in tumor cells and DCs by endogenous GSH, which can be used as an

effective means to augment tumor-specific multifunctional imaging-guided precise photoimmunotherapy.

Photoluminescence spectroscopy:

For PL spectroscopy sample was prepared by adding different concentration of GSH (8µM, 40µM ,80µM ,8mM ,40mM ,80mM)with PB_{60},Mn:PB(5%),Mn:PB(15%),Mn:PB(30%),MnPB(50%) in 1:20 ratio.The concentration of prussian blue and manganese doped prussian blue solution was 0.02mg/ml.After adding GSH with prussian blue and Mn doped prussian blue ,solution was kept for 2 hours.

For different concentration of manganese in prussian blue the absorbance change rate is different. PB_{60} ,Mn:PB(5%) ,Mn:PB(15%) ,Mn:PB(30%) ,MnPB(50%) were allowed to react with 8µM ,40µM, 80µM GSH for 2 hour and then measured Photoluminescence spectroscopy, shown in the following figure. PB and Mn doped prussian blue(0.02mg/ml) shows photoluminescence effect under the excitation of wavelength 406nm and emission at 813 nm.The PL emission intensity is the result of the recombination of photogenerated electrons and holes.Lower the intensity ,lower the recombination rate.

GSH is an antioxidant and undergo redox reaction with metal ion.If GSH interact with Mn centre of doped prussian blue it could reduces or oxidize Mn ion potentially changes the oxidation state of Mn and altering the photoluminescence property.

GSH,being a thoil containing molecule can act as a passivating agent of the surface of PB_{60} ,Mn:PB(5%) ,Mn:PB(15%) ,Mn:PB(30%) ,MnPB(50%).This passivation reduces surface defects and trap states that usually lead to non radiative recombination that potentially increases photoluminescence.

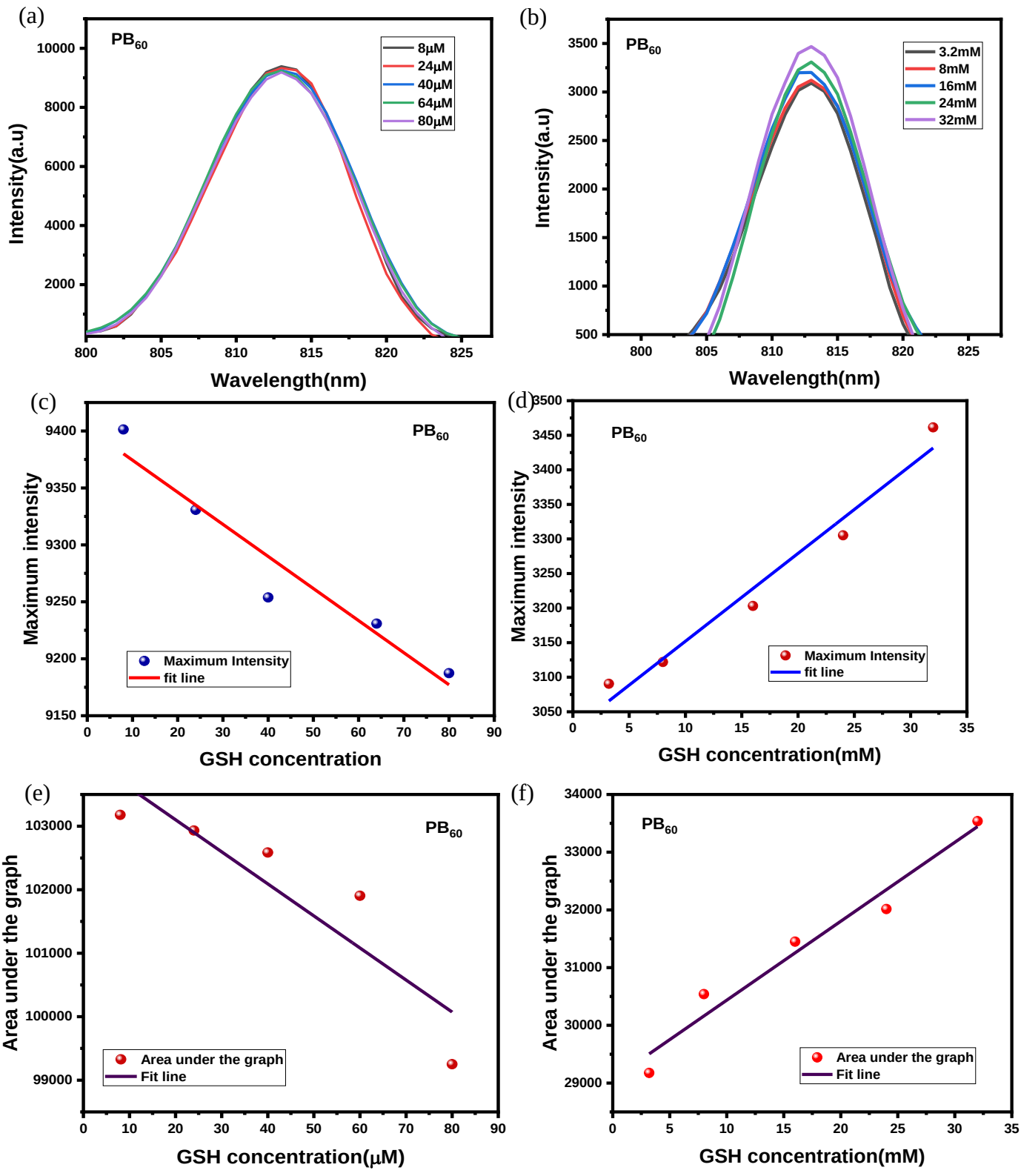


Figure:5.17-PL spectra of (a)PB_{60}-GSH(μM)(b)PB_{60}-GSH(mM),PL intensity Vs GSH conc. of(c)PB_{60}-GSH(μM)(d)PB_{60}-GSH(mM),area under the graph Vs conc.of GSH (e)PB_{60}-GSH(μM)(f) PB_{60}GSH(mM),

When PB_{60} reacts with GSH(8,24,40,64,80micromolar) the change of maximum PL intemsity is very low.As the GSH concentration increase ,PL intensity decreases.The slop of maximum PL intensity Vs

GSH concentration is-2.81736 and slope of area under the graph vs GSH concentration is -50.47645.But for higher concentration of GSH(3.2,8,16,24 and 32mM) ,it shows completely opposite.when the GSH concentration increases,PL intensity aliso increases. The slop of maximum PL intensity Vs GSH concentration is 12.70385 . slope of area under the graph vs GSH concentration is 136.75609.

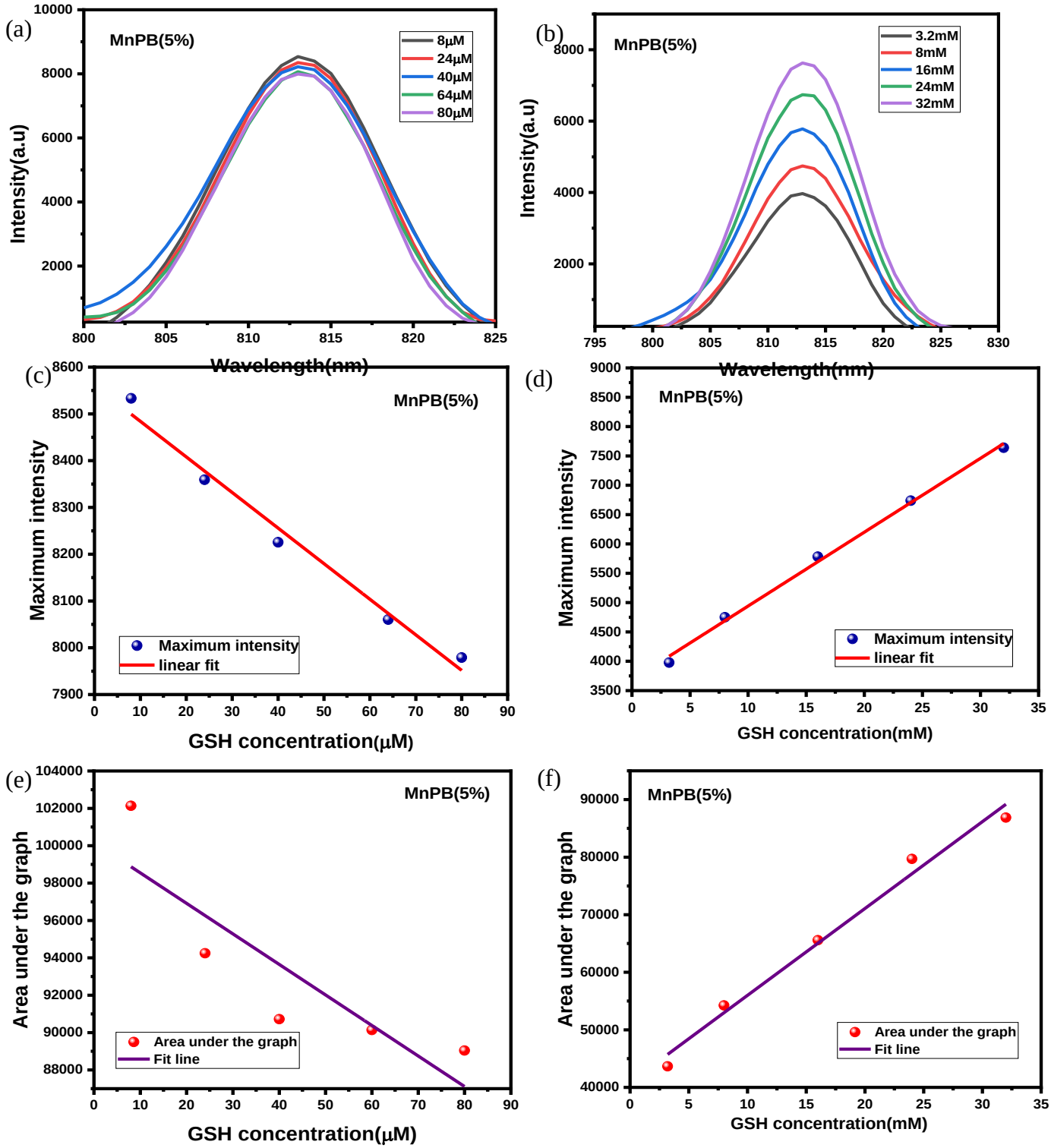
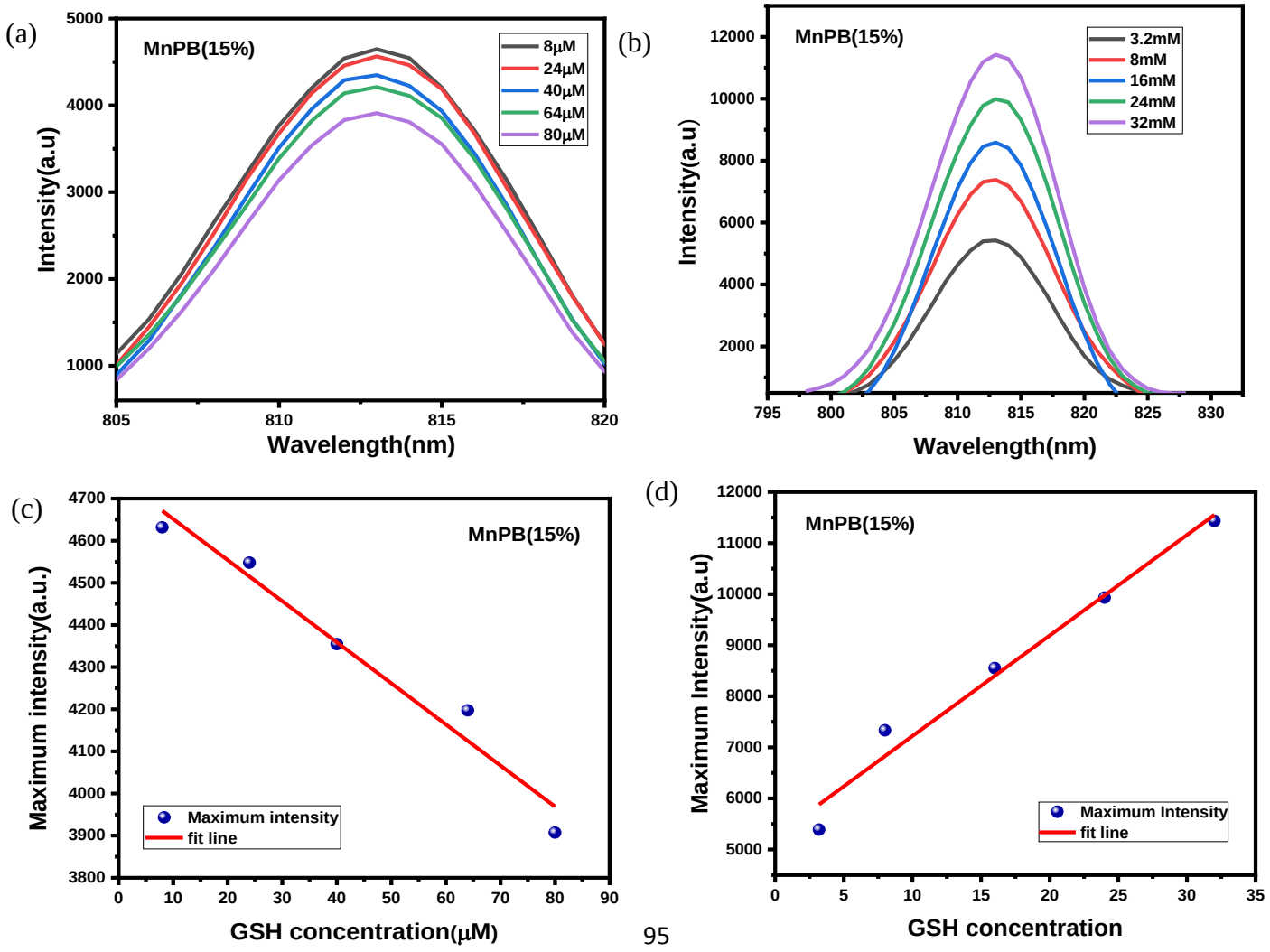


Figure:5.18-PL spectra of (a)MnPB(5%)-GSH(μM)(b) MnPB(5%)-),-GSH(mM),PL intensity Vs GSH conc. of(c)MnPB(5%)-GSH(μM)(d) MnPB(5%)--GSH(mM),area under the graph Vs conc.of GSH (e) MnPB(5%)--GSH(μM)(f) MnPB(5%)-GSH(mM),

When Mn:PB(5%) reacts with GSH(8,24,40,64,80micromolar) the change of maximum PL intemsity is very low.As the GSH concentration increase ,PL intensity decreases.The slop of maximum PL intensity Vs GSH concentration is -7.60824, and slope of area under the graph vs GSH concentration is-92.93919 .But for higher concentration of GSH(3.2,8,16,24 and 32mM) ,it shows completely opposite.when the GSH concentration increases,PL intensity also increases. The slop of maximum PL intensity Vs GSH concentration is 125.89991. slope of area under the graph vs GSH concentration is .Mn:PB(5%) is more sensitive than PB_{60}.



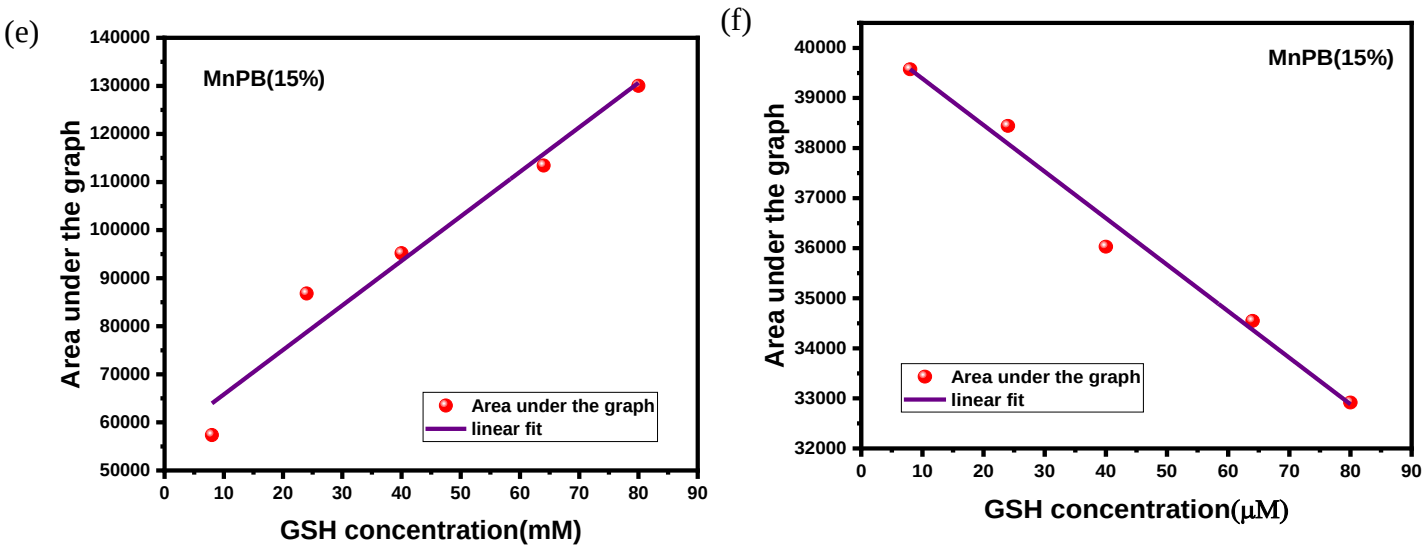
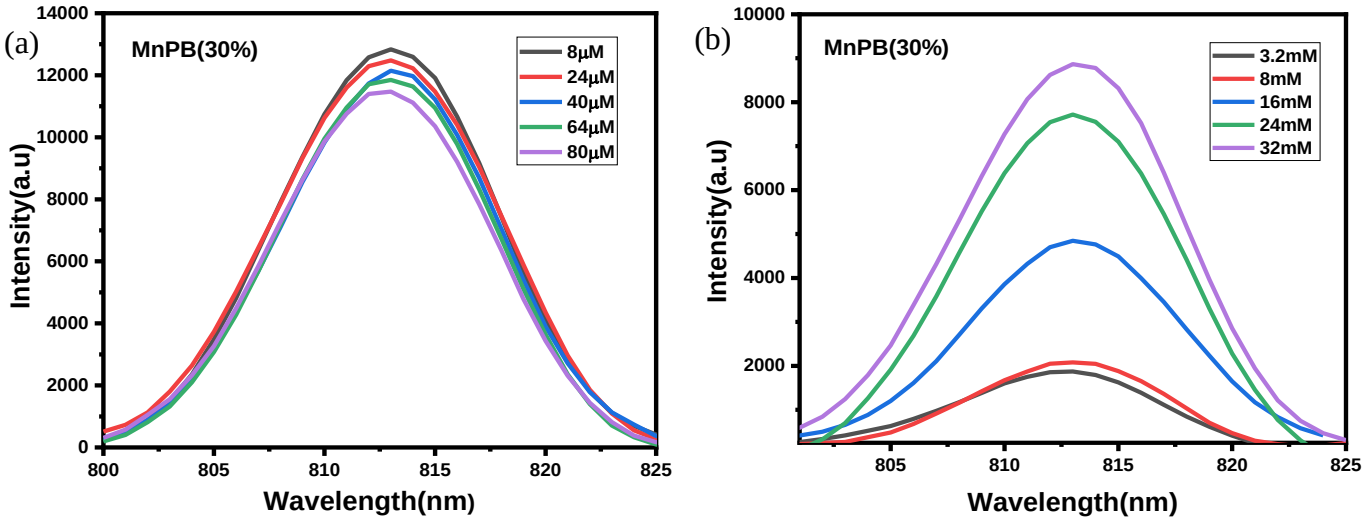


Figure:5.19-PL spectra of (a)MnPB(15%)-GSH(μM)(b) MnPB(15%)-),-GSH(mM),PL intensity Vs GSH conc. of(c)MnPB(15%)-GSH(μM)(d) MnPB(15%)--GSH(mM),area under the graph Vs conc.of GSH (e) MnPB(15%)--GSH(μM)(f) MnPB(15%)-GSH(mM),

When Mn:PB(15%) reacts with GSH(8,24,40,64,80micromolar) the change of maximum PL intemsity is very low.As the GSH concentration increase ,PL intensity decreases.The slop of maximum PL intensity Vs GSH concentration is , -9.75304 and slope of area under the graph vs GSH concentration is -163.35101 .But for higher concentration of GSH(3.2,8,16,24 and 32mM) ,it shows completely opposite.when the GSH concentration increases,PL intensity also increases. The slop of maximum PL intensity Vs GSH concentration is 196.84. slope of area under the graph vs GSH concentration is 1508.75939 .Mn:PB1(5%) is more sensitive than Mn:PB(5%).



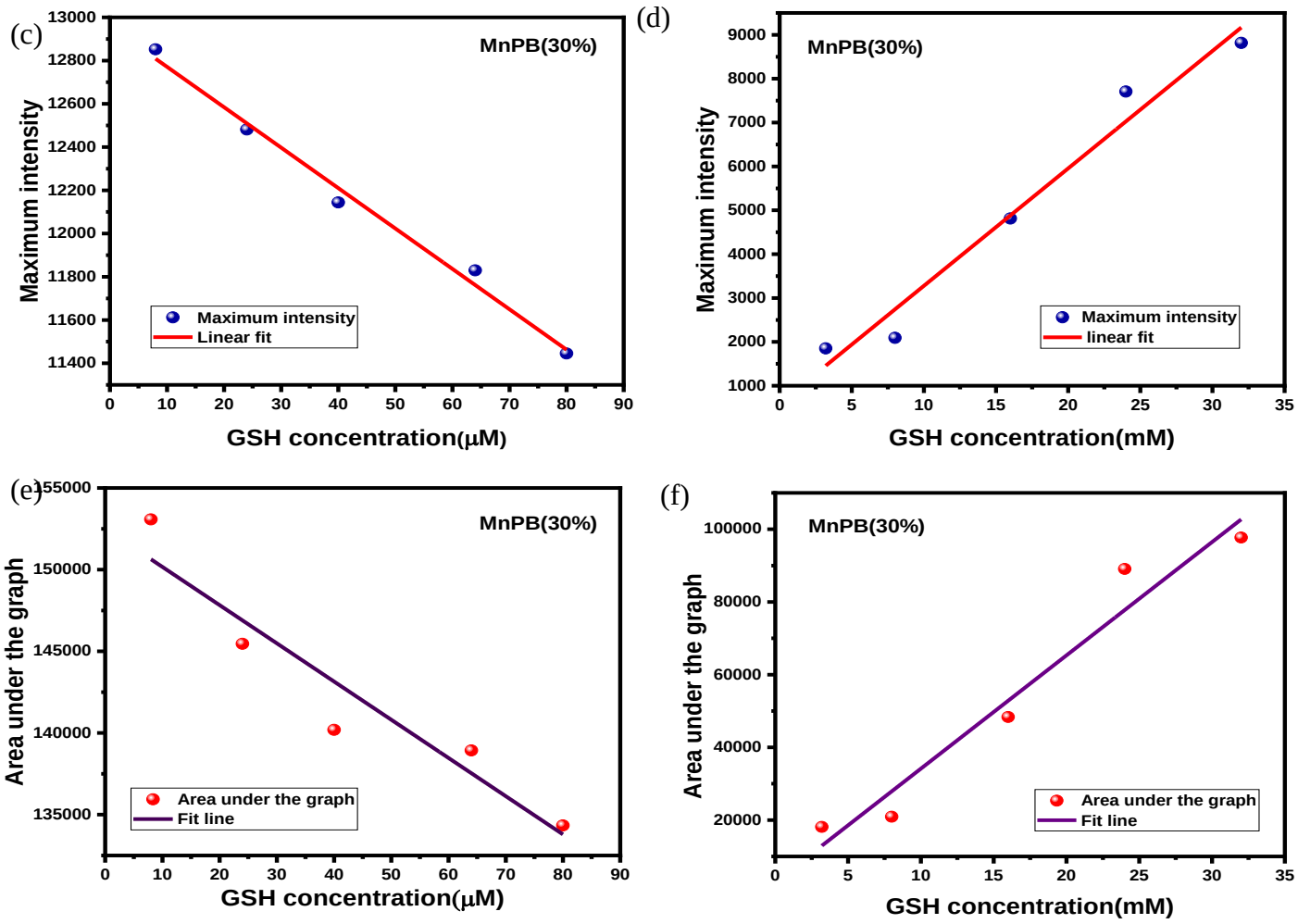


Figure:5.20-PL spectra of (a)MnPB(30%)-GSH(μM)(b) MnPB(30%)-),-GSH(mM),PL intensity Vs GSH conc. of(c)MnPB(30%)-GSH(μM)(d) MnPB(30%)--GSH(mM),area under the graph Vs conc.of GSH (e) MnPB(30%)--GSH(μM)(f) MnPB(30%)-GSH(mM),

When Mn:PB(30%) reacts with GSH(8,24,40,64,80micromolar) the change of maximum PL intemsity is very low.As the GSH concentration increase ,PL intensity decreases.The slop of maximum PL intensity Vs GSH concentration is , -18.69591 and slope of area under the graph vs GSH concentration is -233.91951 .But for higher concentration of GSH(3.2,8,16,24 and 32mM) ,it shows completely opposite.when the GSH concentration increases,PL intensity also increases. The slop of maximum PL intensity Vs GSH concentration is 267.715. slope of area under the graph vs GSH concentration is 3116.49983 .Mn:PB1(5%) is more sensitive than Mn:PB(15%).

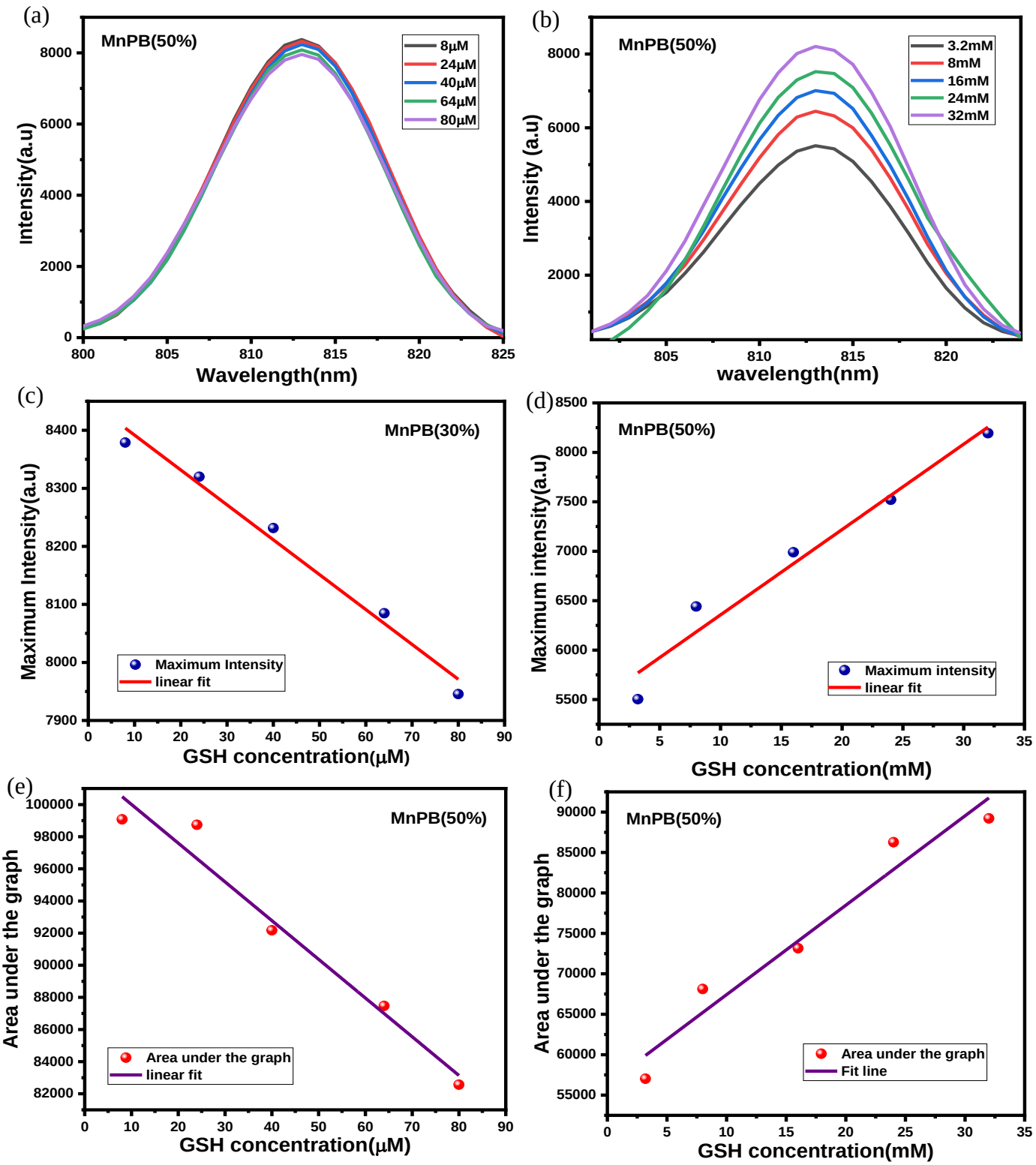


Figure:5.21-PL spectra of (a)MnPB(50%)-GSH(μM)(b) MnPB(50%)-),-GSH(mM),PL intensity Vs GSH conc. of(c)MnPB(50%)-GSH(μM)(d) MnPB(50%)--GSH(mM),area under the graph Vs conc.of GSH (e) MnPB(50%)--GSH(μM)(f) MnPB(50%)-GSH(mM),

When Mn:PB(50%) reacts with GSH(8,24,40,64,80micromolar) the change of maximum PL intemsity is very low.As the GSH concentration increase ,PL intensity decreases.The slop of maximum PL intensity Vs GSH concentration is , -6.01079 and slope of area under the graph vs GSH concentration is -220.99553 .But for higher concentration of GSH(3.2,8,16,24 and 32mM) ,it shows completely opposite.when the GSH concentration increases,PL intensity also increases. The slop of maximum PL intensity Vs GSH concentration is . 86.31048 slope of area under the graph vs GSH concentration is 1105.62925 .Mn:PB(50%) is less sensitive than Mn:PB(30%).

So the sensitivity of Mn:PB is more then prussian blue.It is maximum for Mn:PB(30%) .

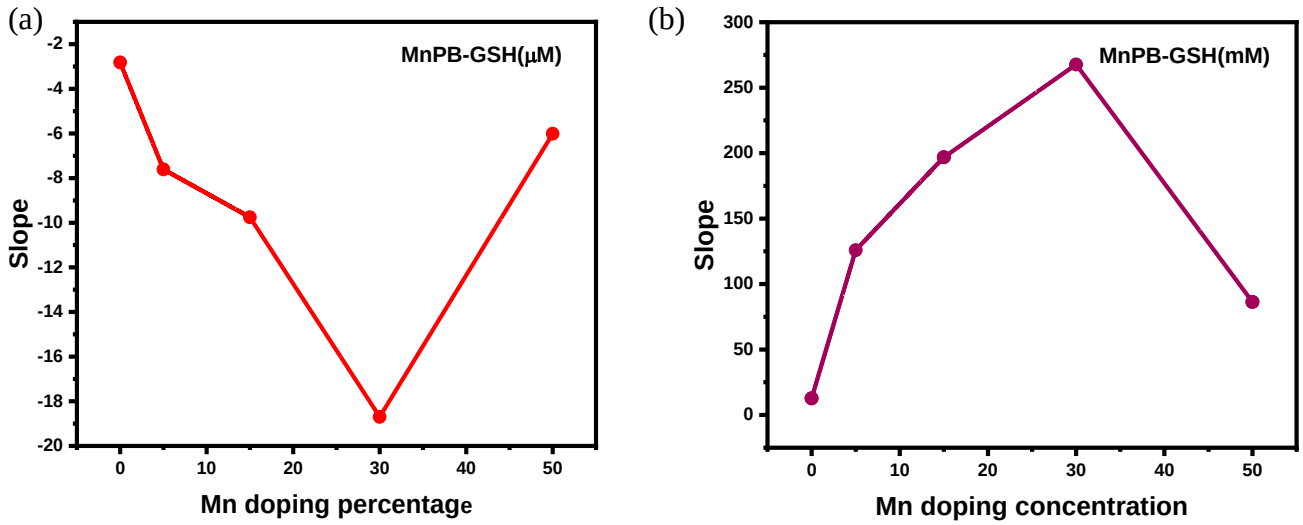


Fig.5.21-slope of PL intensity with respect to GSH concentration vs Mn doping percentage of(a)MnPB-GSH(μM)(b) MnPB-GSH(mM)

The slop of maximum PL intensity for 8,24,40,64,80 μM GSH concentration is -2.81736, -7.60824, -9.75304 , -18.69591 , and -6.01079 for PB60 ,Mn:PB(5%) ,Mn:pB(15%) ,Mn:PB(30%) ,Mn:PB(50%) respectively.So the slope is maximum for 30% manganese doped prussian blue .

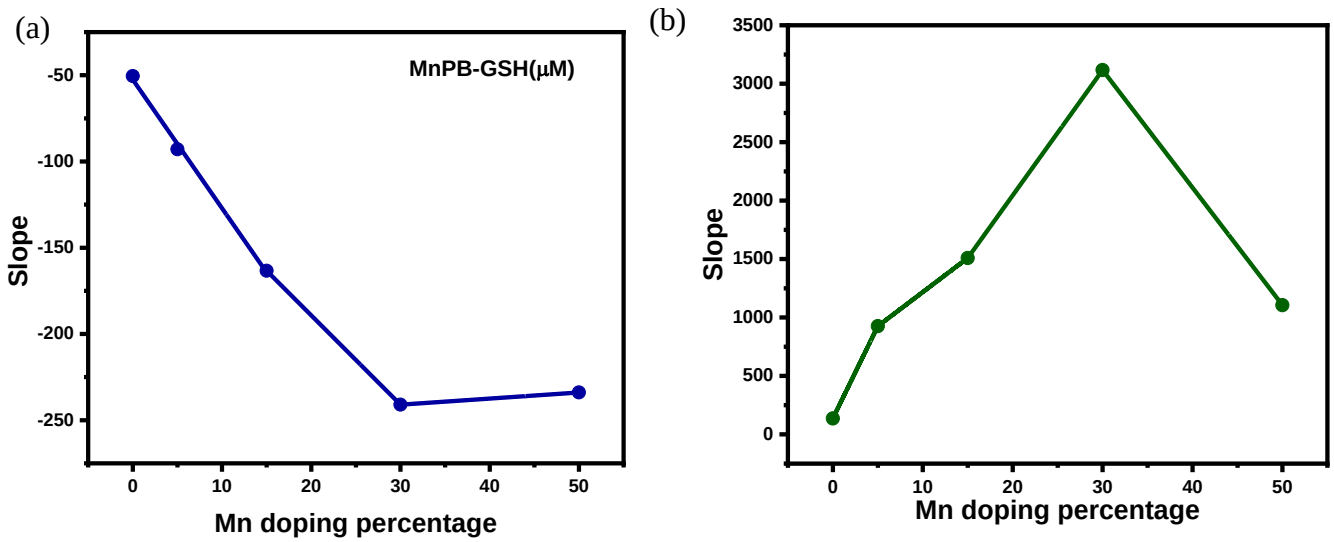


Fig.5.22-slope of area under the graph with respect to GSH concentration vs Mn doping percentage of(a)MnPB-GSH(μM)(b) MnPB-GSH(mM)

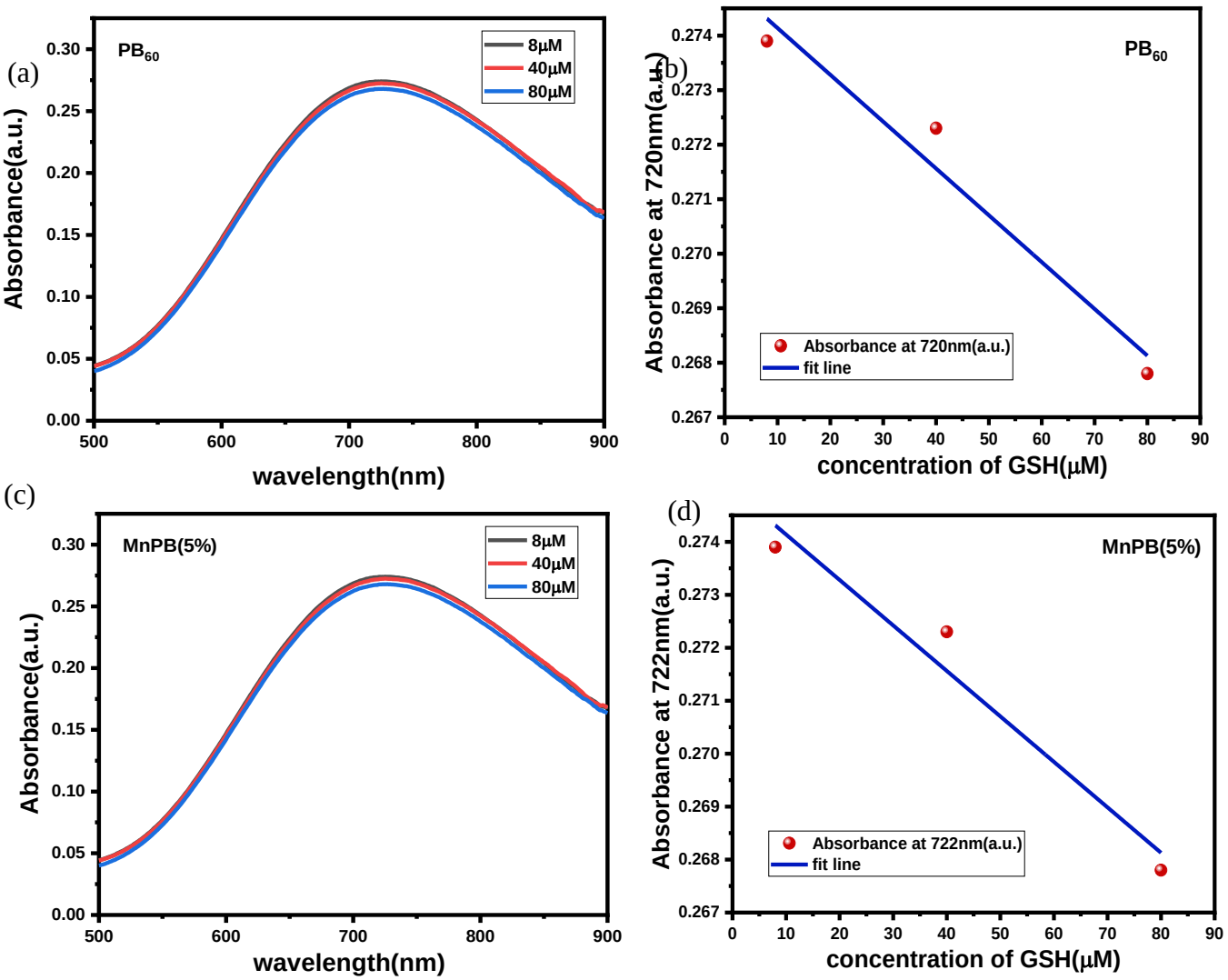
The slope of the Area under the graph with respect to the different concentration of GSH (8,24,40,64,80μM) are -50.47645, -7.60824, , -9.75304 , -18.69591 , -6.01079 for PB_{60},Mn:PB(5%),MnPB(15%),Mn:PB(15%),and Mn:PB(30%),Mn:PB(50%) respectively.

he slope of the Area under the graph with respect to the different concentration of GSH(3.2,8,16,24,32mM) are136.75609, is 135.89991, 926.16292, 1508, 3116.5 and 1105.63 for PB_{60},Mn:PB(5%),MnPB(15%),Mn:PB(15%),and Mn:PB(30%),Mn:PB(50%) respectively.

UV Vis Sprctroscopy:

For UV Vis spectroscopy sample was prepared by adding different concentration of GSH (8µM, 40µM ,80µM ,8mM ,40mM ,80mM)with PB_{60},Mn:PB(5%),Mn:PB(15%),Mn:PB(30%),MnPB(50%) in 1:20 ratio.The concentration of prussian blue and manganese doped prussian blue solution was 0.02mg/ml.After adding GSH with prussian blue and Mn doped prussian blue ,solution was kept for 2 hours.

For different concentration of manganese in prussian blue the absorbance change rate is different. PB_{60} ,Mn:PB(5%) ,Mn:PB(15%) ,Mn:PB(30%) ,MnPB(50%) were allowed to react with 8µM ,40µM, 80µM GSH and then measured UV Vis spectroscopy, following figure shows .



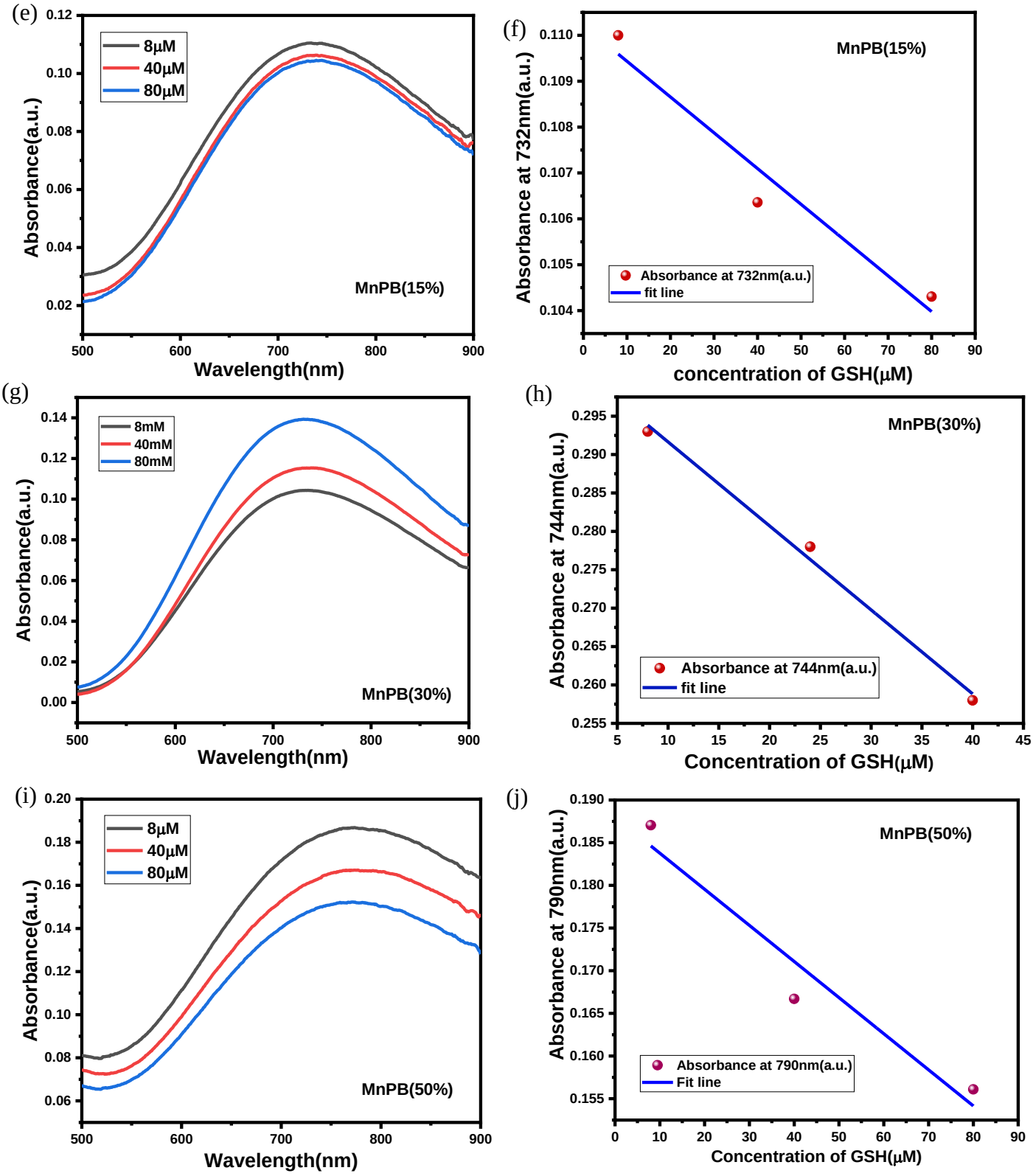
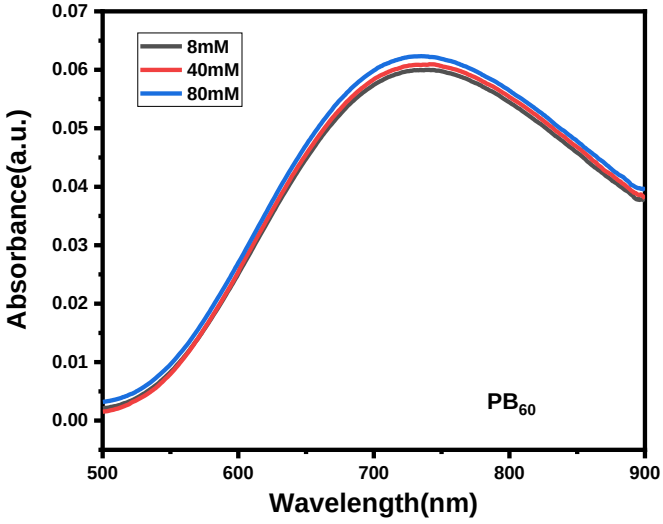


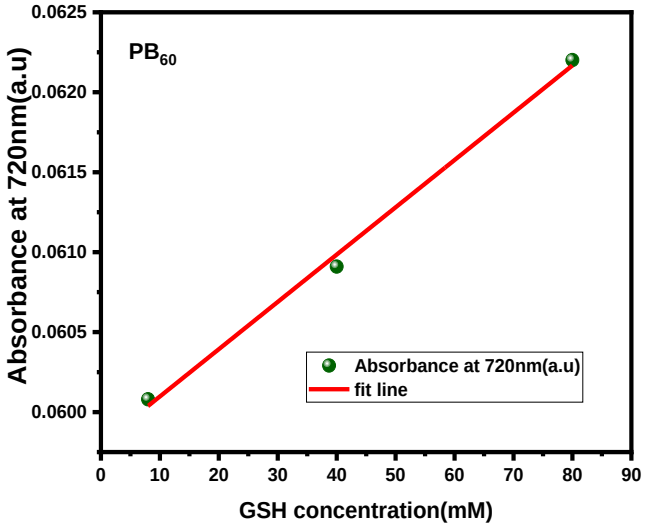
Fig5.23-UV Vis absorbtion Vs wavelength of (a)PB_{60} (c)MnPB(5%) ,(e)MnPB(15%) ,(g)MnPB(30%) , (i)MnPB(50%) –GSH(μM)Peak absorbance Vs concentration of GSH(μM) of of (b)PB_{60} (d)MnPB(5%) ,(f)MnPB(15%) ,(h)MnPB(30%) , (j)MnPB(50%) –GSH(μM)

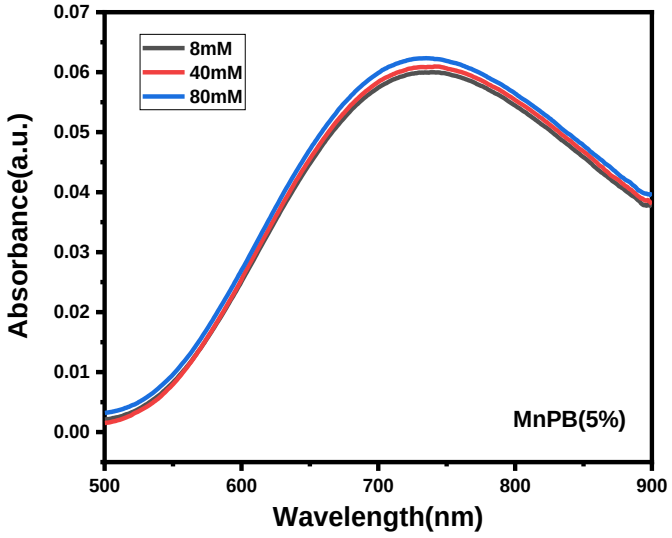
Whenever the concentration pf GSH increases ,the intensity of UV Vis absorbtion decreases .For different doping concentration of Mn the rate of change of absorbtion is different .Fig (5.23)shows that for 30% doping concentration of manganese the change of intensity is faster.

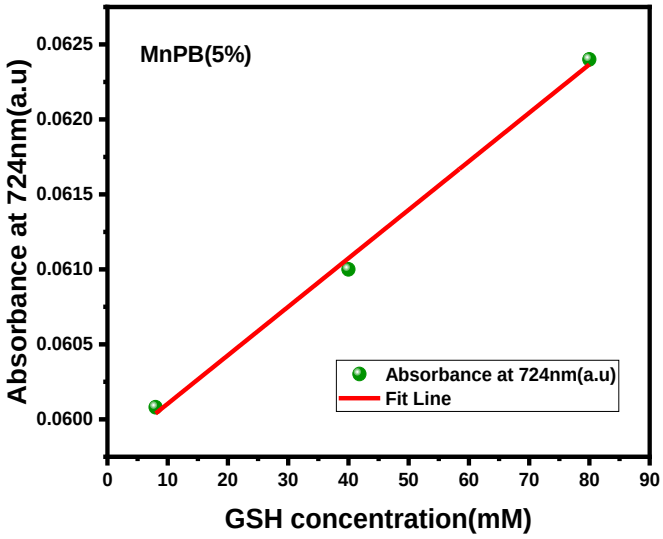
Sample	**Slop of peak intensity (a.u.) vs GSH concentration(μM)**
PB60	-7.89E-05
MnPB(5%)	-8.09E-05
MnPB(15%)	-8.59E-05
MnPB(30%)	-0.00109
MnPB(50%)	-4.23E-04

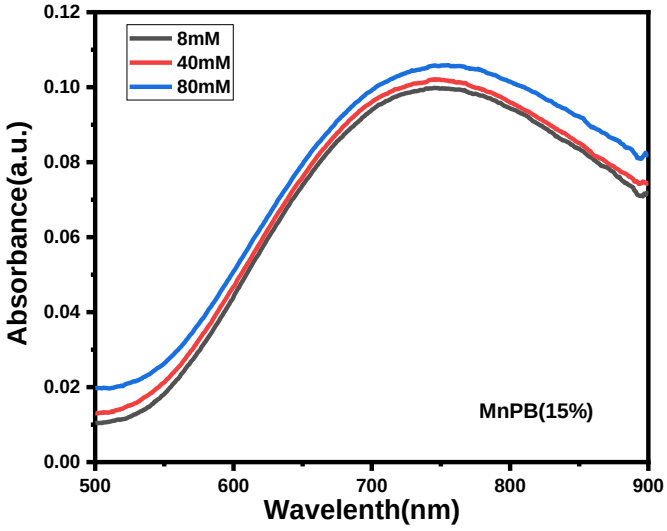
From the above data it is very clear that Mn:15(30%) has high sensitivity to detect glutathoin.

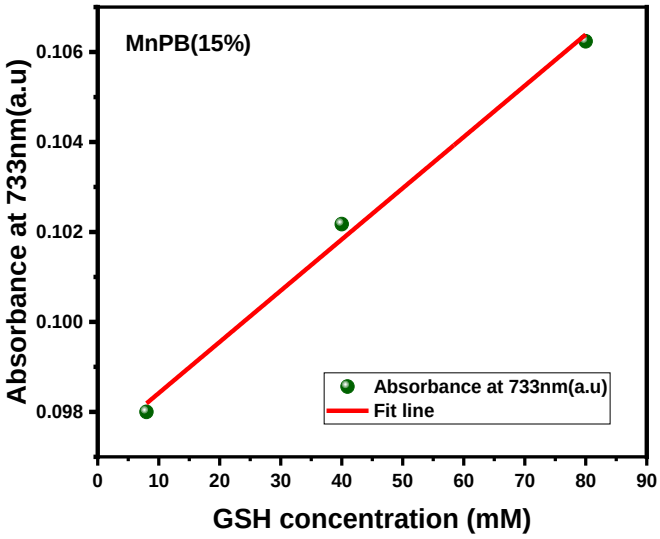

8mM
40mM
80mM
PB60
Absorbance(a.u.)
Wavelength(nm)


PB60
Absorbance at 720nm(a.u)
fit line
Absorbance at 720nm(a.u)
GSH concentration(mM)


8mM
40mM
80mM
MnPB(5%)
Absorbance(a.u.)
Wavelength(nm)


MnPB(5%)
Absorbance at 724nm(a.u)
Fit Line
Absorbance at 724nm(a.u)
GSH concentration(mM)


8mM
40mM
80mM
MnPB(15%)
Absorbance(a.u.)
Wavelength(nm)


MnPB(15%)
Absorbance at 733nm(a.u)
Fit line
Absorbance at 733nm(a.u)
GSH concentration (mM)

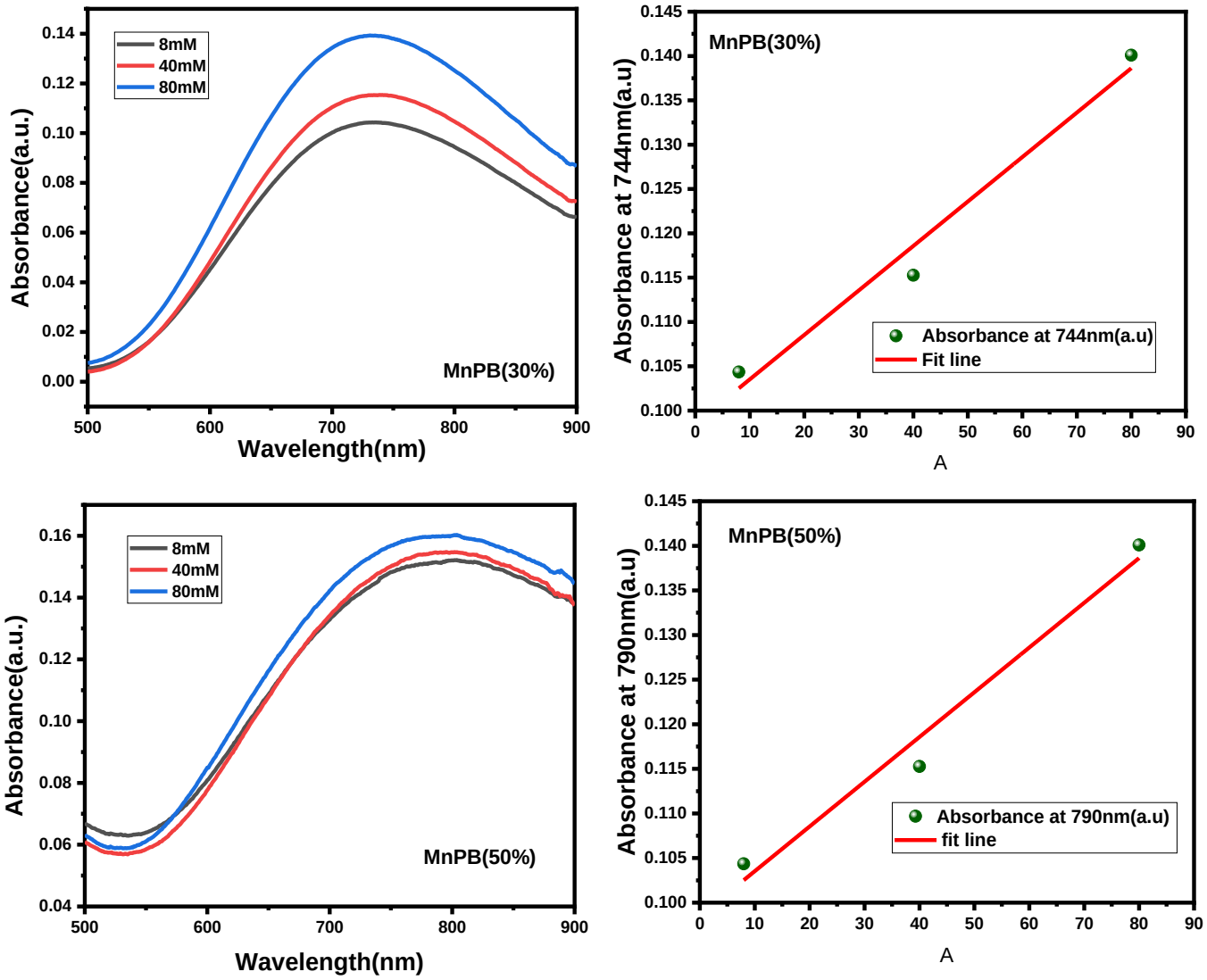


Fig5.24-UV Vis absorbtion Vs wavelength of (a)PB_{60} (c)MnPB(5%) ,(e)MnPB(15%) ,(g)MnPB(30%) , (i)MnPB(50%) –GSH(µM)Peak absorbance Vs concentration of GSH(mM) of of (b)PB_{60} (d)MnPB(5%) ,(f)MnPB(15%) ,(h)MnPB(30%) , (j)MnPB(50%) –GSH(mM)

For high concentration of GSH(millimolar) ,Whenever the concentration pf GSH increases ,the intensity of UV Vis absorbtion increases .For different doping concentration of Mn the rate of change of absorbtion is different .Fig (5.24) shows that for 30% doping concentration of manganese the change of intensity is faster.

Sample	Slop of peak intensity (a.u.) vsGSH concentration(millimolar)
PB_{60}	1.16E-05
MnPB(5%)	2.96E-05
MnPB(15%)	1.14E-04
MnPB(30%)	5.01E-04
MnPB(50%)	3.01E-04

So,Mn:PB(30%) is most sensitive as it has higest slope among all sample.

References

1 .X. Zhang, S. Lin, S. Liu, X. Tan, Y. Dai and F. Xia, Coord. Chem. Rev., 2020, 429, 213652.

2. T. Wu, W. Hou, Z. Ma, M. Liu, X. Liu, Y. Zhang and S. Yao, Microchim. Acta, 2019, 186, 1–7.

3 .W. Yin, J. Yu, F. Lv, L. Yan, L. R. Zheng, Z. Gu and Y. Zhao, ACS Nano, 2016, 10, 11000–11011.

4 L. Gao, J. Zhuang, L. Nie, J. Zhang, Y. Zhang, N. Gu, T. Wang, J. Feng, D. Yang, S. Perrett and X. Yan, Nat. Nanotechnol., 2007, 2, 577–583.

5 .X. Wang, J. Xu, D. Yang, C. Sun, Q. Sun, F. He, S. Gai, C. Zhong, C. Li and P. Yang, Chem. Eng. J., 2018, 354, 1141–1152.

6 .J.-t Jang, J. Lee, J. Seon, E. Ju, M. Kim, Y. I. Kim, M. G. Kim, Y. Takemura, A. S. Arbab, K. W. Kang, K. H. Park, S. H. Paek and S. Bae, Adv. Mater., 2018, 30, 1704362.

7 .S. Xiao, Y. Lu, M. Feng, M. Dong, Z. Cao, X. Zhang, Y. Chen and J. Liu, Chem. Eng. J., 2020, 396, 125294. 8 S. Wang, H. Yan, Y. Wang, N. Wang, Y. Lin and M. Li, Microchim. Acta, 2019, 186, 1–8.

9. P. Ni, Y. Sun, H. Dai, W. Lu, S. Jiang, Y. Wang, Z. Li and Z. Li, Sens. Actuators, B, 2016, 231, 860–866.

10. S. Singh and P. C. Pandey, J. Environ. Chem. Eng., 2020, 8, 103753.

11. M. D. Jerez-Masaquiza, L. Ferna ´ndez, G. Gonza ´lez, M. Montero-Jime ´nez and P. J. Espinoza-Montero, Nanomaterials, 2020, 10, 1328. 12 Y. Zhai, H. Zhang, L. Zhang and S. Dong, Nanoscale, 2016, 8, 9493–9497.

Conclusion:

In this study,Mn@PB nanoparticle with oxidase-like activity were synthesized using a simple and straightforward method to mitigate the interference caused by the color of PB itself Building upon the significant activity of these nanoparticles, a biosensing platform for visually detecting GSH through colorimetry was developed. The platform demonstrated excellent sensitivity with low detection limits and was successfully applied for GSH detection in human physiological body fluids, namely, saliva and urine. Additionally, a portable colorimetric method was devised by integrating the platform with modern intelligent technology, utilizing a smartphone as the detector. The combination of the highly sensitive color development of Mn @PB and GSH detection method holds promise for further extension into clinical detection. This approach can provide valuable methods and technical support for routine health monitoring and the detection of disease markers, particularly in medically underserved regions. It is anticipated that this method will expand the application of PB-based nanozymes in biosensing and pave the way for the development of novel